DESIGN CONSIDERATIONS AND ESTIMATED ON-VEHICLE PERFORMANCE FOR A COMPRESSION-COUPLE BASED THERMOELECTRIC GENERATOR

By

Nariman Mansouri Boroujeni

A DISSERTATION

Submitted to
Michigan State University
in partial fulfillment of the requirements
for the degree of

Mechanical Engineering - Doctor of Philosophy

2015

ABSTRACT

DESIGN CONSIDERATION AND ESTIMATED ON-VEHICLE PERFORMANCE FOR A COMPRESSION-COUPLE BASED THERMOELECTRIC GENERATOR

By

Nariman Mansouri Boroujeni

Approximately 55% percent of the energy produced from conventional vehicle resources is lost in the form of heat. An efficient waste heat recovery process will undoubtedly lead to improved fuel efficiency, reduced greenhouse gas emissions and increased profit. Thermoelectric generators (TEGs) are one of the most viable waste heat recovery approaches that are being widely studied among energy-intensive industries which focus on the ways to convert waste heat energy to electrical energy. With the rising cost of fuel and increasing demand for clean energy, solid-state thermoelectric (TE) devices are good candidates to reduce fuel consumption and CO_2 emissions in an automobile. Although they are reliable energy converters, there are several barriers that have limited their implementation into wide market acceptance for automotive applications. These barriers include: the unsuitability of conventional thermoelectric materials for the automotive waste heat recovery temperature range; the rarity and toxicity of some otherwise suitable materials; and the limited ability to mass-manufacture thermoelectric devices from certain materials. However, skutterudite is one class of material that has demonstrated significant promise in the transportation waste heat recovery temperature domain. These materials have little toxicity, relatively abundant, and have been studied and developed by NASA-JPL and others for the past 20 years.

The converted electrical energy can be used to recharge batteries, run auxiliary electrical accessories, support heating system, and etc. However, durability and reliability of the

thermoelectric generators are the most significant concerns in the product development process. Cracking of the skutterudite materials at hot-side interface is found to be a major failure mechanism of thermoelectric generators under thermal cyclic loading. Cracking affects not only the structural integrity but also the energy conversion and overall performance of the system.

In this project, cracking of thermoelectric material as observed in performance testing is analyzed using numerical simulations and analytic experiments. With the help of finite element analysis, the detailed distribution of stress, strain, and temperature are obtained for each design. Finite element based simulations show the tensile stresses as the main reason causing radial and circumferential cracks in the skutterudite. For thermoelectric generator design, loading conditions, closed-form analytical solutions of stress/strain distributions are derived and scenarios with minimum tensile stresses are sought. All these approaches yield a minimum stress/strain necessary to produce any cracks. Finally, based on FE and computational fluid dynamic (CFD) analysis, strategies in tensile stress reduction and failure prevention are proposed followed by the reasons to change the thermoelectric couple design for having a reliable thermoelectric generator.

Using a modified compression couple technology, a 15-watt thermoelectric generator prototype was designed, built and tested. Experimental results of the TEG are presented. This prototype was analyzed using 1-D engine simulation and computational fluid dynamics (CFD), and the resulting analysis is presented. In a model configuration utilizing eight of these 15-watt TEGs, each having a 4% conversion efficiency, an estimated 136 watts of electricity could be produced at an operating point of 2000 RPM and 3 bar engine load in a 4.7L V6 gasoline engine.

This dissertation is dedicated to:

My family: Abdollah Mansouri, Tooran Foroughi, Dr. Niloofar Mansouri, and Dr. Nima Mansouri

for their endless love, support and encouragement

ACKNOWLEDGEMENTS

First of all, I would like to express my appreciation to my advisor, Prof. Harold Schock, for the opportunity to work with him at the Energy and Automotive Lab at Michigan State University. I would also like to thank him since he has provided motivation, aspiring guidance, encouragement, and for his continual support throughout my PhD program. Without his mentoring, I would not able to complete this work.

In addition, I would like to thank Tenneco Inc. located in Grass Lake, MI for their support. Dipankar Sahoo and Adam Kotrba were especially critical to the success of this dissertation.

Furthermore, I would like extend my appreciation to Edward Timm who helped me a lot to learn different manufacturing techniques and materials preparation. I am also sincerely grateful to him for sharing his truthful, wise and illuminating views on the project. I would like to thank Tom Stuecken, Brian K. Rowley, Trevor Ruckle, Jeff Higel, Jen Higel, Gary Keeney, Kevin Moran, Ravi Vedula, Dr. Giles Brereton, Dr. Katy Colbry Luchini, and Tim Luchini for their guidance in my research. I would also like to acknowledge the significant contributions made by my committee members Prof. Alfred Loos, Prof. George Zhu, and Prof. Donald Morelli during my doctorate research journey. Additionally, I am grateful for my fellow friends and colleagues at MSU for their support and cooperation during my studies.

My family has been an inspiration to me throughout my academic study and I would like to thank them for their ongoing emotional and financial support.

TABLE OF CONTENTS

LIST OF TABLES

LIST OF FIGURES

LIST OF SYMBOLS AND ABBREVIATIONS

IC	Internal Combustion
TE	Thermoelectric
TEG	Thermoelectric Generator
ZT	Figure-of-merit
S	Seebeck coefficient
σ_e	Electrical conductivity
k	Thermal conductivity
T_H	Temperature of the hot surface
T_C	Temperature of the cold surface
η	Energy conversion efficiency
E	Young’s modulus
α	Thermal expansion coefficient
ΔT	Temperature gradient
ν	Poisson’s ratio
FEA	Finite Element Analysis
CFD	Computational Fluid Dynamics
EGR	Exhaust Gas Recirculation
Q	Magnitude of the heat
π	Peltier coefficient
T_{abs}	Absolute temperature
I	Current
q	Heat production per unit volume

κ	Thomson coefficient
J	Local current density
R	Resistance
γ	Thermal resistivity
TECT	Thermal Energy Conversion Technologies
DC	Direct Current
AC	Alternate Current
SKD	Skutterudite
JPL	Jet Propulsion Laboratory
SEM	Scanning Electron Microscope
CMSC	The Composite Materials and Structures Center

1. INTRODUCTION

The purpose of using internal combustion engines (IC) is to extract mechanical power from the chemical energy stored in the fuel. This chemical energy in the fuel is converted to mechanical by burning the fuel inside the cylinder chamber and extracting the work through piston restrained expansion of the expanding gas.

The best current internal combustion engines manufactured by auto industries have brake efficiency up to 45%, which means almost half of the energy coming from combustion converts into the mechanical power needed to brake the vehicle. However, at least 35% of the fuel energy goes to exhaust, turning to waste heat. The rest of the energy is lost due to heat transfer in the cooling system and etc. Simple calculation shows 55% of the energy coming from combustion is heat loss [1]. It means modern IC engines convert only forty five percent of the energy coming from combustion into the mechanical energy needed to run the vehicle at the engine most efficient operating condition. When the vehicle is stopped and idling with accessories off, the efficiency of the engine is zero. This is the conundrum facing the automobile engines. It is clear, however, that one place where an energy source exists is in the heat rejected from the engine [2].

A serious rise in fuel and transportation costs has forced engineers to bring new ideas to develop new technologies needed to improve the fuel efficiency and reduce greenhouse gases emission. Developing fuel efficient automobile engines, which cause less environmental impacts including reduced air pollutants and less CO_2, is a major challenge [3]. As the energy efficiency improves, the process becomes less expensive which leads an incentive usage of the energy [4]. Technologies such as direct fuel injection, variable valve timing, variable cam timing, brake energy regeneration, exhaust-driven turbochargers, and auto start/stop function have played an important role in reducing the fuel consumption over the past decade.

Engineers have started to examine the different ways to use the waste heat out of the engines. There has been an increasing attention to the application of low-grade heat sources, such as waste heat from industrial plants, exhaust gases, and geothermal resources [5]. These sources of energy can reduce fossil-fuel produced electricity demand, but the low to moderate temperature gradient cannot be easily and efficiently converted electrical power. The conversion problem causes a large amount of moderate heat simply wasted [6]. The use of waste heat as an energy source at temperatures below 140 ˚C significantly increases the cost of the production of a device capable of generating electricity [7]. However, exhaust gases from engines and turbines have a reasonable high temperature in the range of 500 ˚C, which is high enough to be considered as a thermoelectric conversion device.

In this study, an effort describes the technology barriers to provide successful performance of thermoelectric technology to convert waste heat to electricity. Thermoelectric devices are reliable, silent, small and light-weight, environmentally green, position-independent, as well as they have no vibration while performance. These are some of the advantages of thermoelectric devices, which make them preferred, over competing technologies [8]. However, the most significant disadvantage of thermoelectrics is their low efficiency [9].

The best known thermoelectric material for near room temperature applications is based on Bi_2Te_3, as first reported in 1954 [10]. As a matter of fact, making improvements beyond these materials is a challenging task. New fabrication capabilities and theoretical predictions have helped renewing interest in this area of research which has led to a number of novel materials that show very promising thermoelectric properties [11]. Some of these new materials, along with the traditional materials, are represented in **Figure 1.1**. ZT is a dimensionless figure of merit which describes the performance of a thermoelectric material. For practical purposes, a ZT of a couple or segmented couple must be greater than 1.0 for the temperature range under consideration [12].

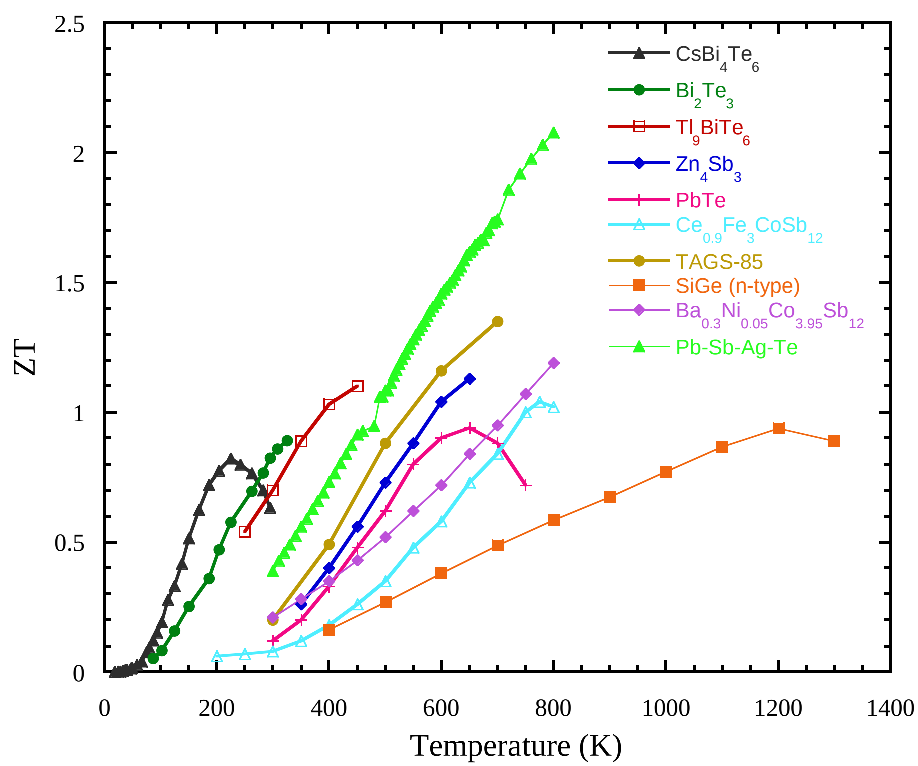

Figure 1.1. ZT vs temperature of different materials[13]

One of the best semiconductors which possesses a figure-of-merit close to one are bismuth telluride (Bi_2Te_3) based alloys [14]. The figure-of-merit is defined as:

$$ZT = \frac{S^2\sigma_e}{k}\frac{T_H + T_C}{2} \tag{1}$$

where S stands of Seebeck coefficient, σ_e is the electrical conductivity, k is the thermal conductivity of the material, and $\frac{T_H+T_C}{2}$ is the average temperature of the hot and cold surfaces. The significant effect of the figure-of-merit is underlined by the expression of the energy conversion efficiency, η, which is described below [15]

$$\eta = \left(\frac{T_H - T_C}{T_H}\right)\left(\frac{\sqrt{1+ZT} - 1}{\sqrt{1+ZT} + \frac{T_C}{T_H}}\right) \tag{2}$$

A larger figure-of-merit signifies a more promising concept for a thermoelectric material in a thermoelectric device, but there are several issues and restrictions on increasing the figure-of-merit [16]. First of all, the common value of the figure-of-merit, for most of the thermoelectric materials, is around 1.0. If ZT goes above 2.0, it affects the efficiency of the thermoelectric devices. The second and equally important issue is finding a way to maximize the heat transfer rate across the hot and cold surfaces to get higher electric power output. For the case in which the TE device is embedded inside a heat exchanger, temperature of the hot and cold surfaces are maintained by a fluid; where, the temperature gradient is controlled and cannot exceed than the temperature range of the cold and hot fluid. A third issue is minimizing damages caused by cracks due to thermo-mechanical stresses. Large temperature gradient produces bigger heat transfer rate; however it causes remarkable thermal expansion or contraction of a device. A large thermal expansion or shrinkage can be named as the main factor of the developed thermo-mechanical stresses.

The thermal conductivity coefficient in the denominator of **equation 1**, inspires the fact that reducing the thermal conductivity coefficient helps getting better figure-of-merit. A lower thermal conductivity coefficient leads to a challenge in designing of thermoelectric devices, because a higher thermal gradient across a thermoelectric material produces a thermo-mechanical stress as shown in **equation 3**.

$$\sigma = \frac{E\alpha\Delta T}{(1-\nu)k} \tag{3}$$

where E is the Young's modulus, α is the coefficient of thermal expansion, ΔT is the temperature gradient, and ν is the Poisson's ratio. Since all the mechanical and thermal properties of the thermoelectric materials depend on the temperature, **equation 3** must be a function of temperature as well [17].

$$\sigma = \frac{E(T)\alpha(T)\Delta T}{\big(1-\nu(T)\big)k(T)} \tag{4}$$

In both cars and trucks, the potential for good thermoelectric generator energy recovery occurs during high-load operation. Engine insulation and heat exchangers for heating up the oil are two common ways of using exhaust gas. Thermoelectric generators having an efficiency of 3-8% can save up to 5% of fuel under everyday driving conditions [18, 19].

The objective of this study is to develop and demonstrate stable TEG designs using experiments, finite element analysis (FEA) and computational fluid dynamics (CFD) to study the three-dimensional temperature, stress distribution, heat transfer, and fluid flow in thermoelectric couples and generators.

1.1 Thermoelectric Overview

Every day a great amount of heat is released from high temperature systems to the environment. Having the idea of recovering the waste heat into electricity was the basis of making heat-conversion devices to solve this issue. Thermoelectric materials, which are solid-state semiconductors, play a significant role in developing sustainable energy technologies by converting heat energy to electricity. Thermoelectric materials are located in a place where thermal gradient exists in the order of few hundred degrees Celsius over a distance of a few centimeters since the electrical power generation depends on temperature difference across the thermoelectric material. On the other hand, if an electrical current is applied to the thermoelectric material, temperature gradient like refrigeration will be produced. The application of thermoelectric materials includes broad aspects of engineering technologies such as air conditioners, night vision systems, energy recovery from automobile and industrial exhaust waste heat, and running satellite systems in space [20, 21]. The role of thermoelectric materials implemented into a direct energy conversion device is the extraction of electrical energy from the exhaust gases. Furthermore, installing a thermoelectric device in an exhaust system has to cope with three issues. The first is the heat transfer consideration needed for a reliable design of heat exchangers in order to get the maximum power out of the thermoelectric generator [22]. The second and equally important issue is material selection for the generator. TEG cost effective materials must be reliable and produce efficient performance in a considerable temperature gradient. The third concern of the selection of the materials is their availability in the market for thermoelectric generator applications [23].

This dissertation mostly deals with the application of thermoelectric devices in automobiles, which are motivations, to describe more about their role in converting the exhaust heat to power. Achieving high performance and reduced fuel consumption engines can occur simultaneously by installing a thermoelectric generator inside the exhaust system of vehicles.

High electrical power out of the thermoelectric generators happens during dynamic and high speed driving cycles. Engine insulation and heat exchangers for heating up the oil are two common ways of using the exhaust gas heat. Nevertheless, these are not efficient ways to use a big portion of the waste heat. New thermoelectric generators installed in the exhaust system can be a useful approach to obtain maximum energy from the available heat source. It was claimed before that the thermoelectric generators, having the efficiency around 5-8%, could save up to 5% of fuel under everyday driving conditions in a couple of years [18, 19]. In addition, thermoelectric devices over competing technologies have some advantages which make them more popular and practical such as:

- High reliability (>250,000 hours)
- Silent and no vibration
- Small electromagnetic signature
- Temperature control to fractions of a degree
- No position dependent
- Survive in severe environment
- Small and lightweight
- No chlorofluorocarbons, chemical, or compressed gases to replenish

- Environmentally green
- Reversible heat pumping direction

However, TEGs have several disadvantages. From the economic point of view, manufacturing process should be set up in a cost effective way. If production cost is not reasonable, rise in the cost of production will be followed by losing the business. From the engineering point of view, installing the thermoelectric generator after the exhaust gas recirculation (EGR) cooler might cause back pressure in the exhaust system. Back pressure refers to pressure opposed to the desired flow of waste gas having a negative effect on engine performance resulting in a drop of power output. Drop in power output must be compensated by increasing fuel consumption [24]. Depending on the application of the thermoelectric generator, for regular passenger cars or trucks and SUV's, TEGs are classified based on their weight. The weight range of thermoelectric generators is roughly between 60 kg to 110 kg. The added weight on a vehicle, because of the installed generator, has a small impact on bringing down the gas mileage [25]. From reliability point of view, thermoelectric materials used in generators may oxidize at higher temperature when they are in contact with the working fluids. It should be noted that a proper method of insulating the sensitive parts from the oxygen has to be considered if not, TEG needs replacement. The cost of repair and installment is more than the amount to be saved in fuel.

Very first generations of thermoelectric generators had transition metals which are especially those of the iron group (Fe, Co, Ni) and other metals (Pt, Ir, Os, Ru, Rh) in the eighth group of the periodic system [26]. Modern thermoelectric devices, depending on the operating temperature range, are made of bismuth telluride (Bi_2Te_3), lead telluride

(PbTe), calcium manganese oxide, skutterudite compounds, or combinations of these thermo-element materials [18]. Reasonable thermal, electrical, and mechanical properties of thermoelectric materials keep them alive in waste heat recovery business. In addition, availability at low cost, harmless to environment, easy fabrication, durability and stability in the temperature range of 20 ˚C to 700 ˚C are some of the important factors which thermoelectric generators for automotive applications must have [25].

Temperature gradient in the exhaust system must be provided for thermoelectric devices to operate. Hot temperature is designed to get from the engine exhaust heat meanwhile the engine coolant is used to cool down the generator and create a reasonable temperature difference. Engine coolant is preferred rather than using ambient air since the coolant has a constant temperature most of the time while engine is running. If engine coolant is used, some considerations should be taken to make sure there is no over loading on the radiator.

1.2 Thermoelectric History

Thermoelectricity was discovered and developed in Europe by academic scientists and researchers starting from 1820 to 1920. The term of thermoelectric comes from the combination of two words “thermo” and “electric”. It conveys a meaning of a device in which electrical energy is produced from thermal energy.

In 1821, Seebeck observed the deflection of a compass needle in a presence of a closed loop two dissimilar conductors when one of the junctions was exposed to heat [27]. At the beginning, Seebeck thought the interaction was a magnetic phenomenon related to the earth’s magnetic system. Since the evidence needed to be proved by him, he started repeating the experiment with different semiconductors but, the interesting mechanism showed him the conversion of thermal energy into electricity in 1821 with an efficiency of about 3%. Afterwards, current flowing in a circuit due to the temperature differenced was called “thermoelectric” effect [28].

12 years later, Peltier, a French physicist, discovered an opposite effect where temperature changes observed in the vicinity of a junction between two dissimilar conductors when a current passed [29]. Although Peltier used the Seebeck effect as a source of weak current in his experiment, he could not reach a conclusion from his observation or relate it to Seebeck effect.

In 1838, German scientist Heinrich Lenz expanded on Peltier’s discovery and described heat transfer phenomena at the junctions depends on the direction of the current flow through the circuit. He illustrated absorption or generation of heat at a junction between two conductors and proved it by freezing water at bismuth-junction. He also heated up the ice until it got melted by reversing the direction of current flow [30].

In 1851, William Thomson, commonly known as Lord Kelvin, found a relationship between Seebeck and Peltier coefficient with the help of a third thermoelectric effect which is called as “Thomson” effect [31].

Up until 1885, the scientists were offering new theories and ideas for thermoelectricity. In 1885, Rayleigh calculated the efficiency of a thermoelectric generator using thermoelectric phenomena in generation of electricity with the help of a temperature gradient. From 1909 to 1911, Altenkirch explained the factors and properties which applicable thermoelectric materials should have [32]. He also mentioned that a worthy thermoelectric material should possess large Seebeck coefficient with low thermal conductivity to keep the heat at the junction and high electrical conductivity to minimize Joule heating.

Starting from 1930, synthetic semiconductors were produced had Seebeck coefficient of more than 100 μV/K. In 1947, Telkes made a thermoelectric generator which had efficiency of about 5% [33]. In 1949, Abram Deforovich Ioffe developed a theory of semiconductors thermoelements followed by the work of Goldsmid and Douglas which was the demonstration of the cooling from room temperature to below 0 °C as a result of refrigeration [10]. He also developed the modern theory of thermoelectricity using the "figure-of-merit" (ZT) concept. Promotion of the use of semiconductors in thermoelectrics and semiconductor physics to analyze results and optimization performance was done by Ioffe [34].

After 1960, a novel thermoelectrics were offered. They consisted of some alternate ingot-shaped negative-type (N-type) and positive-type (P-type) semiconductor connected to each other in series with metal connections. Finally they were sandwiched between thermally conductive but electrically isolated surfaces [35]. The main idea focused on getting electricity from this type of thermoelectrics by maintaining the temperature gradient across the module while the electrical power was delivered by an external load. In the way the N- and P-type unicouples are connected thermally in parallel and electrically in series in order to maintain a temperature gradient across the elements while also providing a usable output voltage, the thermoelectric device started to operate as a generator. On the other hand, when an electric current was passed across the module, the device started acting like a refrigerator by absorbing heat at one face and discharging it at the other end.

The use of the N-type and P-type in TE devices is necessary for the following reasons [36]. First of all, materials which are classified as N-type have impurities that donate electrons to the conduction band. N-type materials are also called as donors that conduct electricity via quasi-free electrons. In opposition, P-type impurities act as acceptors of electrons and conduct through positive charges as it is shown in **Figure 1.2** [37].

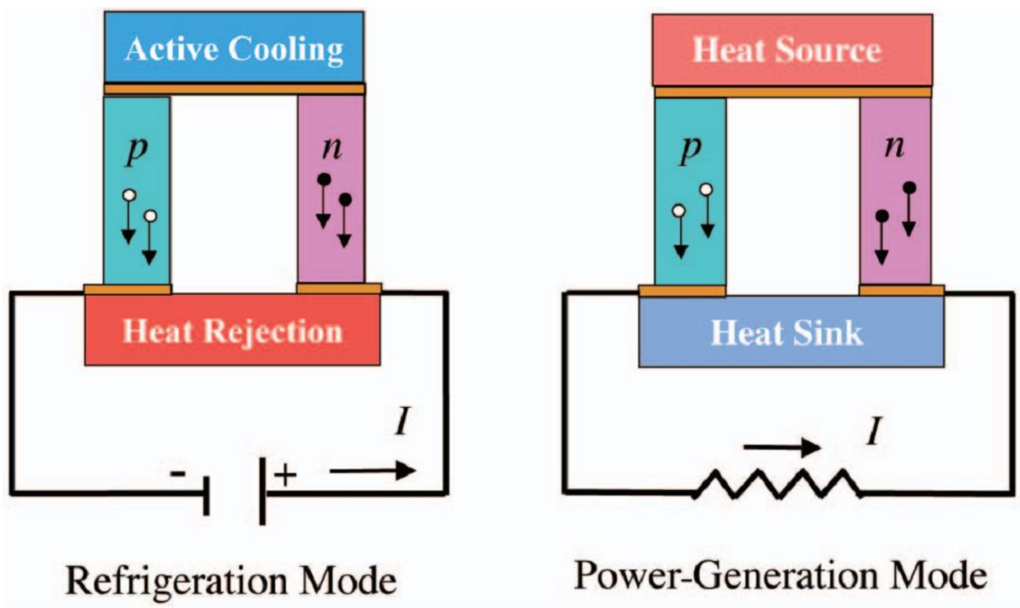

Figure 1.2. Refrigeration of power-generation modes[13]

In 1974, increasing oil prices forced the engineers and scientists to explore different ways to produce energy from inexpensive sources. One of the possibilities on that time was looking at the large scale production of thermoelectrics. One of the restrictions was manufacturing costs of thermoelectric generators. In addition, affordable thermoelectric generator required inexpensive production of substantial amount of semiconductor materials accompanied by a relatively large figure-of-merit. Moreover, there was a concern and general public interest in environmentally clean energy resources which brought a closer look to thermoelectric generator as a large scale convertor of waste heat to electricity [38, 39]. On the other hand, thermoelectric cooling systems were developed such as food refrigerators and air conditioning [40].

In recent years, commercial utilization of thermoelectric devices highly depends on the high figure-of-merit thermoelectric materials [41]. Even though the best models are rough approximations of the materials used in devices, they are capable of delivering a useful vision of the desirable basic properties of materials for refrigeration and generation [42-45]. Many researches and studies have been done on investigating high figure-of-merit materials. However, when it comes to reality and experimental work, due to the dependency of the thermoelectric materials on many factors, the theories and ideas might not come true [46].

1.3 Thermoelectrics operation principles

In the history of the thermoelectric materials some effects, which were found by different scientists, were briefly described. In this section those effects will be expanded more.

In a thermoelectric device there are some reversible and irreversible effects [47]. Reversible effects are Seebeck, Peltier, and Thomson effects. Irreversible effects are classified as Joule heating, thermal conduction, and electrical conduction [48]. These effects are described in the following sections.

1.3.1 Seebeck Effect

Seebeck was a German physicist who discovered the first thermoelectric effect in 1822 [49]. His observation was based on connecting two different semiconductors at their ends while holding the ends at different temperature. This phenomenon led to the voltage development at the end of the junctions. It was found the voltage was a function of material properties and temperature deference between the cold and hot side [48]. Thermocouple was the name of the device that worked on this basis and the conductor components of the thermocouple were called “thermoelements”.

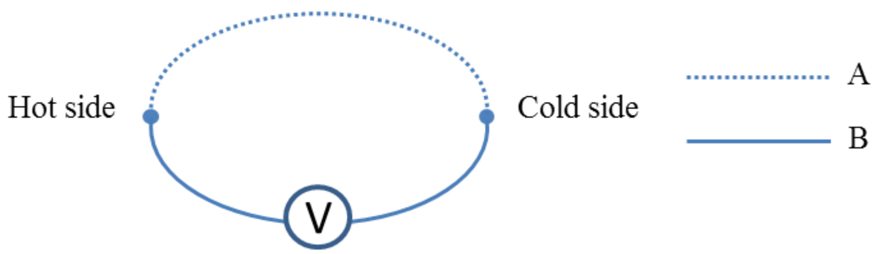

Figure 1.3. Thermocouple simple schematic

Figure 1.3 is schematic of a simple thermocouple made up of thermoelements A and B. The junctions are kept at hot and cold temperatures to develop a voltage across the junctions. The voltage which voltmeter V shows is given by the following equation [50]:

$$V_{HC} = S.\Delta T \tag{5}$$

where S is the Seebeck coefficient and ΔT is the temperature difference between the cold and hot junction. Seebeck coefficient is the function of temperature and material properties of thermoelements.

Equation 5 can be generalized to get the voltage in each segment of the circuit shown in **Figure 1.3.** The theoretical expression for the voltage from arbitrary point **1** to point **2** is:

$$\int_{V_1}^{V_2} dV = \int_{T_1}^{T_2} S.\,dT \qquad (6)$$

S is the Seebeck coefficient of the segment starting from point **1** to point **2**.

For one-dimensional problems, the relationship between the temperature gradient and the voltage gradient with respect to **x** can be written as the following equation.

$$\frac{dV}{dx} = S\frac{dT}{dx} \qquad (7)$$

Or the general form looks like:

$$\nabla V = S\nabla T \qquad (8)$$

1.3.2 Peltier Effect

In 1834, a French physicist found the direction of the heat flow between the cold and hot junctions can be reversed by applying the reverse external or internal current into the thermocouple [51]. The physics of Peltier effect can be described as tendency of the electrical current to drag heat energy into a thermoelectric circuit [48]. The current carries internal energy while flowing from one point to another point of a conductor. When electrical current passes across the junction, from one material having different entropy of transportation to another material with different entropy, heat must be liberated or absorbed at the junction to neutralize the change in the energy of the carriers.

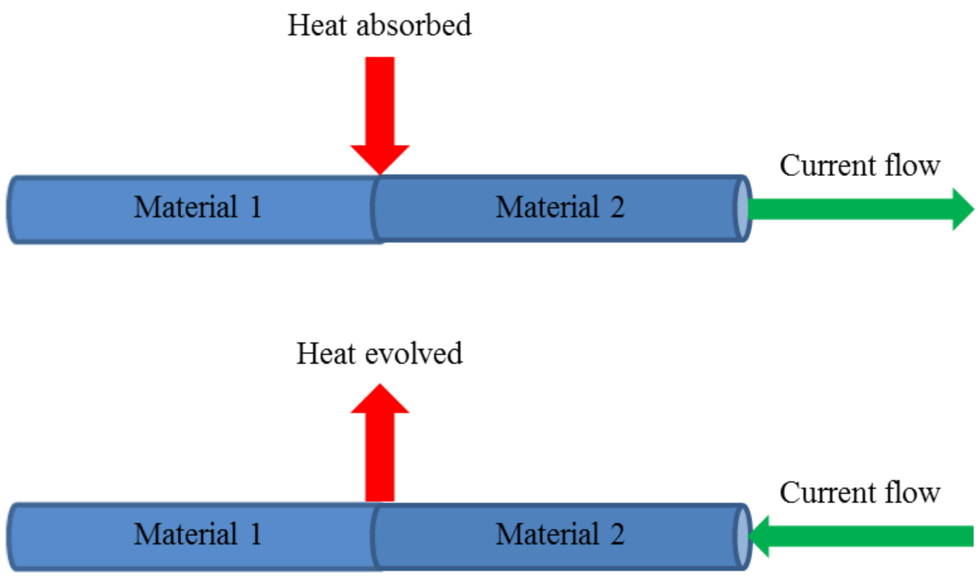

Figure 1.4. Peltier effect

The expression for the magnitude of the heat absorbed or evolved at the cold and hot nodes due to the Peltier effect is given below.

$$Q_P = \pi_{12} I \tag{9}$$

$\boldsymbol{\Pi_{12}}$ is called the Peltier coefficient and $\boldsymbol{I}$ is the current passes through the junction as a function of time [52]. Kelvin relation was offered for mathematical relation of the Peltier coefficient, absolute Seebeck coefficients of thermoelements ***1*** and ***2*** and absolute temperature of the junction [48].

$$\pi_{12} = T_{abs}(S_A - S_B) \tag{10}$$

1.3.3 Thomson Effect

The Seebeck coefficient is not a constant function of temperature in many materials which spatial gradient in temperature can create a gradient in Seebeck coefficient.

Current passed through a gradient in Seebeck coefficient causes Peltier effect. In 1851, this effect, which is called as Thomson effect, was predicted by Lord Kelvin. Thomson effect predicts a heat production rate per unit volume [53]. Thomson effect comes about in a thermoelectric circuit whether the external or internal current in the system generate in a thermoelectric system due to the Seebeck effect [54].

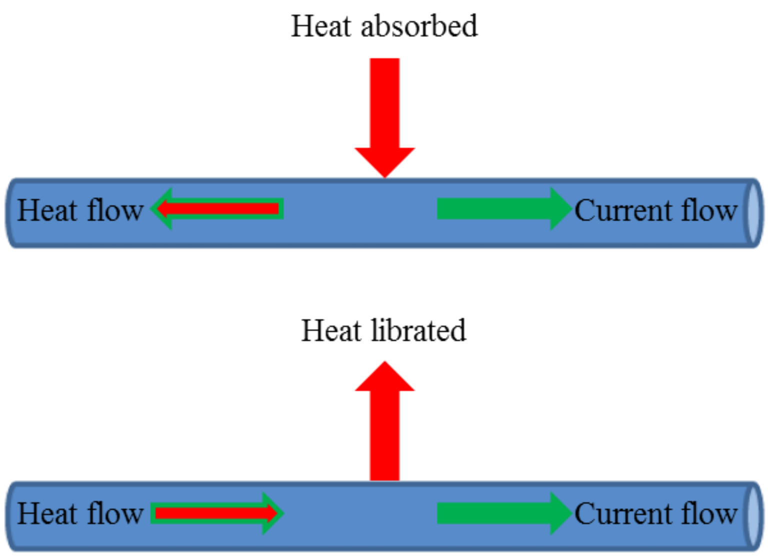

Figure 1.5. Thomson effect

$$\dot{q} = -\kappa J . \nabla T \tag{11}$$

$$\kappa = T \frac{dS}{dT} \tag{12}$$

$$J = k(-\nabla V - S\nabla T) \tag{13}$$

Where $\dot{\boldsymbol{q}}$ is the heat production rate per unit volume, $\boldsymbol{\kappa}$ is the Thomson coefficient, $\boldsymbol{J}$ is the local current density, $\boldsymbol{\nabla T}$ is the temperature gradient, $\boldsymbol{S}$ is the Seebeck coefficient, $\boldsymbol{k}$ is the thermal conductivity and $\boldsymbol{\nabla V}$ is the voltage gradient.

1.3.4 Joule Effect

Joule effect is an irreversible thermoelectric effect which induces internal heating of a current carrying in a conductor. It acts the opposite way of Thomson effect since heat due to the Joule effect is always absorbed in a conductor irrespective of the current direction and temperature gradient existence [48]. The internal heat generation rate $\boldsymbol{Q_J}$ due to the Joule effect and Joule per unit volume $\boldsymbol{q'''_J}$ expressions are listed below.

$$Q_J = I^2 R \tag{14}$$

$$R = \gamma \frac{l}{A} \tag{15}$$

$$q'''_J = \frac{Q_J}{V} = \gamma (\frac{l}{A})^2 = \gamma(\vec{J}.\vec{J}) = \gamma|\vec{J}|^2 \tag{16}$$

Where, $\boldsymbol{I}$ and $\boldsymbol{R}$ are the current passing through the conductor and conductor resistance respectively.

1.3.5 Thermal Conduction

Thermal conduction due to a temperature gradient is internal energy transfer by microscopic diffusion and collisions of particles in a body. The heat transfer rate conducted, due to presence of temperature difference, is given by Fourier law of heat conduction.

$$\vec{q} = -k\nabla V \tag{17}$$

The thermal conductivity can be dependent or independent to the temperature of materials [55].

1.3.6 Electrical Conduction

Voltage gradient in a conductor brings charge flow from high potential to low potential point. Voltage gradient relation with the electric current and thermal resistivity γ is known as Ohm's law [56].

$$\vec{J} = \frac{1}{\gamma}\nabla V \tag{18}$$

2. MATERIALS AND METHODS

2.1 Material Selection

2.1.1 Thermoelectric Material Selection

Thermoelectric materials with high figure-of-merit values are identified by certain criteria such as; semiconducting properties, low thermal conductivity, large Seebeck coefficient, and high electrical conductivity. The selection of high-performance thermoelectric materials requires a balance between conflicting requirements for the optimization of various transport properties. It is also important to know that the thermoelectric materials must be mechanically and chemically stable throughout the entire temperature range of operation [1].

New high-performance thermoelectric materials, including P-type ($Ce_{0.85}Fe_{3.5}Co_{0.5}Sb_{12}$) and N-type ($CoSb_3YbBa$) skutterudite, were developed at NASA's Jet Propulsion Laboratory (JPL). These materials have the potential to achieve the thermoelectric efficiency of about 15% over a 500 °C temperature gradient. Preliminary stability tests have indicated that the maximum operating temperature is approximately 700 °C for the skutterudite [15].

2.1.2 Insulators Selection

The purpose of using the insulator in a thermoelectric couple is electrical isolation of the interconnect circuitry. Ideally, the insulator low electrical conductivity, and low thermal conductivity since it is arranged in series with respect to heat flux across the module. In addition, for minimizing thermal stresses in the module, the substrate have a coefficient of thermal expansion that is compatible with interconnects and the heat exchanger surfaces. Mica and Macor® were selected and used in this project for this purpose.

Mica is used principally in the electronic and electrical industries. Its usefulness in these applications is derived from its unique electrical and thermal insulating properties. Mica could be cut, stamped, punched, and machined to close tolerances. Mica is a good electrical insulator at the same time as being a good thermal conductor.

Macor® is the trademark for a machineable glass-ceramic developed by Corning Inc. It can be machined into any shape using standard machining tools. Macor® can be used in high temperature application and it has high electrical resistivity while providing tight tolerance capability.

2.2 Thermoelectrics Specific Equipment

2.2.1 Material Synthesis

The raw elements used in the synthesis of thermoelectric materials were stored inside an inert atmosphere glove box. To make a sample, individual elements were weighed on an electronic balance and placed inside of a quartz tube. The quartz tube was then removed from the glove box and immediately place on the high vacuum sealing line. The high vacuum sealing line consisted of a Varian Turbo Mini Pumping Station (Model Turbo V70LP) backed by an Edwards RV5 pump. The line can accommodate quartz tubes ranging from 10 mm to 50 mm in diameter and can reach a vacuum pressure of 1e-6 torr.

The quartz tubes were sealed by placing a smaller diameter plug inside the tube and using a torch to flame seal the tube.

2.2.2 High Temperature Furnaces

All of the thermoelectric materials used in the project were synthesized in three Model 3210 ATS Split Tube furnaces. The 1200 ^{o}C furnaces were mounted on a rocking table to enable mixing of the material while a programmable controller automatically controls the temperature. The flame sealed quartz tube was placed inside a 3-zone split tube furnace. Each zone was independently controlled helping the user carefully control the heating and cooling of the sample. After the material had been synthesized, the tube was transferred into the double glove box, where the ingot was powder processed.

2.2.3 Double Glove Box/Powder Processing

The double glove box was used in powder processing of all thermoelectric materials and for loading dies prior to hot pressing. The glove box contains the following equipment for powder processing:

- Motorized mortar and pestle
- Sieve shaker
- A planetary ball mill
- A hydraulic cold press and electronic balance are also located inside the glove box for die loading.

The powder processing of the thermoelectric materials was all done inside the double glove box. After synthesis, the thermoelectric material was transferred into the powder processing glove box and removed from the quartz tube and graphite crucible. The ingots were crushed and ground using the motorized mortar and pestle. After grinding step, the powder was sieved and reground to get the desired particle size. To reduce particle size even further, the powder collected from the grinding and sieving can be milled using the planetary ball mill.

The double glove box was also used to load all the dies for hot pressing. The die was first prepared outside the glove box by lining the inside of the die with a grafoil. The die was then loaded into the glove box and the individual layers of material, including TE materials and insulator, were weighed and cold pressed into the die using the hydraulic press. Once all the layers of materials were loaded, the die was transferred to the hot press.

2.2.4 Hot Press

After cold pressing the materials in the glove box, dies were immediately loaded into the hot press. The Thermal Technology Model HP200-14020-23G hot press can achieve 2200 ^{o}C in vacuum or inert gas atmosphere and has a force capacity of 100 ton. The temperature and force in the 12” diameter × 12” high work zone, which have automatic programmable control, can be controlled simultaneously and independently. Once the die was loaded, the hot press was pumped down for approximately an hour or until it reached 100 millitorr. The hot press was back filled with high purity argon (99.99%) and allowed to pump down overnight (almost 12 hours). Depends on the size of the die and the heating and cooling profile, a typical hot press ran for approximately six hours.

Figure 2.1. Thermal Technology Model HP200-14020-23G hot press

2.2.5 Bell Jar Hot Press

Pressing in the large hot press typically takes 8 hours or longer to complete the heating and cooling cycle. For this reason, a small hot press shown in **Figure 2.2** was manufactured. This small hot press consists of a 1200 Watt band heater, 12 ton jack and is housed inside of a glass bell jar. The top and bottom platens are water cooled and the pressing environment can be back filled with inert gas. A data acquisition system monitors the temperature and pressure within the die. The band heater can easily heat the die up to 700 ^{o}C in approximately 30 minutes. The small hot press reduced the amount of time to press a thermoelectric couple from 8 to 2 hours with no discernable difference in the thermoelectric couple performance.

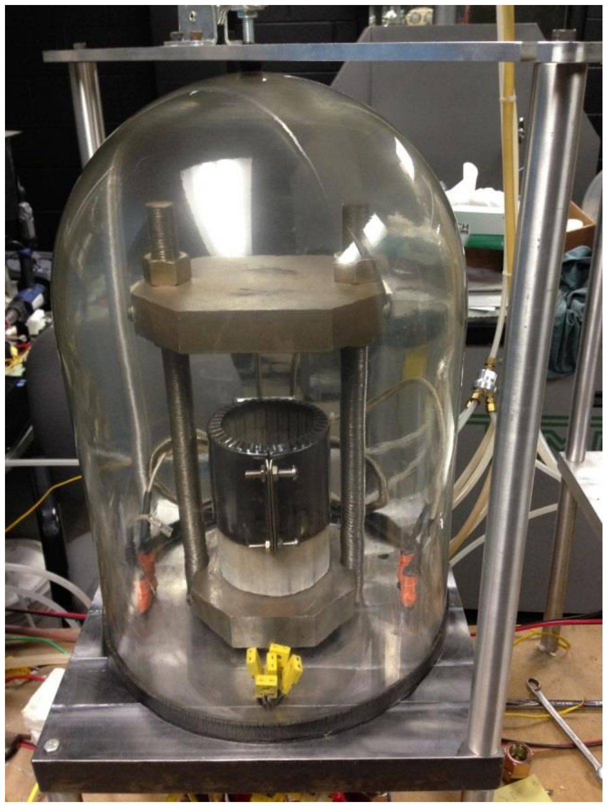

Figure 2.2. Bell jar hot press

2.2.6 N and P Hot Pressed Pucks before Dicing

Prior to dicing, a matched pair of N- and P-type hot pressed pucks, which were crystal bonded to a steel plate, covered by a graphite surface. This allows the material to be cut into precise width and length dimensions.

2.2.7 Grinder/Slicing Machine

KO Lee grinder/slicer, which was used to dice up the thermoelectric material, is isolated inside of a soft wall clean room. The programmable controller and variable high-speed motor can be used to automatically cut hot-pressed material into desired precision rectangular legs (Y and Z axis ± 0.0001 inch).

2.2.8 Machine and Fabrication Shop

To support thermoelectric generator fabrication, engine build and teardown, a machine and fabrication shop, which is located in energy and automotive research laboratory at MSU, is equipped with a CNC mill, lathe, metal cutting and welding equipment.

2.3 Module Development and Fabrication (1^{st} Generation Couple)

First generation thermoelectric modulus was comprised of thermoelectric N- and P-type sections trapped between Macor® insulator and titanium rings. Fabrication typically involves:

- Consolidating thermoelectric powder through standard powder metallurgical processes
- Cold pressing and hot pressing the module to get a homogenous structure
- Pressing the brass ring onto the couple to apply excessive compressive stress
- Integrating suitable thermal insulation

2.3.1 Skutterudite Fabrication

One of the main components in the development of a thermoelectric generator is fabrication of the thermoelectric materials used in the generator. The fabrication includes several different processes which are critical during the fabrication. These processes include synthesis of the skutterudite material, powder processing, cold pressing, and hot pressing [57]. Each process is described as follow.

2.3.1.1 Skutterudite Synthesis

The synthesis production of the skutterudite material involves weighting high purity raw materials, sealing them in an oxygen free quartz tube and then melting them in a furnace to obtain 100 to 200 grams ingots.

Materials for both the N- and P-type skutterudite were weighed inside the single glove box and transferred to a graphite crucible. The total batch size was approximately 100 grams for both the N- and P-type material. The graphite crucible was then placed inside a 1.25” quartz tube and put onto the sealing line. The quartz tubes were left on the sealing line until the pressure reached 3×10^{-6} torr. The quartz tubes were then flame sealed and placed inside a tube furnace. The furnace was then programmed to heat to 1100 ^{o}C at a rate of 10 ^{o}C/min. The material was then held at 1100 ^{o}C for approximately 12 hours and then air quenched. After air quenching, the material was annealed for 48 hrs at 700 ^{o}C for the N-type and 740 ^{o}C for the P-type.

2.3.1.2 Powder Processing

The next step after synthesizing the N and P-type materials is transferring the ingots into an inert gas glove box, where the material is powder processed. The powder processing of both N- and P-type skutterudite has been standardized for both materials.

After annealing, the material was transferred into the powder processing glove box and removed from the quartz tube and graphite crucible. The ingot was then crushed and ground using the motorized mortar and pestle. After grinding for 5 minutes, the powder was sieved for 30 minutes using a 75 μm test sieve. Material that did not pass through the sieve is reground for 5 minutes and sieved again. This process was repeated until approximately 99% of the material has passed through the 75 μm test sieve.

Bulk materials such as metals and ceramics are polycrystalline which means in their structures, there are randomly oriented crystalline regions called grains. The reduction of the grain size in bulk materials has a big impact on the material properties. Bulk materials with grain size less than a micrometer have higher electrical resistance, specific heat capacity, thermal expansion coefficient, mechanical strength, and Seebeck coefficient. On the other hand, small grain size materials have lower thermal conductivity [46].

All the material was then put into a 500 ml stainless steel ball mill jar along with 7-20 mm stainless steel balls. The material was ball milled for 3 hours at the speed of 110 rpm afterwards. Finally, the powder was removed from the jar and placed inside a glass jar until further use.

2.3.1.3 Die Preparation

The loading of the powder material was done inside of the powder processing glove box. The die was first prepared outside the glove box by lining the inside of the die with grafoil. The contacting surfaces of the die bottom and plunger were coated with boron nitride spray and allowed to dry for 15 minutes. **Table 2.1** shows the thickness of the material after cold pressing. The powder of each material was poured into the die and then cold pressed using a hydraulic press located inside of the glove box. This process was repeated until all powders and insulators have been loaded into the die.

Table 2.1. Powder and layers for 1st generation couple

Material	Thickness (mm)
Macor®	1.5
N-SKD powder	1.0
Macor®	2.5
P-SKD powder	1.0
Macor®	1.5

2.3.1.4 Hot Pressing

The hot pressing and metallization of the 1st generation thermoelectric couple has been standardized for both N- and P-type materials. An optimum temperature and pressure during hot pressing has produced strong and robust thermoelectric couples.

All dies were loaded into the hot press immediately after they were removed from the glove box. The hot press was then allowed to pump down for approximately one hour or until it reaches 100 millitorr. It was back filled with high purity argon (99.999%) and allowed to pump down overnight or almost 12 hours. The temperature and pressure profiles for the couple are shown in **Table 2.2**.

Table 2.2. Temperature and force profile for the 1st generation couple hot pressing

Time (min)	30	20	120	60
Temp (^{o}C)	700	700	50	Room
Pressure (MPa)	0	63.5	63.5	0

2.4 Module Development and Fabrication (2nd Generation Couple)

Thermoelectric modulus was comprised of thermoelectric N- and P-type legs connected electrically in series and thermally in parallel. Fabrication typically involves:

- Consolidating thermoelectric powder through standard powder metallurgical processes

- Dicing the thermoelectric legs into the appropriate dimensions
- Bonding thermoelectric legs to a conductive substrate either through cold and hot soldering
- Integrating suitable thermal insulation

2.4.1 Skutterudite Leg Fabrication

One of the main components in the development of a thermoelectric generator is the fabrication of the thermoelectric legs used in the generator. The fabrication includes several different processes that are critical during the fabrication. These processes include synthesis of the skutterudite material, powder processing and hot pressing. Each process is described as below. Skutterudite synthesis and powder processing were followed by the same steps as 1st generation couple synthesized and processed.

2.4.1.1 Die Preparation

The loading of the powder material was done inside of the powder processing glove box. The die was first prepared outside the glove box by lining the inside of the die with grafoil. The contacting surfaces of the die bottom and plunger were coated with boron nitride spray and allowed to dry for 15 minutes. Two pieces of 0.05 mm copper foil, the same diameter as the plunger, were cut and cleaned with acetone. One of the pieces of copper was glued to the die bottom and then inserted into the die. The die along with the foil pieces were loaded into the glove box where the powder materials were loaded.

Table 2.3 and **Table 2.4** show the loading sequence for each hot pressed material. The powder of each material was poured into the die and then cold pressed using a hydraulic press located inside of the glove box. This process was repeated until all powders and foil have been loaded into the die.

Table 2.3. Powder and foil layers for N-type hot pressed ingot

Material	Thickness (mm)
Copper foil	0.05
Titanium powder	0.60
N-SKD powder	6.1
Titanium powder	0.60
Copper foil	0.05

Table 2.4. Powder and foil layers for P-type hot pressed ingot

Material	Thickness (mm)
Copper foil	0.05
Titanium powder	0.30
Cobalt powder	0.30
N-SKD powder	5.9
Cobalt powder	0.30
Titanium powder	0.60
Copper foil	0.05

2.4.1.2 Hot Pressing

The hot pressing and metallization of the N- and P-type materials has been standardized for both materials. An optimum temperature and pressure during hot pressing has produced strong and robust legs. Metalizing both sides in copper during the hot pressing procedure has improved the hot side bonding process.

All dies were loaded into the hot press immediately after they were removed from the glove box. The hot press was then allowed to pump down for approximately one hour or until it reaches 100 millitorr. It was back filled with high purity argon (99.999%) and allowed to pump down overnight or almost 12 hours. One large 12.5” die produces 52 legs that were diced into 3×3×7 mm leg **Figure 2.3**. The temperature and press profiles for both the N and P-type material is shown in **Table 2.5** and **Table 2.6**.

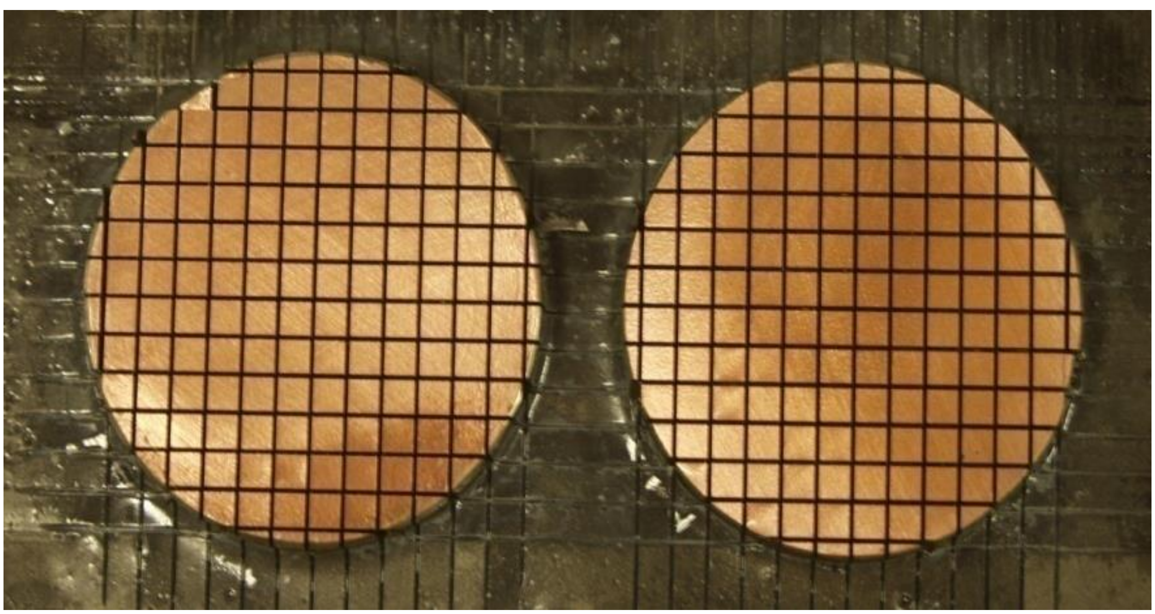

Figure 2.3. Hot pressed N and P-type metalized skutterudite

Table 2.5. Temperature and force profile for the N-type SKD hot pressing

Time (min)	20	20	10	120	20	120
Temp (^oC)	250	500	730	730	600	50
Force (kgf)	0	15500	15500	15500	0	0

Table 2.6. Temperature and force profile for the P-type SKD hot pressing

Time (min)	20	20	10	120	20	120
Temp (^oC)	250	500	660	660	550	50
Force (kgf)	0	15500	15500	15500	0	0

2.4.1.3 Module Tracking and Measurements

As advancements are made and more ambitious power goals are set in the area of thermoelectric generator testing, it becomes desirable to gain greater insight into the process by which the thermoelectric modules are constructed. A certain level of understanding is gained when the performance of the skutterudite material is measured by testing the thermoelectric modules in a generator. However, a greater level of understanding could be attained if the performance of the skutterudite material could be measured at every step of the preparation process. We could discover which steps result in considerable performance degradation.

One indicator of skutterudite performance is the electrical resistivity of the material. As with any thermoelectric material, it is desirable for the material to have a high value of thermal resistivity and electrical conductivity in order to maximize the power output when exposed to a given temperature gradient.

The procedure for creating modules was updated to include measuring the electrical resistance of the couples. Under these new procedures, the electrical resistance of N-type and P-type legs that were cut from the same puck varied considerably, (as much as 50% in some cases) but he electrical resistance of the couple varied only slightly.

To investigate the homogeneity of the pucks a new method of leg tracking and documenting was established. Under this new method, each puck was marked to note the orientation in the hot press. Using this mark, the pucks were then cut using the following diagram to assign a number to each of the legs. Each leg was placed into a numbered glass container to be washed and cleaned afterwards. Finally, the legs were moved into new containers and their electrical resistivity is measured and recorded.

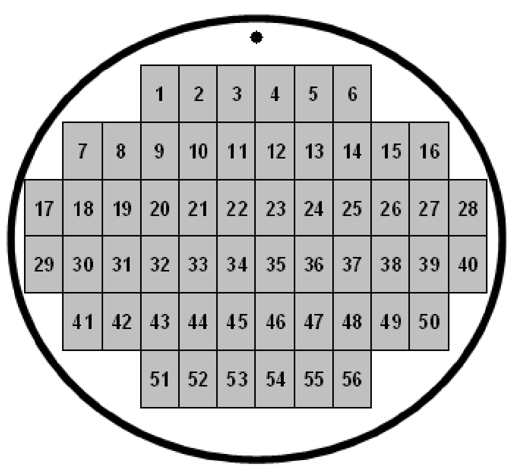

Figure 2.4. Leg tracking and documenting from hot presses pucks

3. EXPERIMENTAL PROCEDURE

3.1 Cylindrical Design of the First Generation Thermoelectric Couple

Traditionally, thermoelectric modules had a flat and rectangular construction which served as building blocks for scalable and flexible TEG architecture. However, that design had a problem from mechanical strength stand point in applications where large temperature gradient applied to the couple. With such a design, which is shown in **Figure 3.1**, the TEG was sandwiched between hot and cold plates which restrict the couple from thermal expansion or contraction [16]. For the purposes of thermoelectric devices design, the mechanical and thermal properties must be characterized. Since the materials used for power generation are brittle and have low strength in tension, existence of tension, big loads, or impacts might disturb the functionality of these devices. In that couple, the risk of a broken couple was found to pose a significant threat to the overall power generation of the entire generator because of big thermal stresses in the P-type leg.

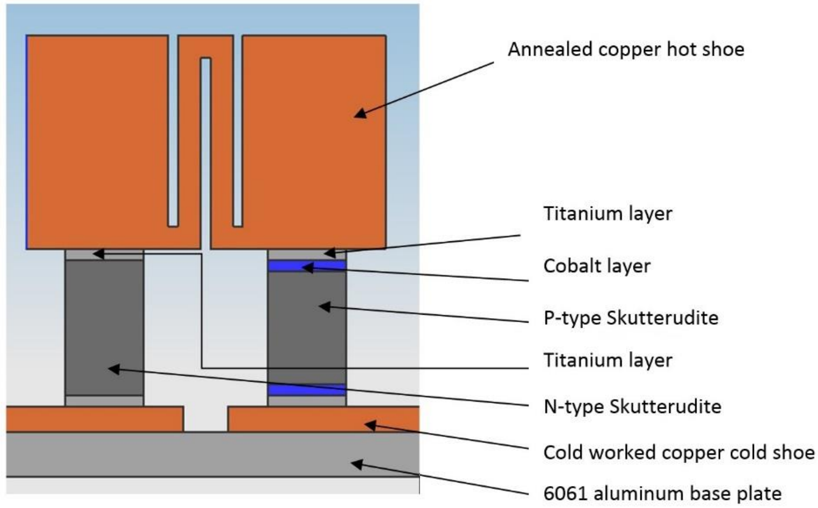

Figure 3.1. First generation thermoelectric components

The new design of the TEG has been developed which is no longer a rectangular shape. The cylindrical design integrates the TE material directly into hot side and cold side heat exchangers. In the new technique, both N- and P-type skutterudite legs, along with the metallization in a single hot press run, were pressed. In the new circular couple design, there is a common hot shoe and a separate cold shoe for both N- and P-type legs. The N- and P-type legs were separated by layers of Macor® insulation with a titanium tube in the inside and a titanium/copper material between the N- and P- cold shoe to electrically isolate the two thermoelectric legs.

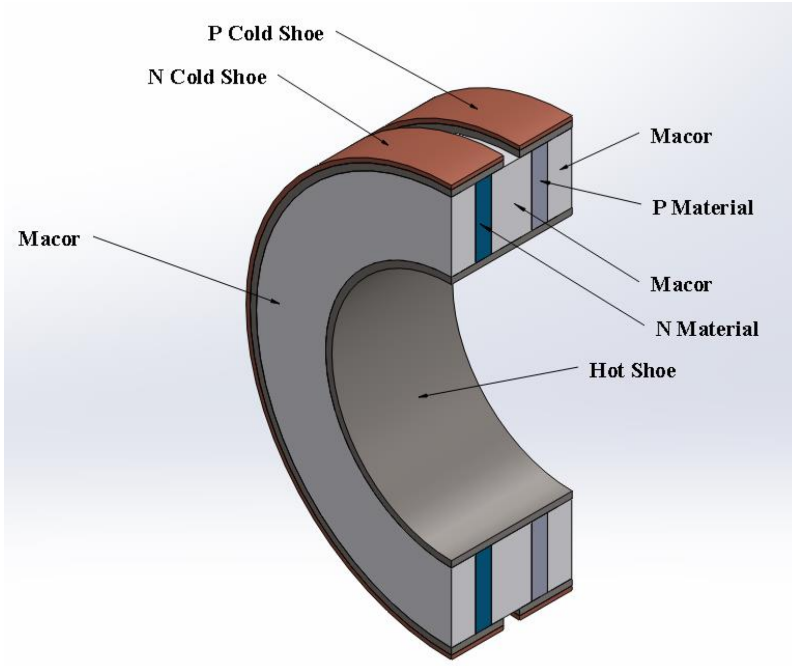

Figure 3.2. Section view of a net shape hot pressed couple

The couple shown in **Figure 3.2** was used as a starting point for the net shape hot pressing with variations in insulation, cold shoe tube thickness and assembly. Several other designs were explored and are shown in **Figure 3.2** to **Figure 3.5**. In **Figure 3.3,** a wider piece of Macor® to separate the N and P-type leg was used and the outsides with a thin layer of Mica insulation were covered. The design of **Figure 3.4** was similar to **Figure 3.2** except the thickness of the cold shoes were increased and a layer of Mica on either side of the N and P legs was located. In **Figure 3.5** a layer of Mica between the two cold shoes was inserted to eliminate the extra machining process of removing material between the two cold shoes. Example of the actual hot pressed couple is shown in **Figure 3.6**.

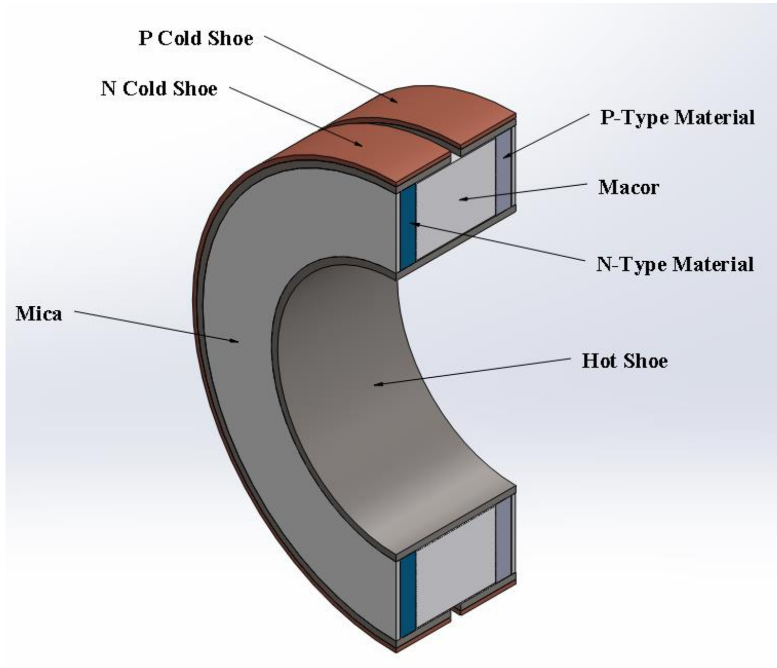

Figure 3.3. Section view of a net shape hot pressed couple

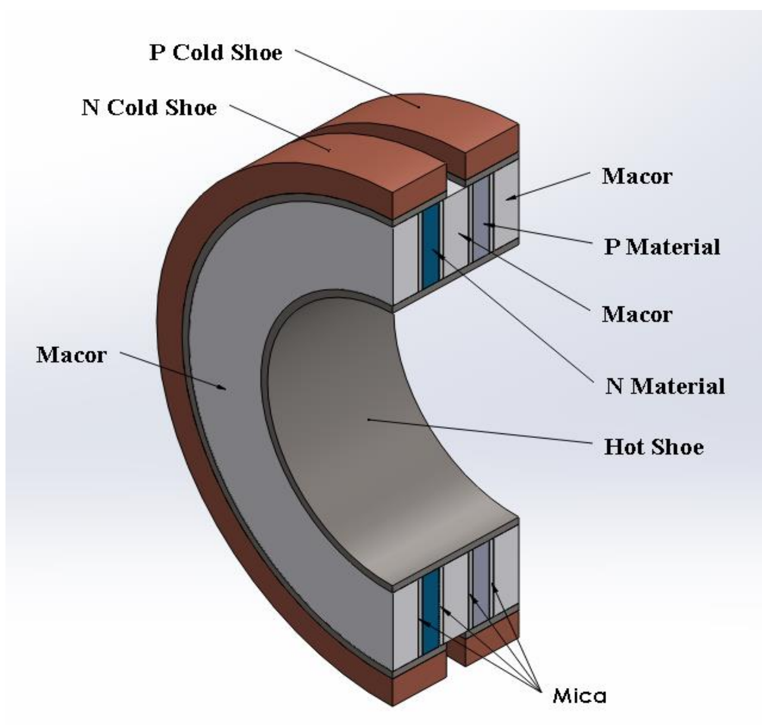

Figure 3.4. Section view of a net shape hot pressed couple

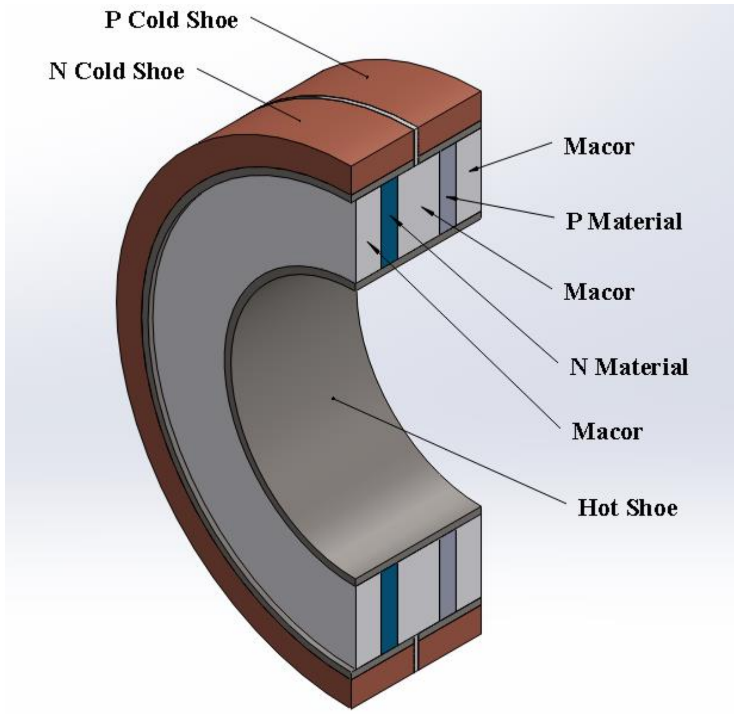

Figure 3.5. Section view of a net shaped hot pressed couple

Figure 3.6. Net shape hot pressed couple

3.1.1 Single Couple Performance Testing

To determine the power production under a heat load, each couple was tested using the test setup shown in **Figure 3.7**. The test fixture was made up of a heat gun with capability of delivering 600 °C air flow to the couple, an aluminum water cooling jacket and a ceramic fixture to hold the couple. The cooling jacket is clamped on the couple which was then bolted onto the ceramic fixture. The setup can be change from one couple to the next fairly quickly. This set up was used for the power output test, cycling test, one hour durability test and long performance testing.

In the setup, the couple was tested by applying a heat load to the center through the jet impingement and a cold load to the outside by the cooling jacket. Temperatures were monitored on both hot and cold sides and voltages were recorded for the total output and the P leg, N leg and the couple using National Instruments and Omega OMB-DAQ-54 data acquisition system. Once the hot side temperature had reached its maximum, a DC load was applied and the output voltage was recorded automatically. To obtain the peak power output of the module, the amperage load was increased until the power output starts to decrease. The peak power mostly happened at the current of 10 Amps.

An example of the voltage and power curve for one couple is shown in **Figure 3.8**. The open circuit voltage, which has no load on it, was 0.066 Volts with a maximum power output of 0.48 Watts at 14 Amps. The temperature on the hot side was 375 ^{o}C and the cold side was 125 ^{o}C for a time step of 20 minutes. A regression equation of the voltage and amperage curve provides the overall resistance of the module. The resistance of that module was 2.4 mΩ. A second test was run, however the power output decreased significantly indicating cracking is most likely occurring between the skutterudite and titanium interface or specifically in the skutterudite.

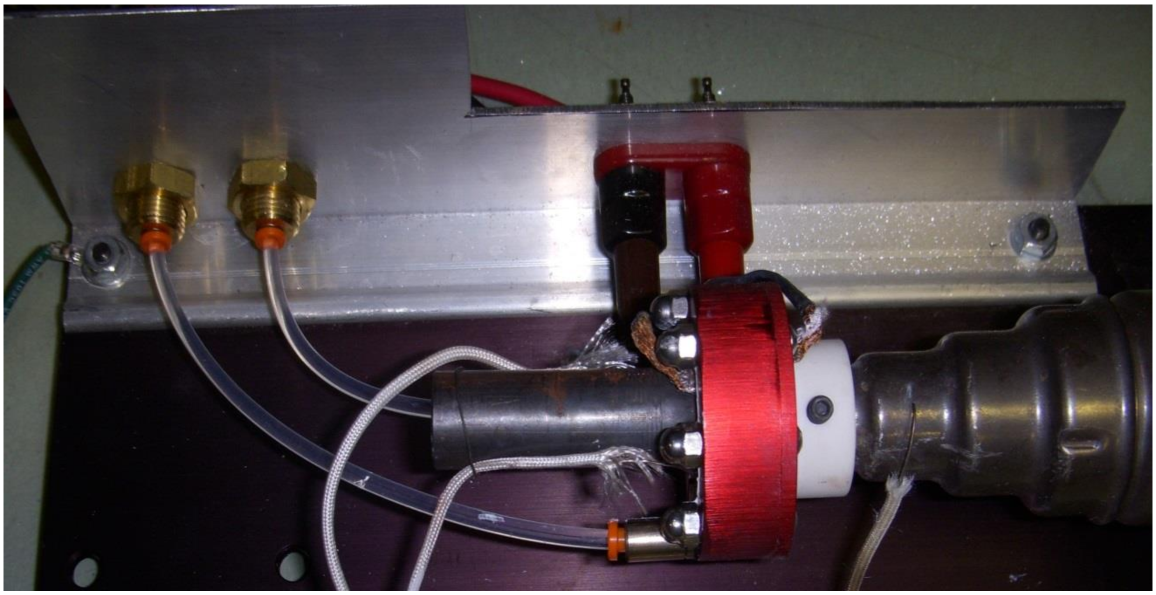

Figure 3.7. Single couple testing setup

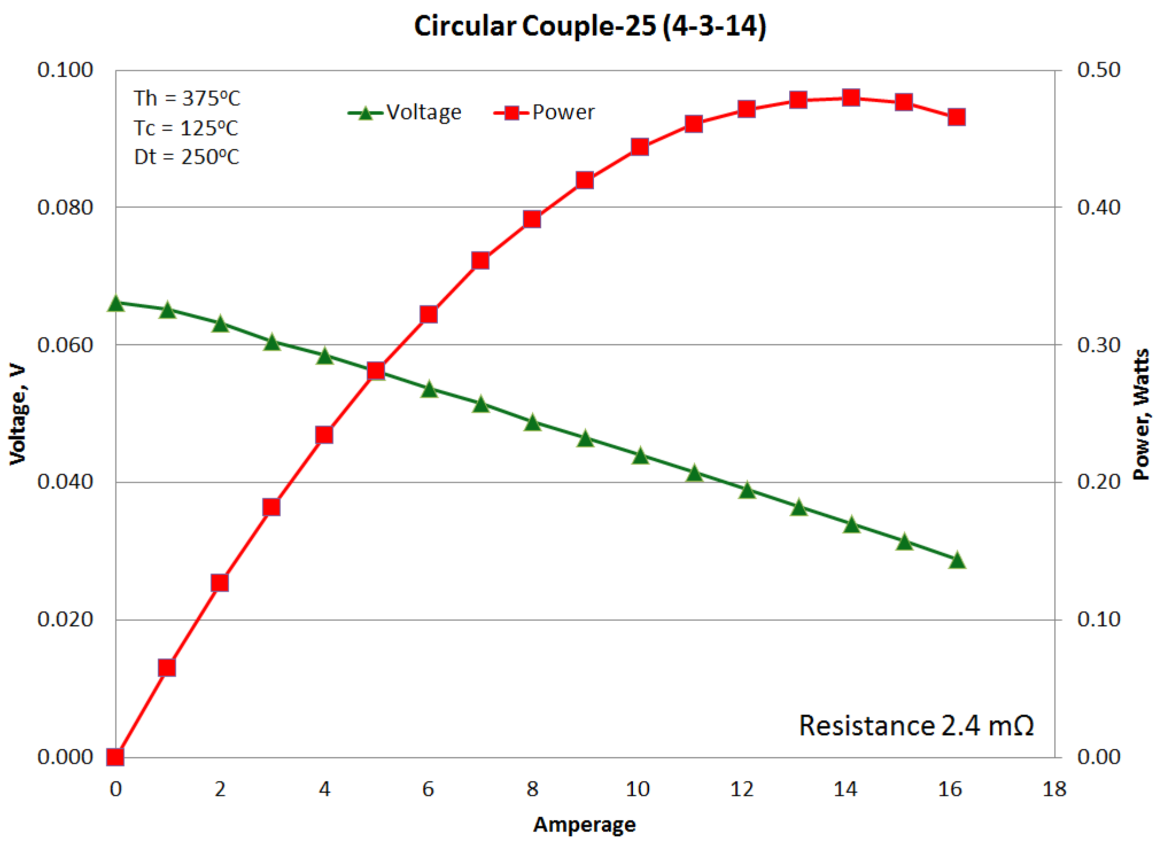

Figure 3.8. Voltage and power output for a net shape hot pressed circular couple

3.1.2 Thermoelectric Couple Redesign

In the initial design of the couple, the outer copper tube was hot pressed along with all of the other materials. Based on past experience, copper when hot pressed at high temperatures anneals and results in softening. The compressive forces that the outer copper ring was to provide radially to the couple were nonexistent. For this reason, the design of the couple was changed and a new design put together and assembled. In the new design, the couple was hot pressed only with titanium tubing on the inside and outside. The outside titanium tube was then split by machining a small groove in the tube which is shown in **Figure 3.9**. A brass ring that has a 0.001 to 0.002 inches interference fit was then pressed onto both the N and P side with a layer of Mica insulation in between to electrically isolate them as it is shown in **Figure 3.10**. The pressing of the brass rings was done by cooling down the couple to -60 ^{o}C and heating up the brass ring up to 100 ^{o}C. A finite element analysis of the hot pressing, pressing of the brass rings and simulation of the testing procedure will be discussed in later sections.

Figure 3.9. Net shape hot pressed couples with inner and outer titanium tubing

Figure 3.10. Net shaped hot pressed with a brass ring pressed on

3.2 New Design of Cylindrical Thermoelectric Couple (2nd Generation)

While the performance of the circular couple showed promising, the structural integrity of the P-type leg resulted in radial and circumferential cracking caused by excessive tensile stresses. The existence of tension, large loads, or impacts might disturb the functionality of the thermoelectric couples. Several different methods were studies, as they will be mentioned in chapter 4, in an effort to reduce the cracking; however none of the techniques solved the problem [58].

Using previous square leg technology, which has fewer residual stresses created during hot pressing, and compression couple technology, a new circular couple was developed. This couple incorporates the best technology from both previous designs. An assembled and exploded view of the new couple is shown in **Figure 3.11**. The couple consists of 4

N-type legs, 4 P-type legs, 2 brass cold shoes, a common hot shoe and a layer of Mica insulation.

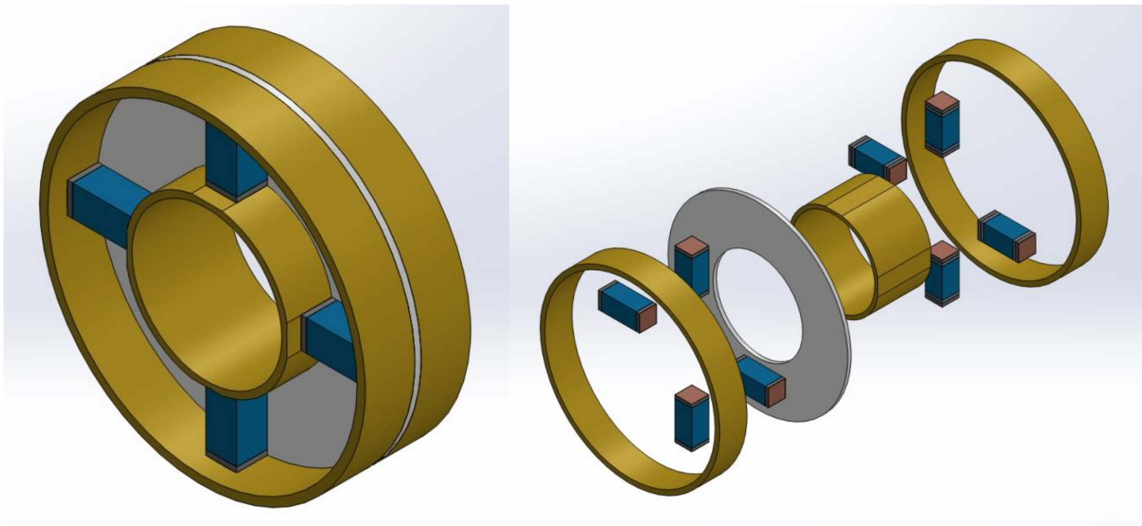

Figure 3.11. Assembled and exploded view of the new circular couple

The couples have been assembled using two different methods. The first method used involves bonding the legs to the hot shoe using a high temperature braze paste (651 ^{o}C) and using a low temperature solder (200 ^{o}C) to bond the legs to the cold shoes. The second method uses a low temperature solder (200 ^{o}C) to bond both hot and cold shoes. Examples of the assembled couples are shown in **Figure 3.12**.

Figure 3.12. Assembled new circular couple with square legs

Several variations of the couple were tested for both performance and the effect of thermal cycling. The variations in couple design included, high and low temperature bonding of the skutterudite legs to the hot shoe and different material for the hot shoe design. The variations in the hot shoe design included:

- Brass (Low temperature solder)
- Brass (High temperature braze)
- Brass with a steel insert (Low temperature solder)
- Copper thicker walled (No Solder)
- Brass with a graphite insert (Low temperature solder)
- Inconel 600 (Low temperature solder)

In addition to the hot shoe design, the method to heat the hot shoe using jet impingement was also refined. Details in the design of the jet impingment and the flow patterns of the hot gas will be presented in a later section.

3.2.1 Two Couple Performance Testing

To determine the power production under a heat load, two couples, which were bonded together, were tested using the test setup shown in **Figure 3.13**. The test fixture was made up of a heat gun with capability of delivering 600 °C air to the couple, an aluminum water cooling jacket and a ceramic fixture to hold the couple. The cooling jacket is clamped on the couple which was then bolted onto the ceramic fixture. The setup can be change from two couples to the next assembly quickly. This set up was used for the power output test, cycling test, one hour durability test and long performance testing.

In this setup, the couple was tested by applying a heat load to the center through jet impingement and a cold load to the outside by the cooling jacket. Temperatures were monitored on both the hot and cold side and voltages were recorded for the total output and the P leg, N leg and the couple using a small data acquisition system. Once the hot side temperature had reached its maximum, a DC load was applied and the output voltage was recorded automatically. To obtain the peak power output of the module, the amperage load was increased until the power output starts to decrease. The peak power mostly happened at the current of 10 to 14 Amps.

An example of the voltage and power curve for one couple is shown in **Figure 3.14**. The open circuit voltage, which has no load on it, was 0.18 Volts with a maximum power output of 1.38 Watts at 14 Amps. The temperature on the hot side was 401 ^{o}C and the cold side was 28 ^{o}C for a time step of 20 minutes. A regression equation of the voltage and amperage curve provides the overall resistance of the module. The resistance of that module was 6.1 mΩ. A second test was run, however the power output decreased indicating detachment between the legs and brass rings.

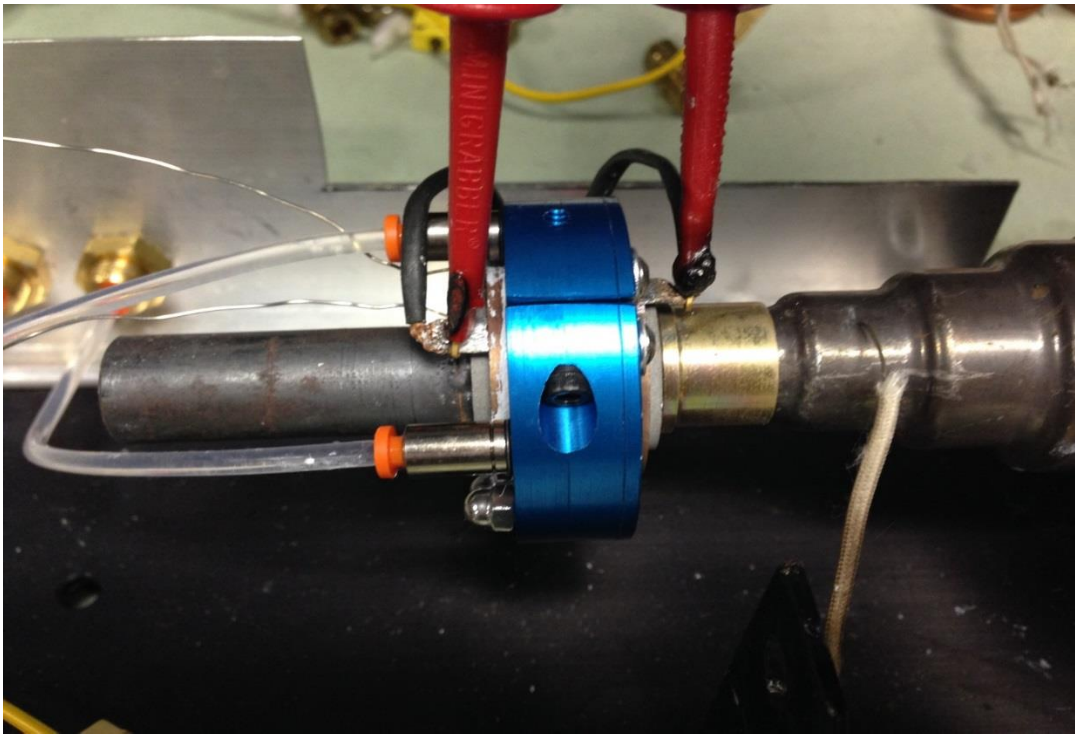

Figure 3.13. Two couple testing setup for 2nd generation couple

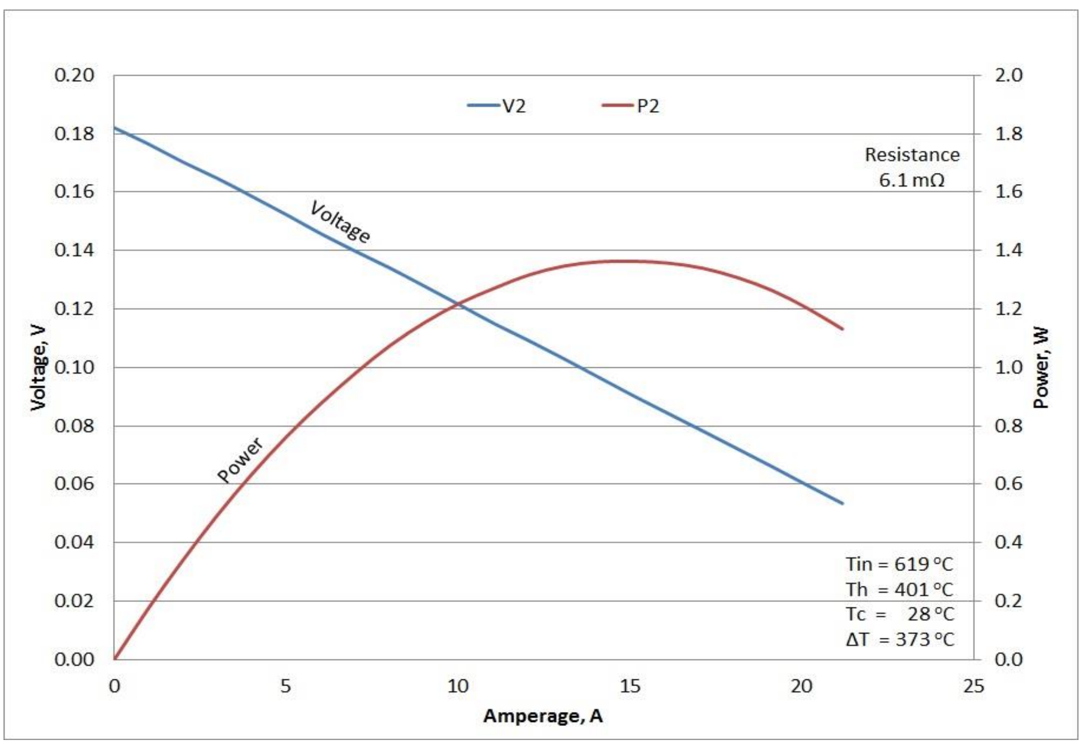

Figure 3.14. Voltage and power output for two couple assembly

3.3 15 Watts Thermoelectric Generator

A prototype TEG was designed which consists of common coolant input and output ports as well as exhaust intake and output ports as it is shown in **Figure 3.15**. The basic shell of the TEG is designed to hold 4 modules with 5 couples per module (**Figure 3.16**). The couples used in the 15 watts TEG were all 2nd generation couples. All parts of the outer housing were made from 304 stainless steel and were welded together to form a solid and leak-free heat exchanger on the cold side of the modules. Based upon performance results from module testing, the prototype TEG was expected to produce 15 watts with an output voltage of 1.0 and current of 15.0 amps.

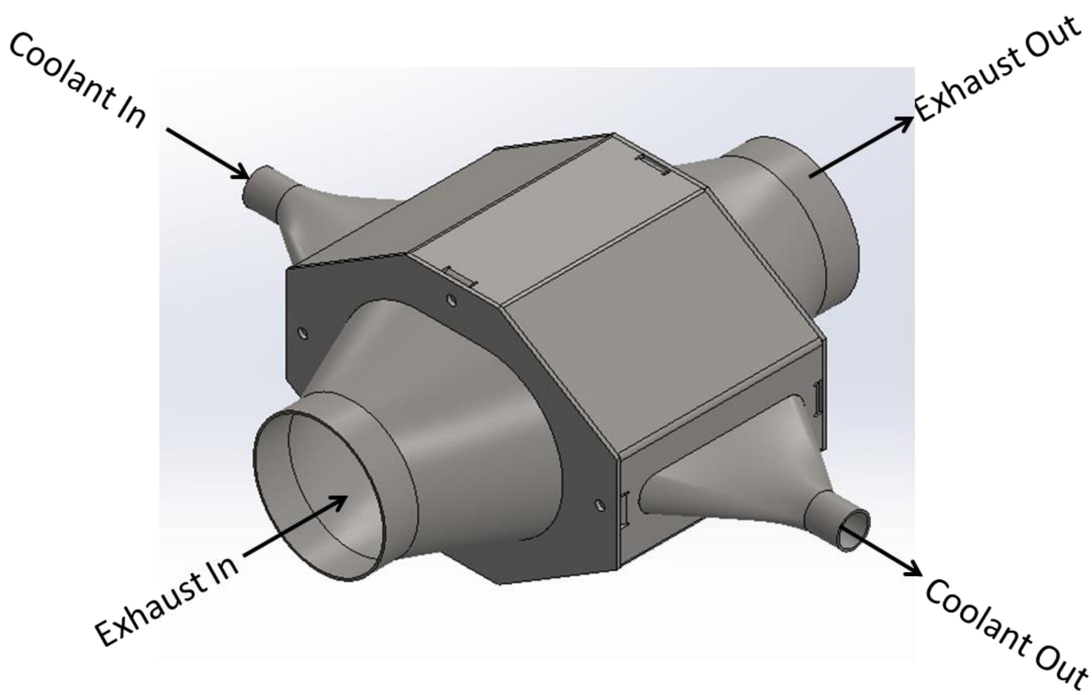

Figure 3.15. CAD model of the prototype TEG

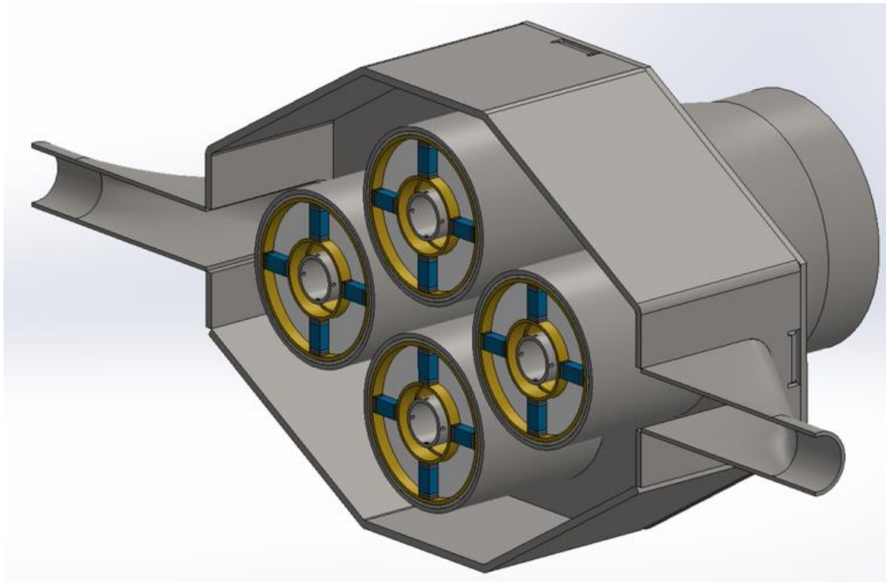

Figure 3.16. Section view of the prototype TEG

3.3.1 Couples

A total of 20 individual couples were assembled and measured for internal resistance (**Figure 3.17**). The measured resistance ranged from 1.9 to 2.3 mΩ. Each couple consists of 4 N- and P-type legs, a common Inconel 600 hot shoe, two brass cold shoes, and a layer of mica insulation to separate the cold shoes electrically and physically.

Figure 3.17. Twenty assembled couples for use in prototype TEG

3.3.2 Modules

The twenty couples were assembled into 4 modules by using low-temperature solder to connect 5 couples in series as it is shown in **Figure 3.18**. A mica disc was also added between each couple to insulate the void area created when connecting the couples together. Modules were assembled and pressed into precision-machined anodized aluminum tubes. The purpose of the anodized aluminum tubes is electrical isolation of the modules from the cooling housing. Electrical leads were added to each end of the module, and mica plugs were pressed into the aluminum housing (**Figure 3.19**).

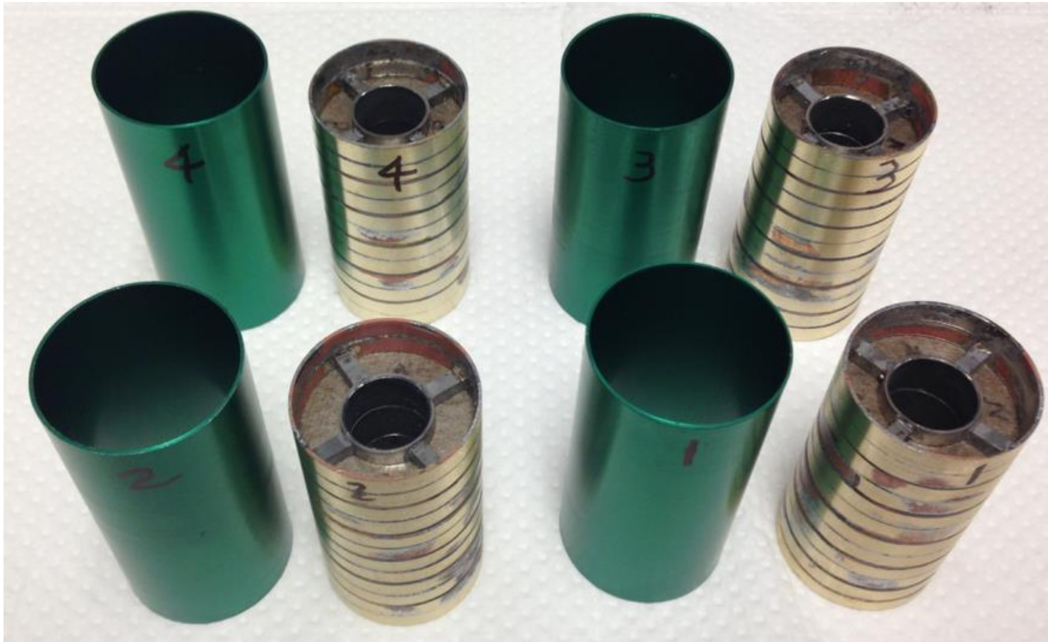

Figure 3.18. Assembled modules with anodized aluminum tubes

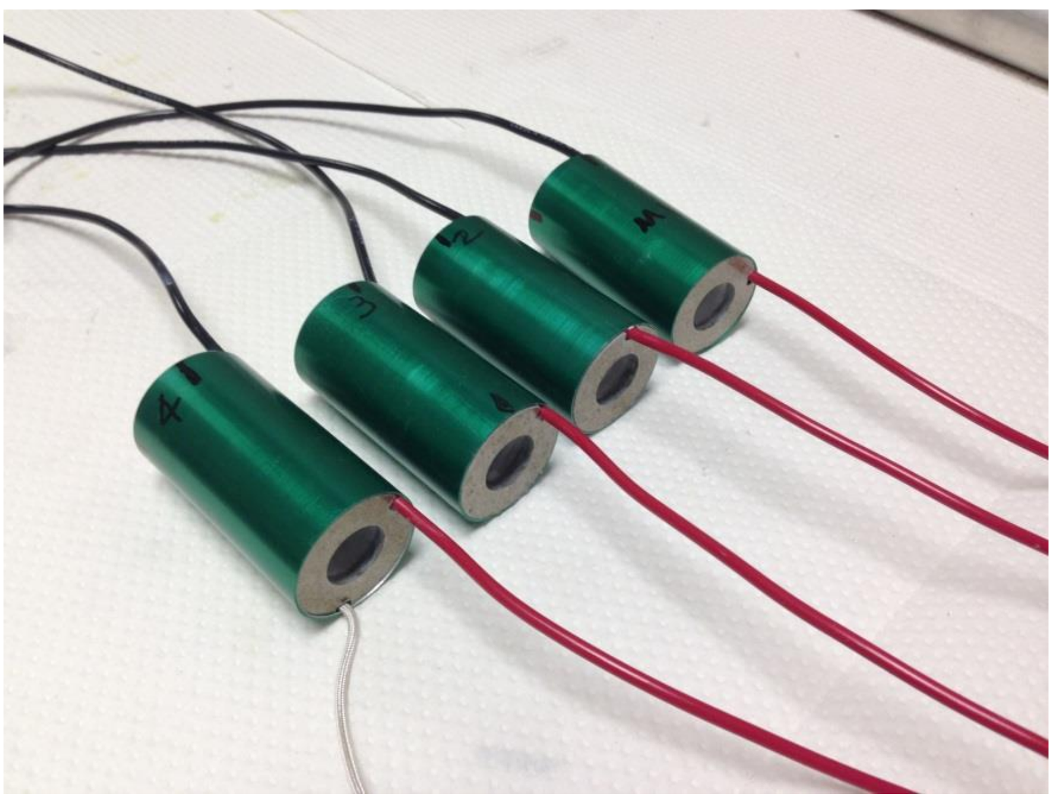

Figure 3.19. Assembled modulus with electrical leads

3.3.3 Cooling Housing

The cooling housing was assembled with 304 stainless steel and TEG welding at each seam. The four cooling tubes in the center of the cooling housing were press-formed after welding to insure a slight press fit with the modules.

Figure 3.20. Assembled TEG cooling housing

3.3.4 Jet Impingement Assembly

Jet impingement is an attractive heating/cooling mechanism due to the capability of providing high heat transfer rates. The high heat transfer rates is the result of impinging the airflow through a series of small orifices or holes directed onto the surface of the hot shoes. Jets are deployed in different shapes, round or square, that impact the eventual heat transfer from the impinged jet surfaces [59]. An impingement array is comprised of a jet plate typically having holes producing the impingement jets. The jets strike the surface to make it hotter or cooler. Impingement jets can be either be air- or liquid-powered [60].

The jet impingement assembly consisted of 4 stainless steel jet impingement tubes, a face plate and intake exhaust pipe (**Figure 3.21**). The jet impingement holes were located on each tube so that the air jet would be directly in line with each thermoelectric leg in the assembly. Each tube was welded to the face plate, as was the intake exhaust tube. The entire assembly was then bolted to the cooling housing with four machine screws.

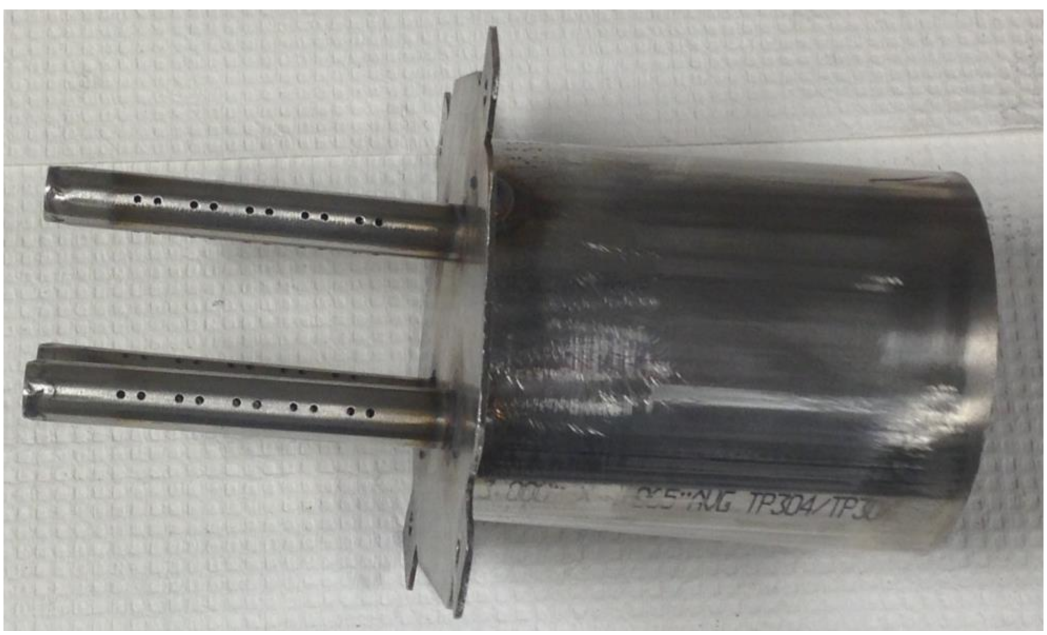

Figure 3.21. Jet impingements assembly

3.3.5 TEG Assembly on the Air-Torch

The final assembly of the prototype TEG is shown in **Figure 3.22**. A total of 7 thermocouples were used to monitor system temperatures during testing. These included: air torch thermocouple, input and output exhaust thermocouples, cooling water input and output thermocouples, and a representative hot and cold shoe thermocouple in the first and last couple. Air flow rate, coolant flow rate, voltage output on individual modules and amperage load applied during testing were also recorded. A National Instruments (NI)/Omega data acquisition system was used to monitor temperatures, flow rates and voltages.

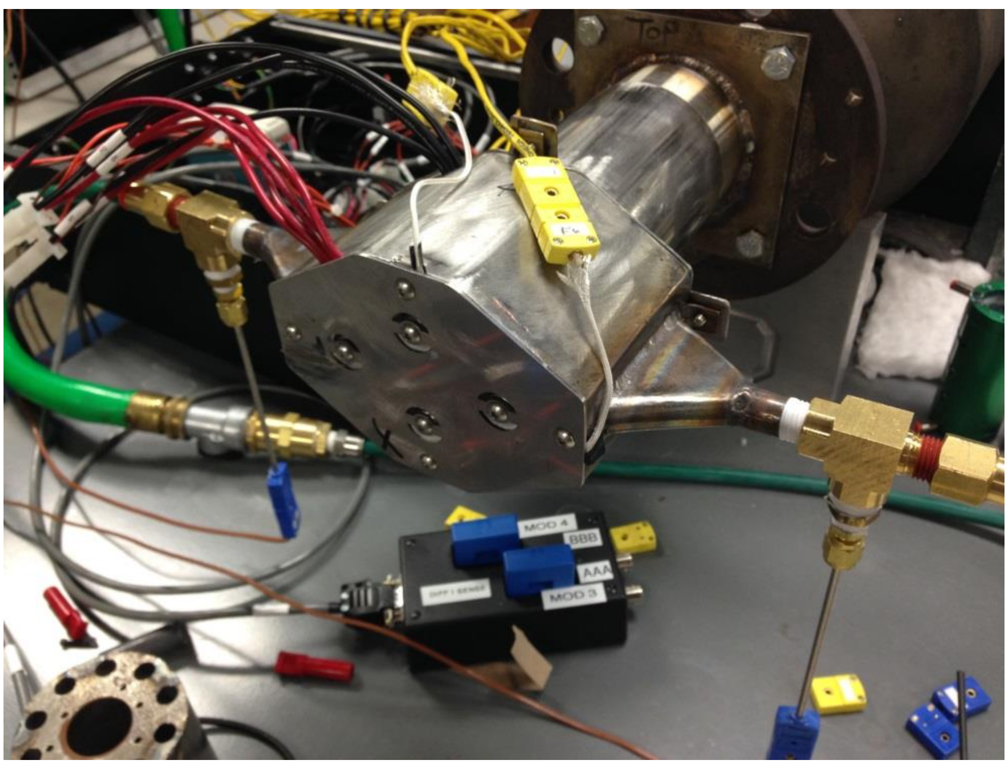

Figure 3.22. TEG assembly coupled to the Air-Torch with system monitoring

4. RESULTS AND DISCUSSION

4.1 Finite Element Modeling

The finite element method is a numerical technique which is widely being used to get a reasonable and accurate solution of the partial differential equations that governs many physical and engineering problems. The finite element method originated in mid 1950s when engineers and scientists had difficulties in solving complex models and geometries via finite difference method [61].

A typical work out of the finite element method can be done in two steps [62]:

1) Dividing the domain problem into a collection of subdomains that each of the subdomains represented by a set of mathematical equations to the original problem in a local system assigned for each of elements.
2) Combining all sets of equations into a global system of equations

Applications of finite element modeling are broad because of several advantages such as [63]:

- Capable of solving problems with complex geometries
- Inclusion of dissimilar material properties
- Ability to capture local effects
- Easy representation of the total solution
- Enhanced design and better insight into critical design problems
- Virtual prototyping
- A fast, reliable and less expensive design compare to real experiment

- Fewer hardware prototype

In the past decades, finite element applications were restricted to structural problems, but gradually heat conduction and fluid dynamic problems were covered and solved mostly by this method [64].

A finite element analysis of the TEG was performed by ABAQUS 6.12-3 to investigate the materials interactions occur during manufacturing and performance of the TEG. With the advantage of using finite element analysis, temperature distribution and state of stresses within the TEG can be calculated by solving coupled thermal-displacement equations.

Fully coupled thermal-stress analysis is needed when stress analysis depends on the temperature distribution while temperature distribution depends on the stress solution. For instance, some problems may include significant heating due to inelastic deformation of the material which changes the material properties. Moreover, contact conditions exist in some problems where heat conducted between surfaces may depend strongly on the separation of the surfaces or the pressure transmitted across the surfaces. For these cases and similar problems, thermal and mechanical solution should be obtained simultaneously rather than sequentially.

An exact implementation of Newton's method involves a non-symmetric Jacobian matrix which is written below

$$\begin{bmatrix} K_{uu} & K_{u\theta} \\ K_{\theta u} & K_{\theta\theta} \end{bmatrix} \begin{Bmatrix} \Delta_u \\ \Delta_\theta \end{Bmatrix} = \begin{Bmatrix} R_u \\ R_\theta \end{Bmatrix} \tag{19}$$

Where $\boldsymbol{\Delta_u}$ and $\boldsymbol{\Delta_\theta}$ are the corrections to the incremental displacement and temperature respectively, $\boldsymbol{K_{ij}}$ are submatrices of the fully coupled Jacobian matrix, and $\boldsymbol{R_u}$ and $\boldsymbol{R_\theta}$ are the mechanical and thermal residual vectors.

For some cases, fully coupled analysis in the sense that the mechanical and thermal solutions evolve simultaneously, however the weak coupling between the two solutions makes the off-diagonal components ($\boldsymbol{K_{u\theta}}$ and $\boldsymbol{K_{\theta u}}$) of the fully coupled Jacobian matrix small compare to the other components in the diagonal submatrices. A less costly solution can be obtained by setting the off-diagonal submatrices to zero to get an approximate set of equations.

$$\begin{bmatrix} K_{uu} & 0 \\ 0 & K_{\theta\theta} \end{bmatrix} \begin{Bmatrix} \Delta_u \\ \Delta_\theta \end{Bmatrix} = \begin{Bmatrix} R_u \\ R_\theta \end{Bmatrix} \tag{20}$$

This approximation shows the mechanical and thermal problems can be solved separately with fewer equations. This modified form of Newton's method does not affect the solution accuracy since the fully coupled effect is considered in the residual vector $\boldsymbol{R_i}$ at every increments in the time domain. However, the rate of the convergence is not quadratic anymore and strongly depends on the magnitude of the coupling effects. Bigger coupling effect needs more iterations to achieve equilibrium rather than the exact implementation of the Newton's method [65].

4.1.1 Finite Element Analysis of the First Generation Couple Design

The components of the couple used in the finite element modeling are shown in **Figure 4.1** to **Figure 4.3.**

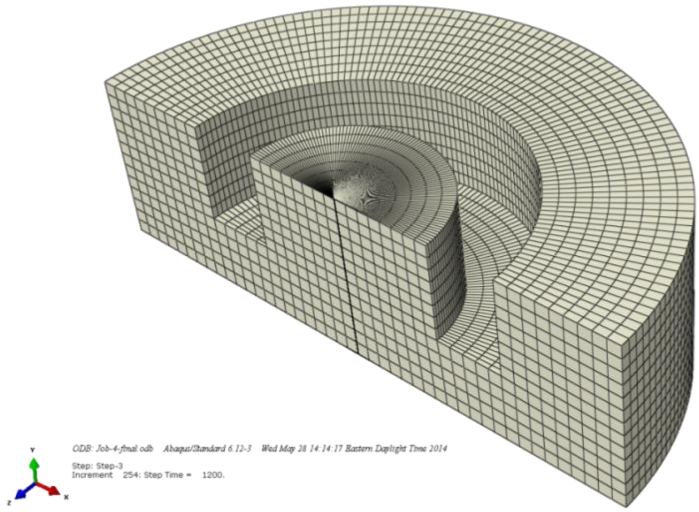

Figure 4.1. Section view of the graphic die

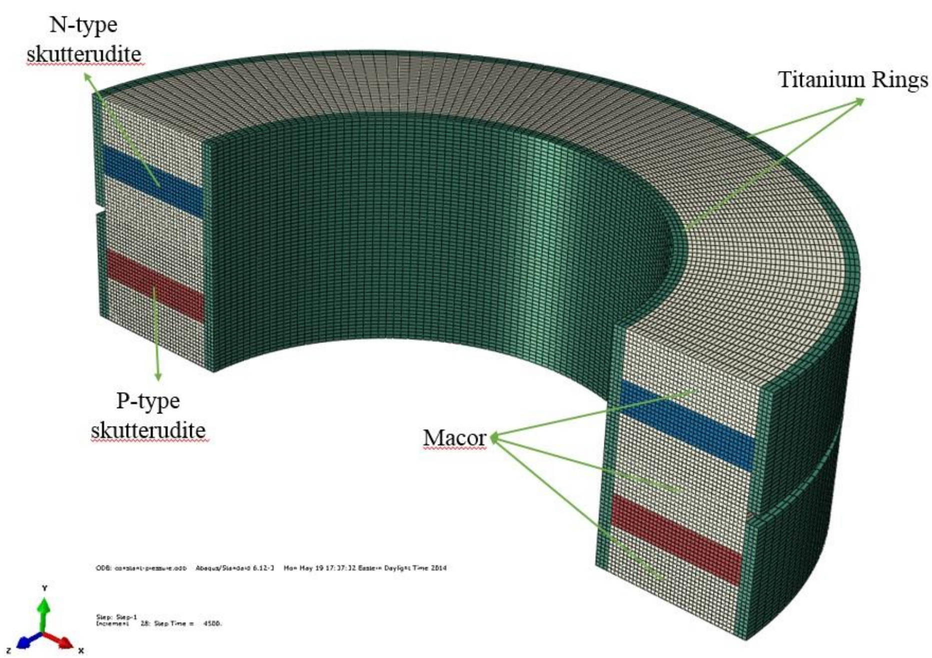

Figure 4.2. Section view of the thermoelectric couple

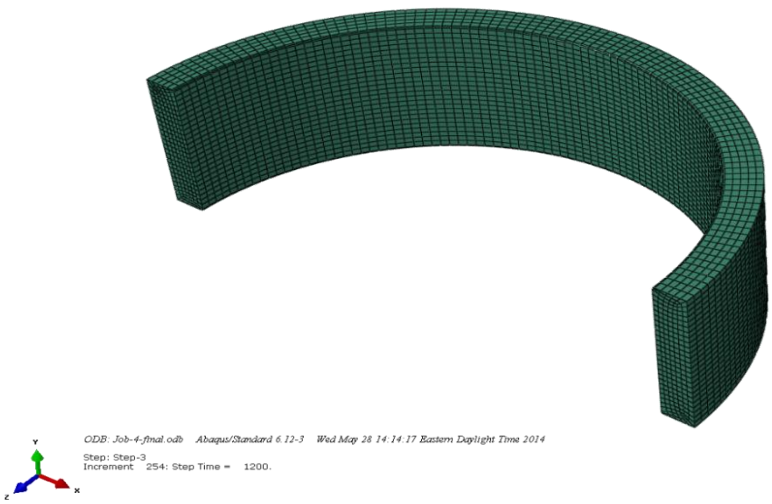

Figure 4.3. Brass ring

The model consists of inner and outer titanium rings with N- and P-type skutterudite materials and Macor® ceramic material layered in between the titanium rings. The titanium rings and brass ring have 0.016 and 0.06 inches thickness respectively. The couple was modeled as an axisymmetric deformable shell having an inside radius of 0.297 inches and an outer radius of 0.50 inches to the outside surface of the titanium ring as shown in **Figure 4.2**. The overall thickness of the TEG couple used for FE analysis is 0.2988 inches. The material properties including mechanical and thermal properties are summarized in the **Table 4.1**. True stress-strain data of the skutterudite, which are necessary to model the plastic behavior of the couple, are not included in the table below but all the essential information were considered to get a trustworthy simulation. True stress-strain data were calculated from engineering stress-strain data provided by NASA JPL. For the skutterudite materials included here, the Young's modulus, Poisson's ratio, and the coefficient of thermal expansion used, all measured by Schmidt et al [12, 15].

Table 4.1. Material properties of the thermoelectric couple components

	E(MPa)	υ	Density ρ (kg/m^3)	Thermal Expansion α (1/C)	Thermal Conductivity κ (W/m-C)	Specific Heat C_p (J/kg-K)
N-SKD	1.27e+5 (500˚C) 1.41e+5 (-60˚C)	0.231	7570	1.20e-5 (500˚C) 8.50e-6 (-60˚C)	4.5	140
P-SKD	1.13e+5 (500˚C) 1.31e+5 (-60˚C)	0.242	7570	1.50e-5 (500˚C) 1.28e-5 (-60˚C)	2.7	140
Macor®	6.70e+4	0.29	2491	1.14e-5	1.46	790
Titanium	1.20e+5	0.34	4500	8.90e-6	17	528
Copper	1.14e+5	0.31	8920	1.17e-5	387	385
Mica	1.72e+3	0.40	2900	3.00e-5	0.54	500
Graphite	1.03e+5	0.30	1780	5.60e-6	70	760

In the analysis part, transient module instead of steady-state was preferred since the temperature could be monitored in every time increment. Boundary conditions were defined in the way to mimic the real physics of the problem. At the beginning, since the model is based on the axisymmetric simulation to reduce the computation time, the graphite die was constraint from any movement along the z axis but it was free to expand or move in the radial direction.

Before starting the pressing simulation of the brass ring onto the thermoelectric couple, the base of the couple was locked from moving in z direction. In addition, in the heat transfer step analysis, the brass and the couple were not allowed to move in z direction and they were locked on their center line. Defining the boundary conditions on the center line of the module, it allowed the couple to expand along z direction and kept it symmetry but it didn’t allow its movement along the axial direction. In the mesh menu, all the meshes were defined as a 4-node axisymmetric thermally coupled quadrilateral bilinear displacement and temperature (CAX4T) free mesh after choosing the base size as 0.0001 m.

All the contacts were in the form of surface-to-surface contact because of the physics of the problem. All the friction and gap conduction coefficients were defined. On the other hand, since effect of radiation was negligible to change the heat transfer rate and temperature distribution, it was skipped from simulation.

For the hot pressing step, pressure of 63.5 MPa was applied on the thermoelectric couple. It was assumed the pressure started from zero and reached its maximum value after 60 seconds. Afterwards, it was held for 4000 seconds and then gradually reduced to zero within 500 seconds.

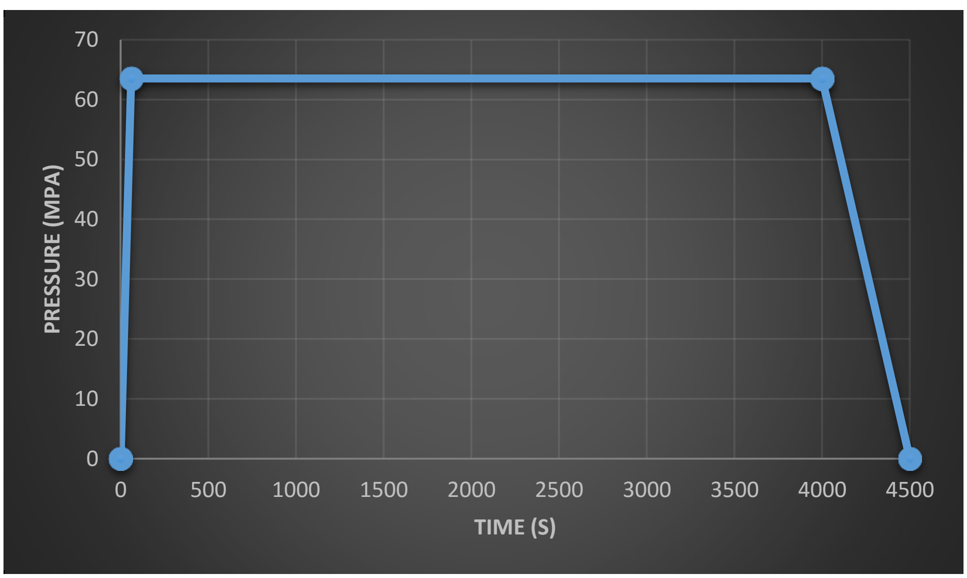

Figure 4.4. Pressure time history of the pressure applied on the couple

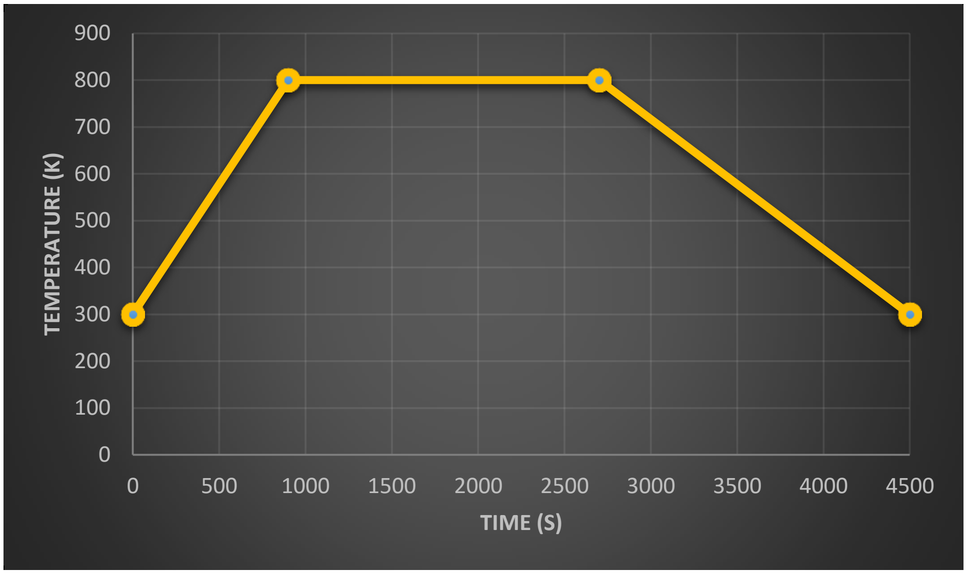

Figure 4.5. Temperature time history of the die and couple inside the hot press

In the hot pressing process, temperature gradient needed to be defined as well. Temperature was undertaken to reach 800 K from room temperature which is almost 300 K in 15 minutes and stayed constant for 30 minutes. Finally, die and couple linearly were cooled down back to the room temperature again in half an hour. It is important to know the temperature of the thermoelectric couple before putting the brass ring on was 200 K. The contraction of the couple and expansion of the brass ring help the pressing process of brass ring onto the couple easier.

The brass ring was pressed onto the TE couple to induce more compression stresses in the couple. The brass ring was heated up to 400 K while the couple was cooling down to 200 K. Interference fit of the Brass ring and the thermoelectric couple was chosen as 0.002 inches.

In the final step, the couple thermal-displacement analysis was used the same as pervious steps. At that stage, there was no structural load, but since the couple experienced a temperature gradient, thermal stresses were generated accordingly. The boundary conditions in this step were defined as below:

1) The coolant temperature of 400 K which was applied to the outer surface of the brass ring.
2) The hot air in the vehicle exhaust with temperature of 800 K was assigned to the inner surface of the couple which is the inner titanium ring.
3) All the residual stresses from pervious steps had direct effects on the final results. (Spring-back effects, residual stresses, temperature, and …)

Skutterudite is a brittle material and it behaves poorly when faces tensile stresses which cause radial and circumferential cracks. Cracks in the skutterudite materials may cause interruption or disconnection of the electrical circuit, produced by the thermoelectric couple. All the manufacturing process was done to put the thermoelectric couple, especially skutterudite part, in compression to avoid thermal cracks inside the device. Cracks increase the electrical resistance of the circuit by reducing the surface area of the connected materials.

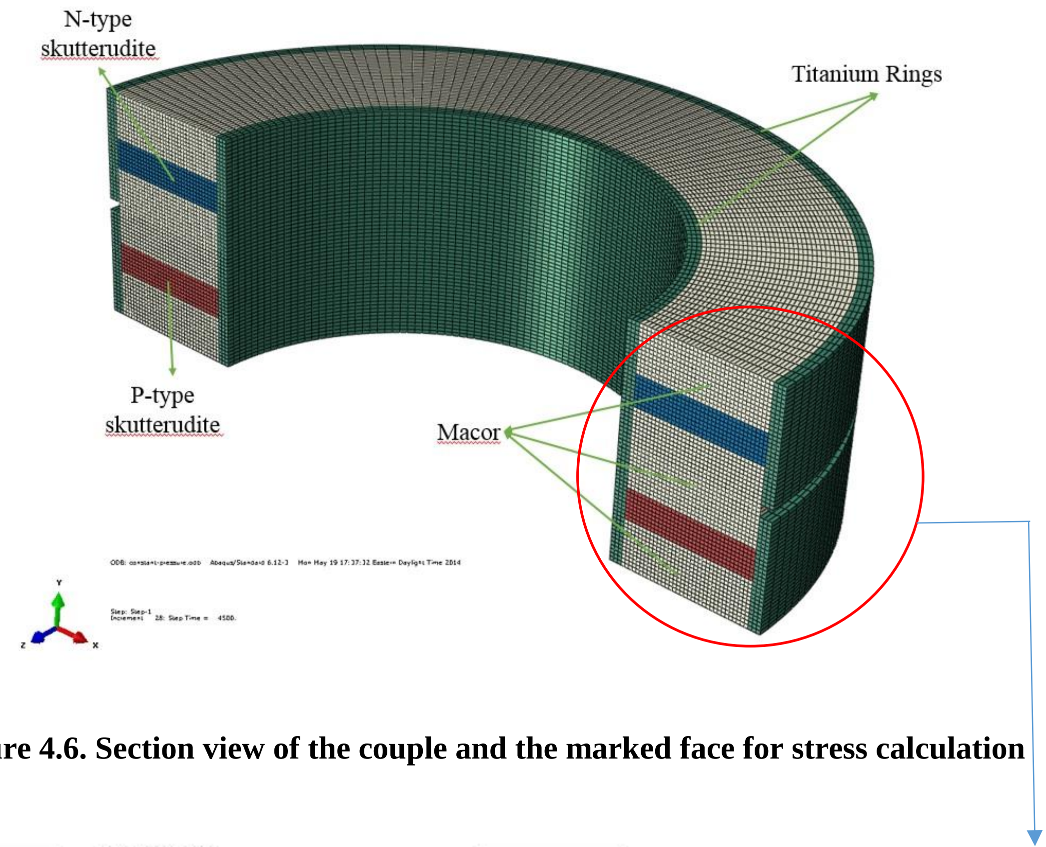

Figure 4.6. Section view of the couple and the marked face for stress calculation

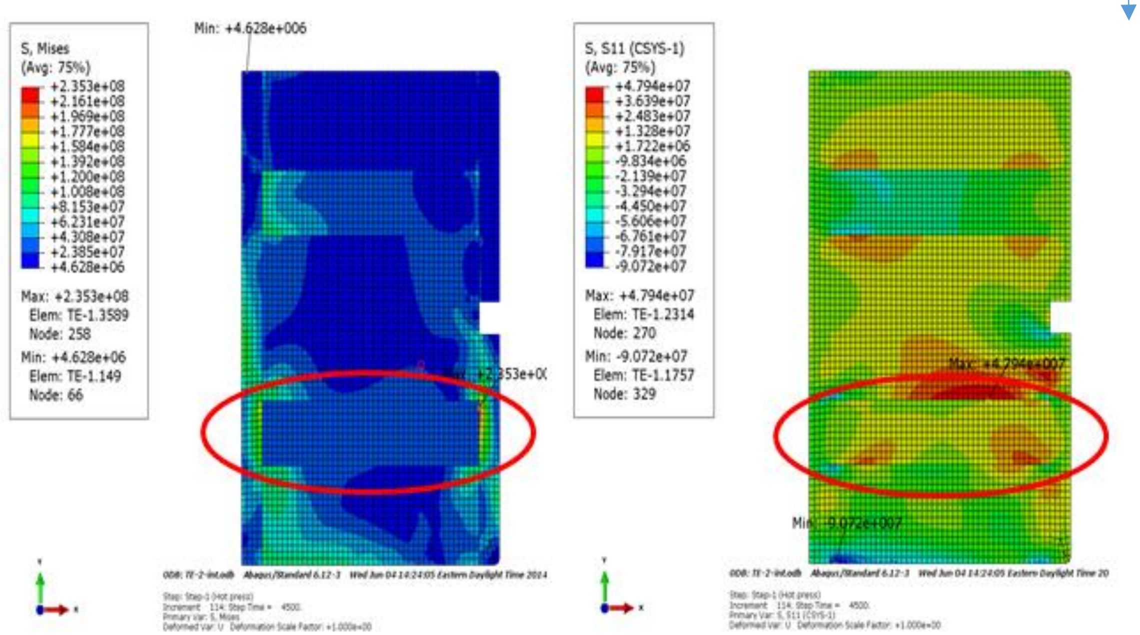

Figure 4.7. Stress distribution, S: Mises, S11: Radial

Figure 4.7 shows more than 80% of the P-type Skutterudite was experiencing severe tensile stress in radial and circumferential directions. These tensile stresses are the main source of the cracks in the skutterudite.

The finite element simulation results which are mentioned or will be mentioned express the qualitative agreement with the actual thermoelectric generator behavior. From **Figure 4.7**, it can be observed high tensile stresses are in the P-type skutterudite in the three manufacturing steps. During hot press, skutterudites wanted to expand however, they were fixed between two titanium rings and had bonding with them. This phenomenon forced the skutterudites to go to their plastic region and experience plasticity. When the cool down cycle started after hot pressing, those materials suffered a little plasticity followed by mostly unrecoverable expansions. Upon releasing of the forming forces, the material had a tendency to partially return back to its original shape because of the elastic recovery of the material. This is called Springback effect and influenced not only by tensile and yield strength, but also by thickness, bend radius and bend angle. Cooling cycle has caused high tensile stresses in the P-type skutterudite which became residual stresses in the following steps. These reasons show the cracks in the skutterudite which is shown in **Figure 4.8**.

Figure 4.8. P-type skutterudite radial and circumferential cracks

Existence of the cracks in the skutterudite after hot pressing step was a challenge for thermoelectric device to work properly. Different assumptions were made and simulated to deal with this issue. All of the following results are for the hot pressing step and they do not cover anything for other steps since tensile stresses in this step was more critical rather than other steps. The approaches and assumptions aiming to reduce tensile stresses are listed below:

1) Increasing the thickness of the outer titanium ring
2) Increasing the thickness of both outer an inner titanium rings
3) Using stiffer titanium ring having Young's modulus of 140 GPa

4) Increasing the applied pressure on thermoelectric couple in the hot press up to 100 MPa instead of 63.5 MPa which is used to be
5) Removing the applied pressure on titanium ring and put it on the Macor® only
6) Taking the pressure off from the thermoelectric couple after reaching the room temperature
7) Changing the location of the N and P-type. P-type goes on top and N-type goes down
8) Remove bonding between skutterudite and Macor® by assuming slip surface with no friction and bonding between them
9) Thermoelectric couple with thicker outer titanium ring accompanied by taking off the pressure after reaching the ambient temperature which is the combination of assumptions 1 and 6
10) Use more P-type skutterudite powder to make a thicker layer of P-type in the couple

4.1.1.1 Couple with Thicker Outer Titanium Ring (0.035”)

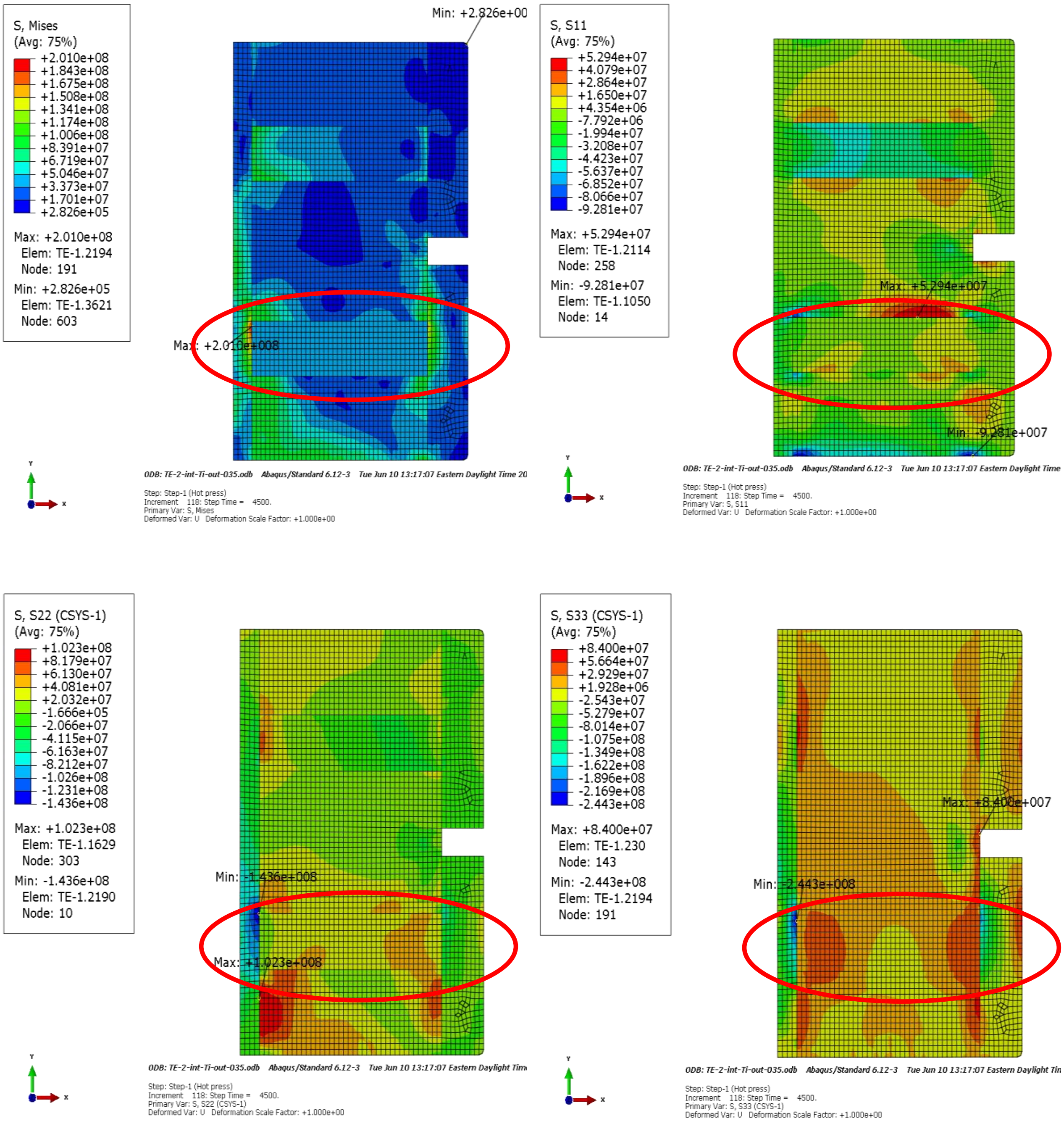

Figure 4.9. Stress distribution, S: Mises, S11: Radial, S22: Circumferential, S33: Axial

4.1.1.2 Couple with both Thicker Outer and Inner Titanium Rings (0.035”)

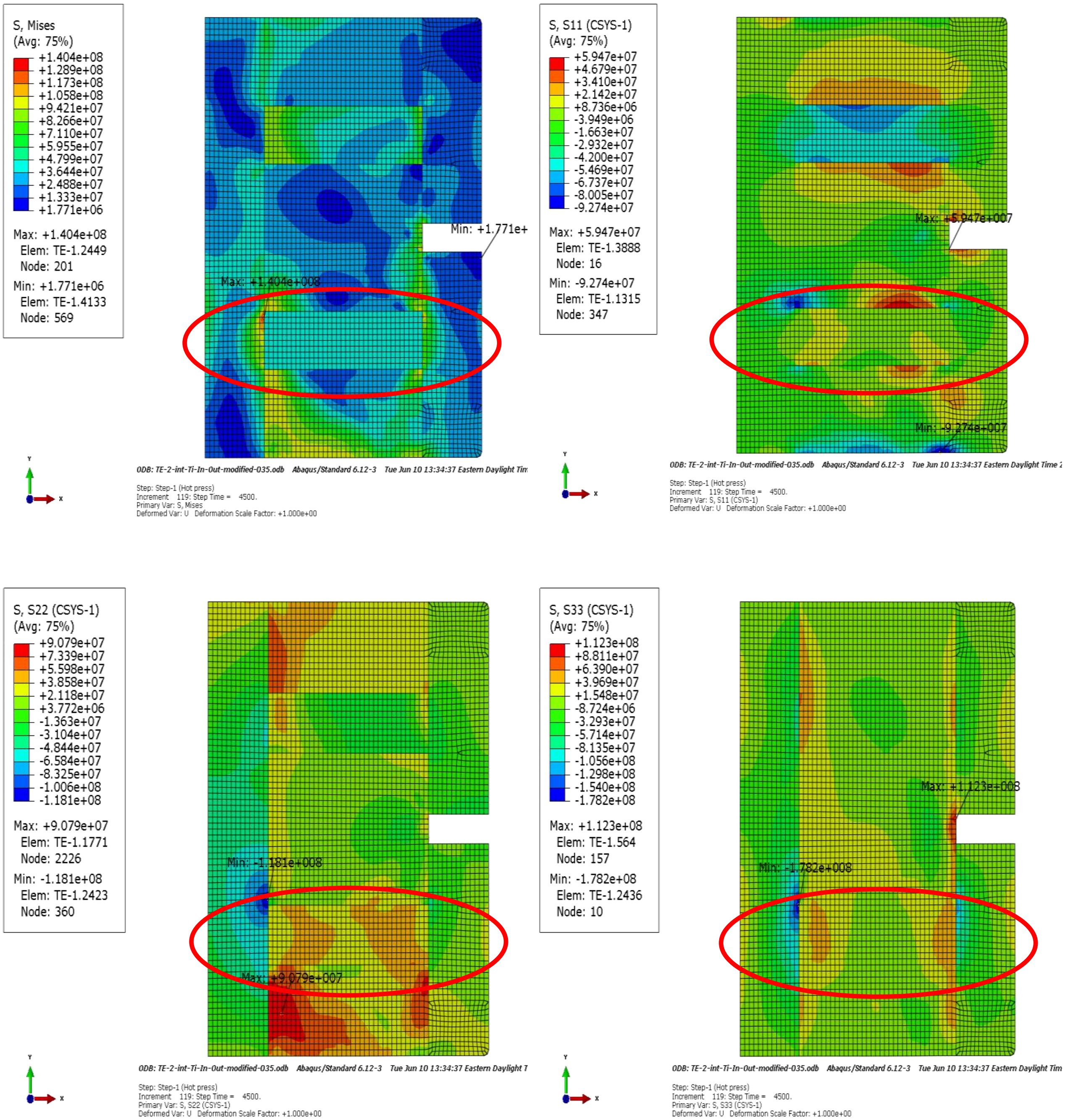

Figure 4.10. Stress distribution, S: Mises, S11: Radial, S22: Circumferential, S33: Axial

4.1.1.3 Thermoelectric Couple Made by Stiffer Titanium Rings (E=140 GPa)

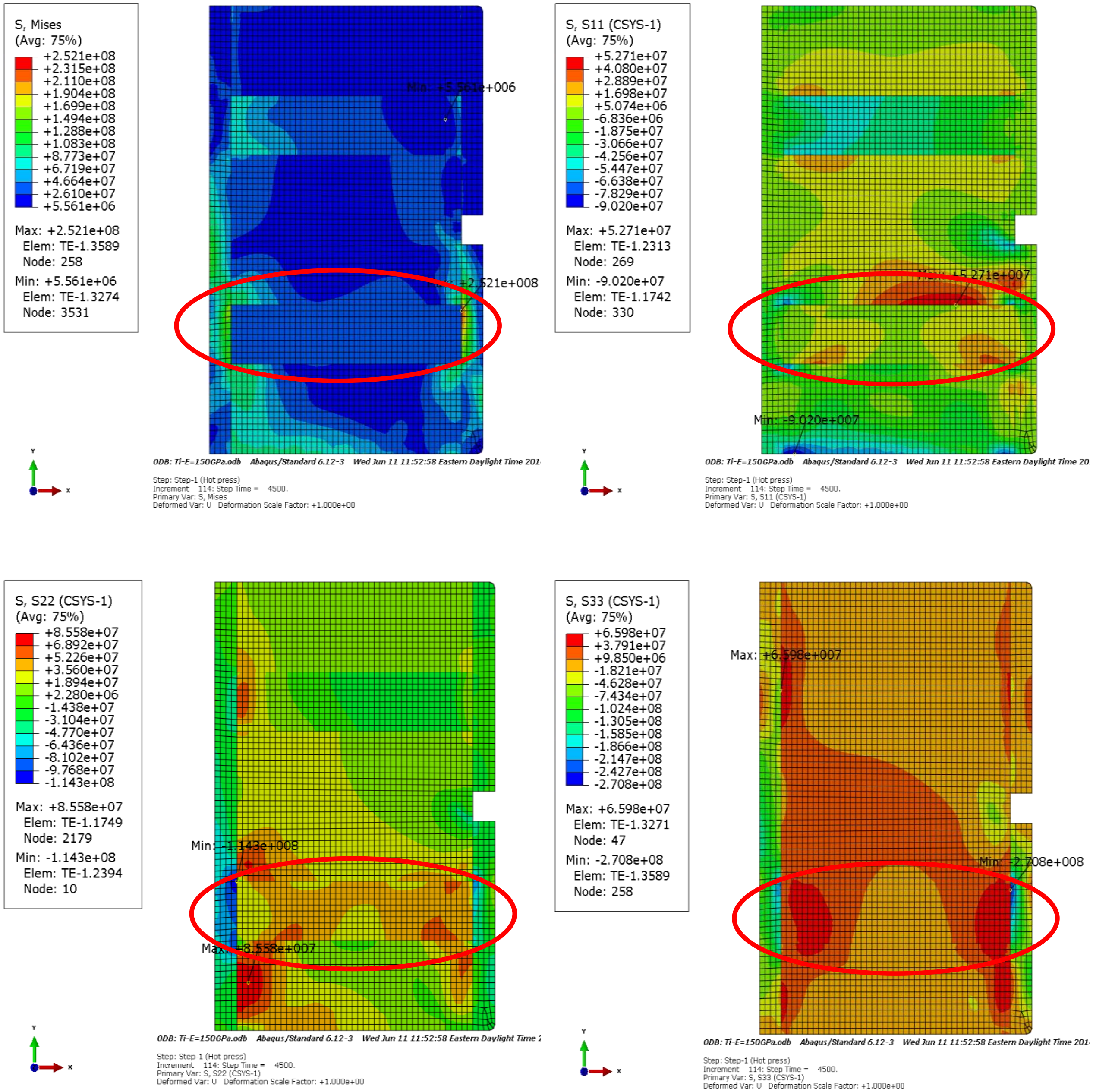

Figure 4.11. Stress distribution, S: Mises, S11: Radial, S22: Circumferential, S33: Axial

4.1.1.4 More Applied Pressure on the Thermoelectric Couple (100 MPa)

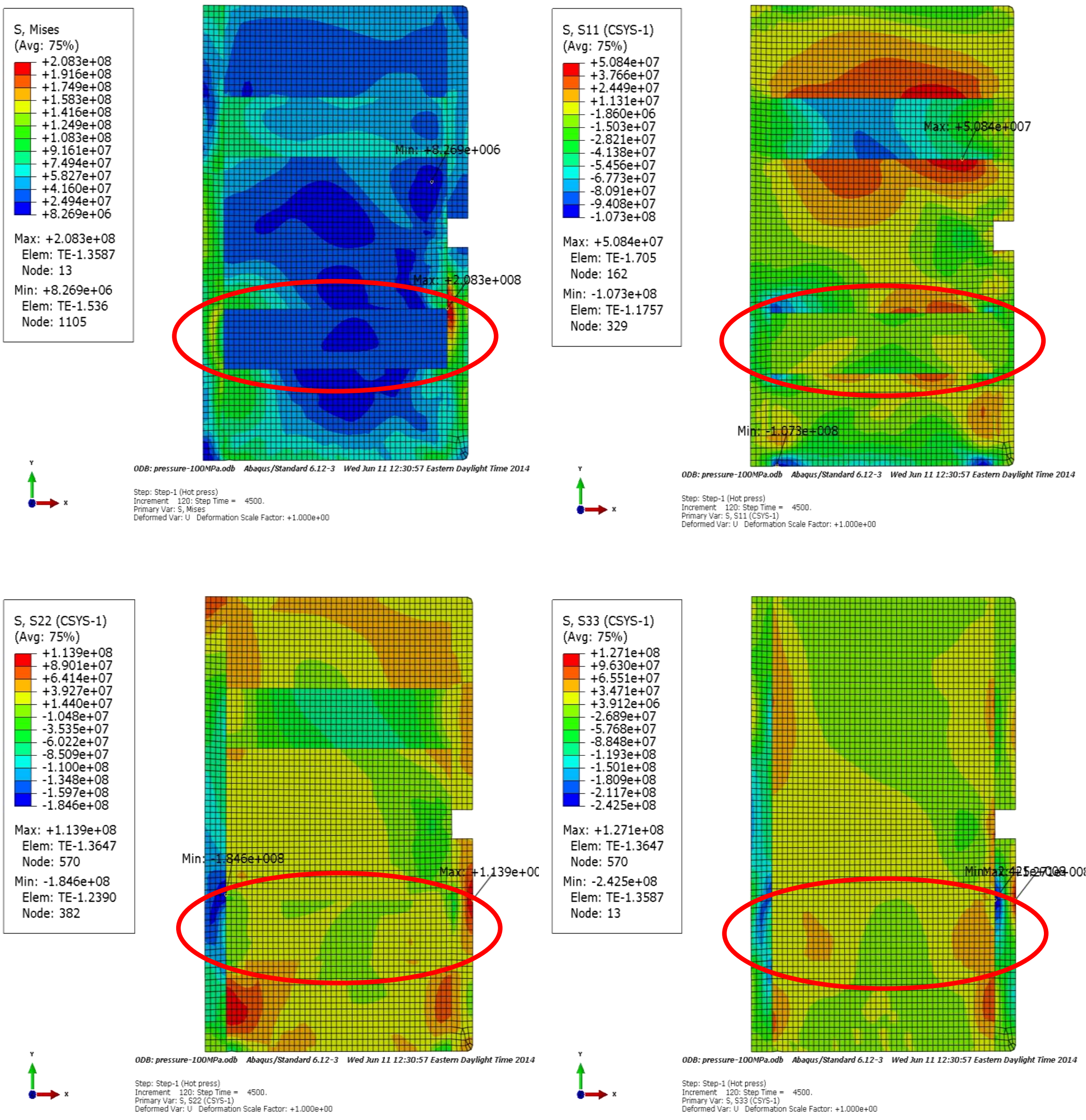

Figure 4.12. Stress distribution, S: Mises, S11: Radial, S22: Circumferential, S33: Axial

4.1.1.5 Removing Applied Pressure on Titanium Rings

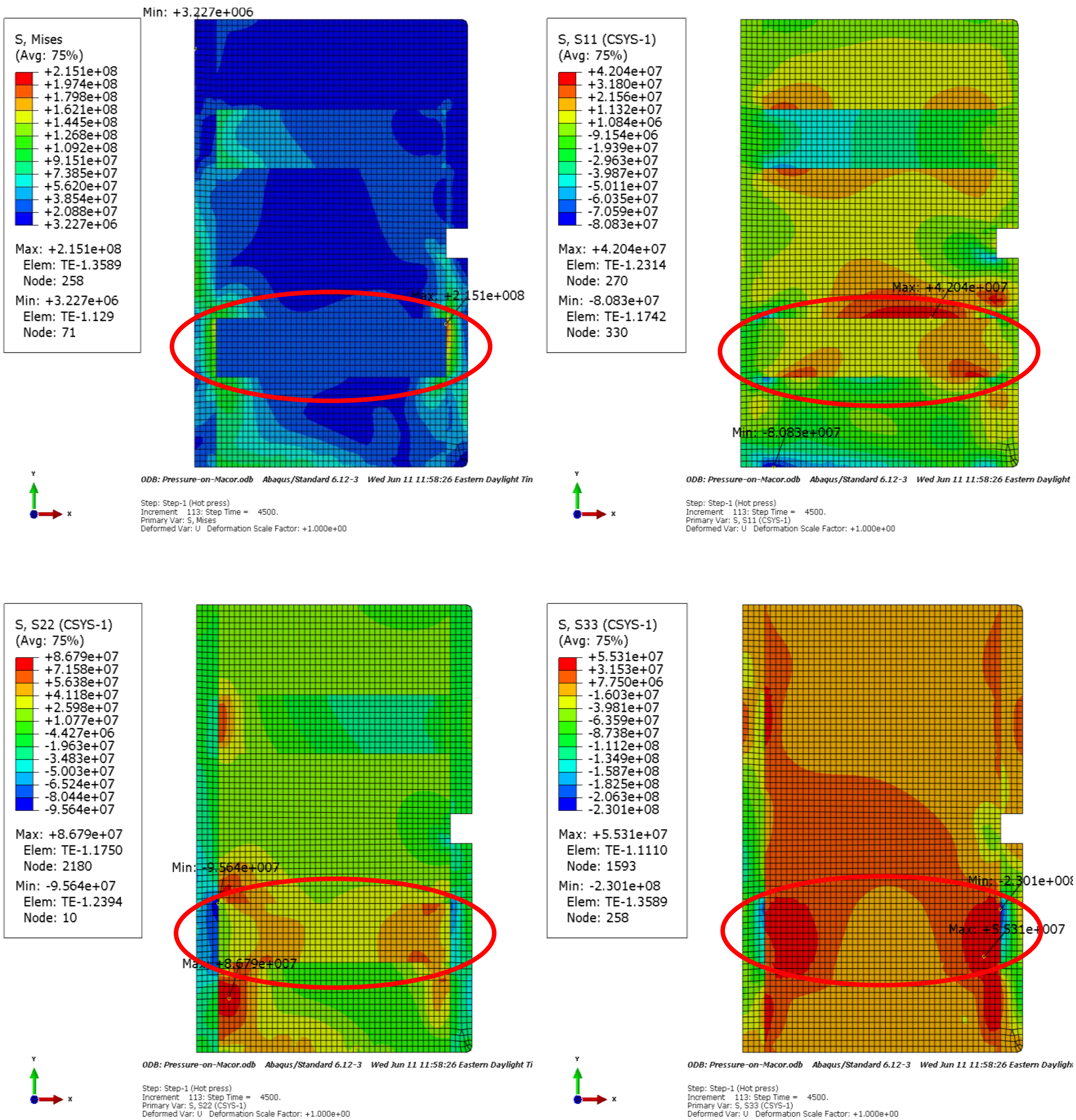

Figure 4.13. Stress distribution, S: Mises, S11: Radial, S22: Circumferential, S33: Axial

4.1.1.6 Pressure off after the Couple Reached the Room Temperature

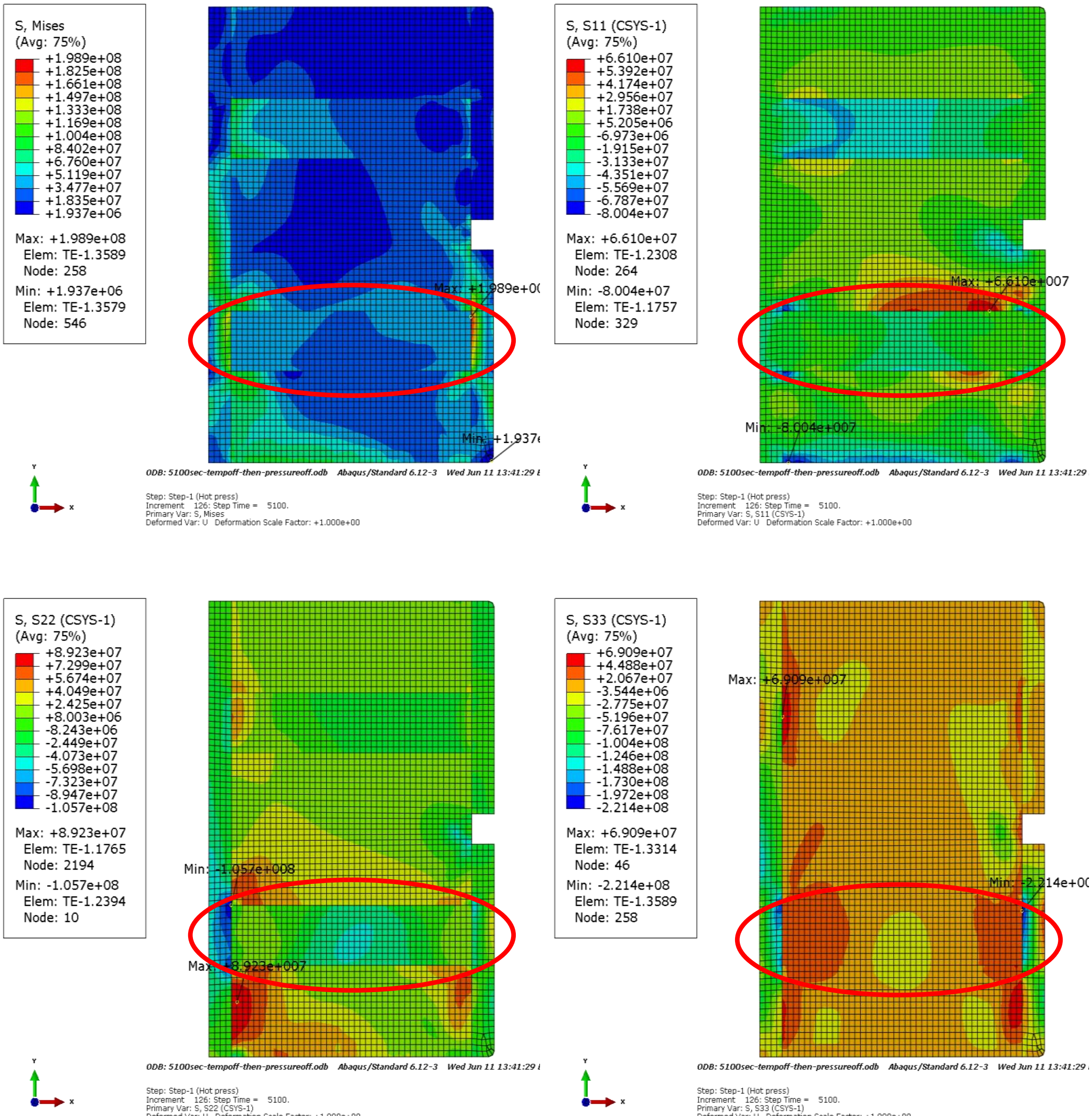

Figure 4.14. Stress distribution, S: Mises, S11: Radial, S22: Circumferential, S33: Axial

4.1.1.7 Relocating the P-type and N-type

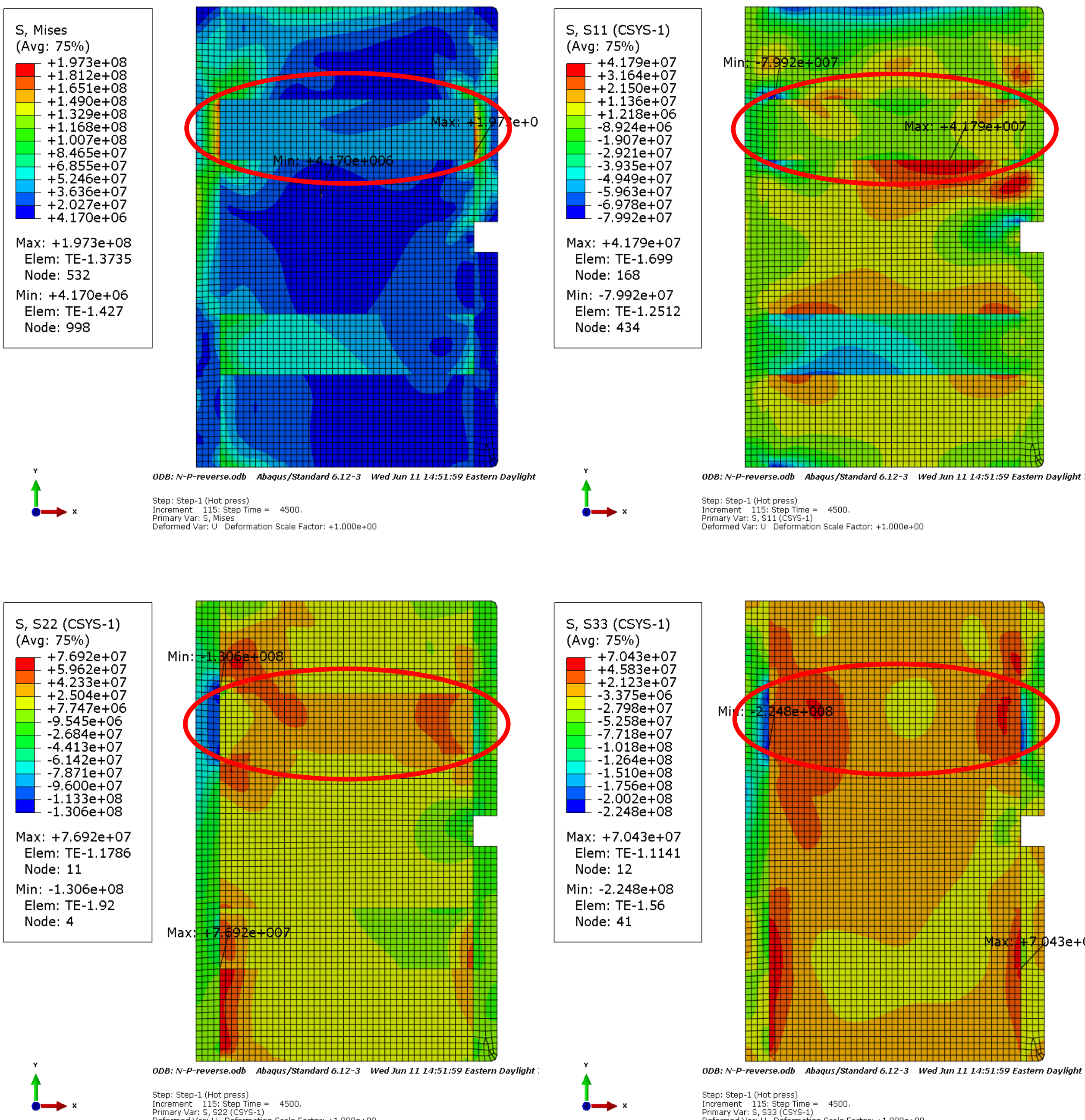

Figure 4.15. Stress distribution, S: Mises, S11: Radial, S22: Circumferential, S33: Axial

4.1.1.8 Thermoelectric Couple with No Bonding between Skutterudite and Macor®

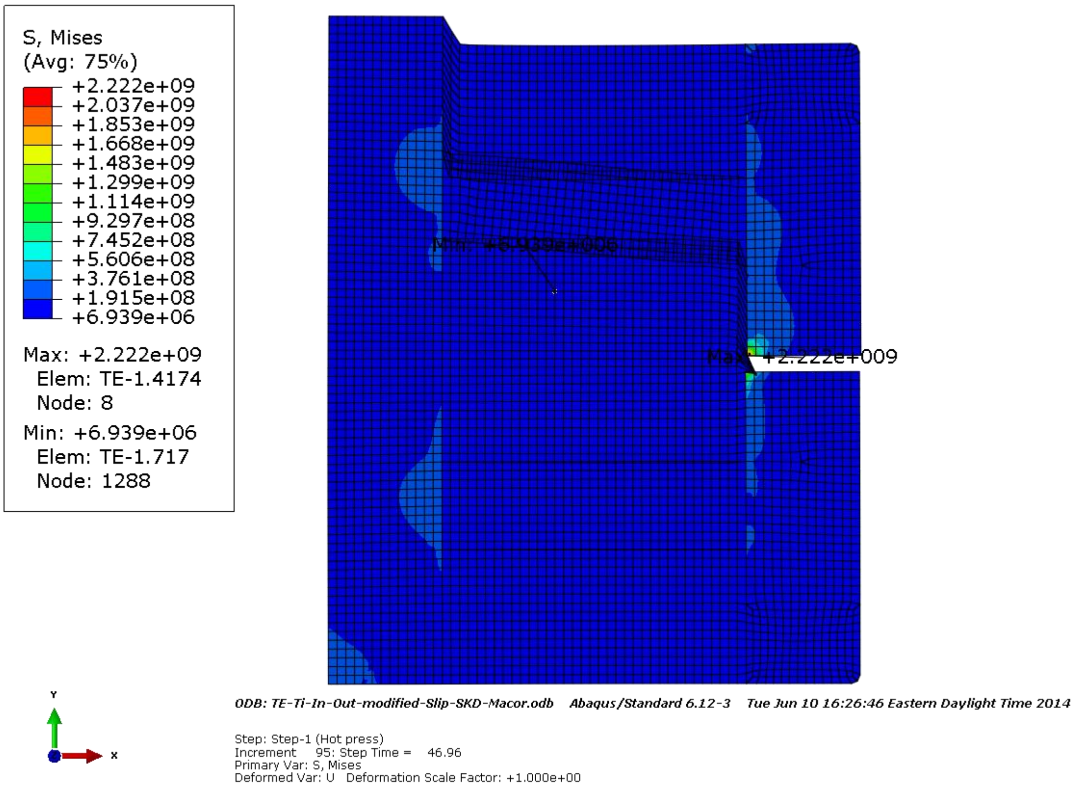

Figure 4.16. Mises stress distribution

4.1.1.9 Couple with Thicker Outer Titanium Ring (0.035”) Followed by Taking off the Pressure after Cooling Down

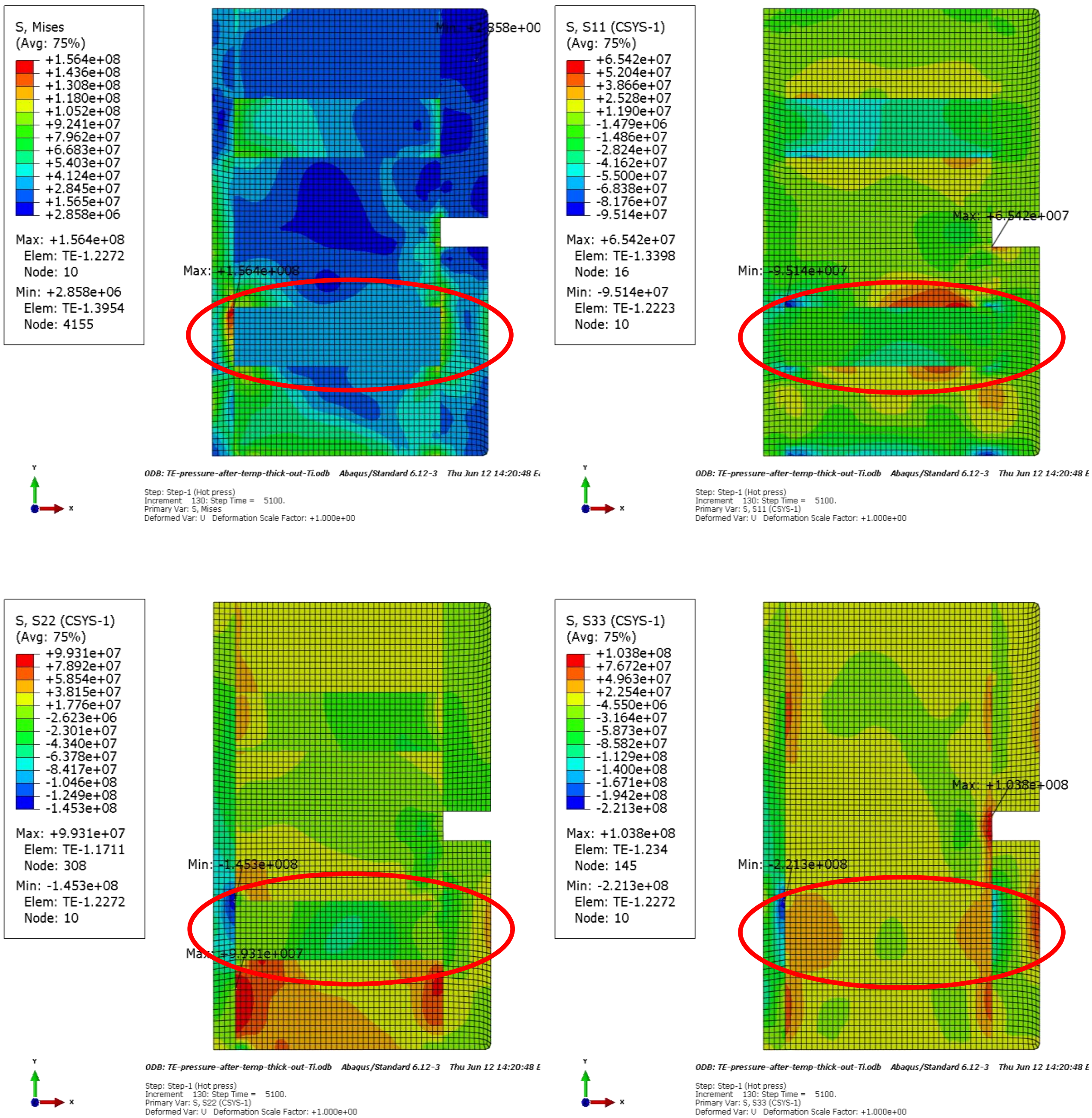

Figure 4.17. Stress distribution, S: Mises, S11: Radial, S22: Circumferential, S33: Axial

4.1.1.10 Couple with Thicker P-type Skutterudite (1.36 mm)

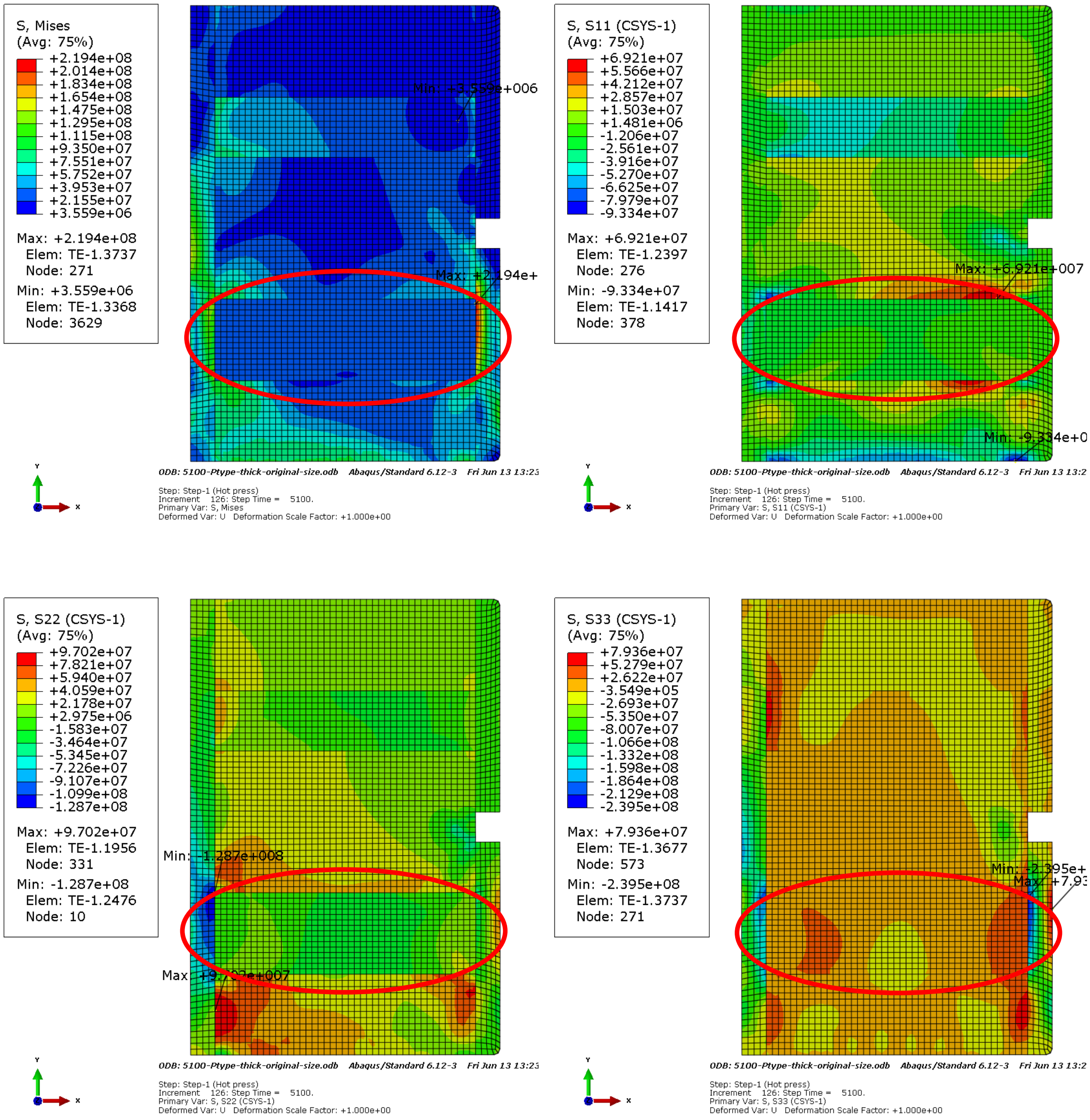

Figure 4.18. Stress distribution, S: Mises, S11: Radial, S22: Circumferential, S33: Axial

4.1.1.11 Thermoelectric Couple having thicker P-type Skutterudite (1.36 mm) and Thicker Outer Titanium Ring (0.035”)

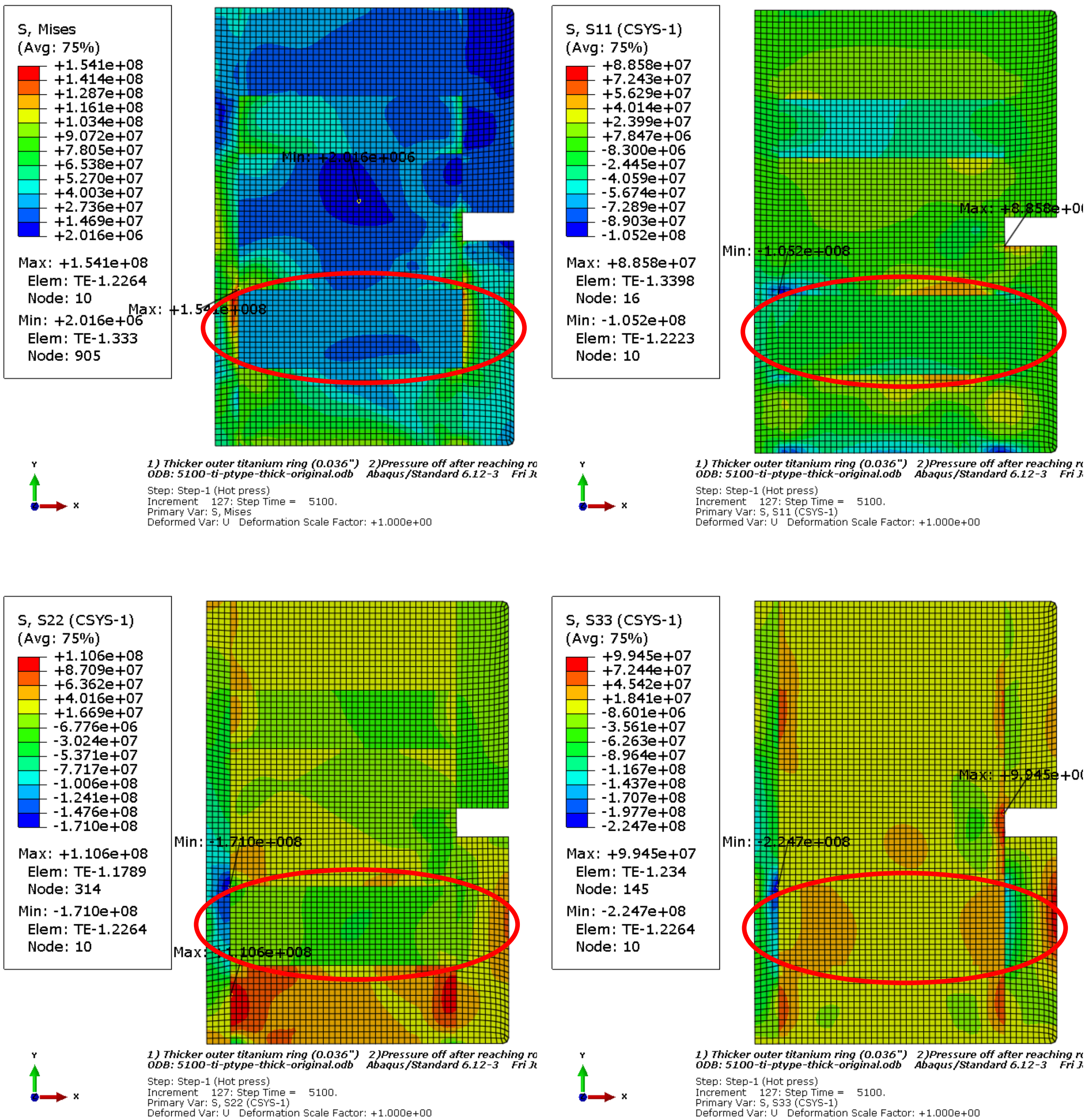

Figure 4.19. Stress distribution, S: Mises, S11: Radial, S22: Circumferential, S33: Axial

4.1.2 Finite Element Analysis Results of the First Generation Thermoelectric Couple

Figure 4.9 shows the results of the first step toward improving the critical tensile stresses by reducing those stresses. The approach was thickening the outer titanium ring to see the effect of this change to our model. The initial thickness of the titanium ring was 0.016'' and afterward it was chosen as 0.035". The tensile stresses in P-type Skutterudite were reduced but 50% of the Skutterudite was in tension which could not completely solve that issue.

Figure 4.10 illustrates the state of stresses after increasing the thickness of both titanium rings to 0.035". The tensile stresses were lower than the original design; however they were more than the initial design which was explained in section 4.1.1.1.

From **Figure 4.11,** which is the case of using stiffer titanium ring with modulus of elasticity of 140 GPa, it can be seen that the tensile stresses reduced compare to the initial design. The problem of this approach was existence of some regions in which Skutterudite experienced tensile stresses.

The next step toward enhancement of the module was increasing the pressure in hot pressing step up to 100 MPa. The finite element solution can be found in **Figure 4.12**. The simulations showed by increasing the pressure, there was a considerable change in the state of stresses which indicated more than 75% of the P-type was under compression loads however, existence of tensile stresses in the intersection of skutterudite and titanium ring is an issue which might cause cracks in that area.

In **Figure 4.13,** results of the simulation based on the applied load on Macor® only and not titanium rings. The results were similar to the initial model because the way that TE was modeled was perfect bonding between skutterudites, Macor®, and titanium rings. The results of simulation did not have a huge difference. The cohesive zone between skutterudites and titanium rings must be known to model the module realistically. For modeling purposes, defining different cohesive zones leads to fully slipping the material on each other or behaving as a unique solid part.

Induced tensile stresses inside the skutterudites are due to applied load in the manufacturing process of thermoelectrics. Different behavior of materials in the thermoelectric couple under heat loads is one of the main reasons of having tensile stresses in the skutterudite. It might be a way to eliminate all the tensile stresses which puts the whole couple under compressive stresses. The initial model was based on applying pressure and temperature simultaneously. From the beginning of the hot pressing the temperature raised to 800 K then cooled down to 300 K while the pressure was kept at 63.5 MPa until the module reached the room temperature, then gradually it was reduced. **Figure 4.14** shows some improvement in terms of avoiding tensile stresses radially and circumferentially in P-type Skutterudite but not completely able to remove all tensile stresses.

Figure 4.15 and **Figure 4.16** demonstrate the effects of lateral pressure on inner titanium ring, changing the location of N-type and P-type together, and skipping the interactions between Skutterudites, Macor®, and titanium rings regardless of bonding between them. All these considerations were not a helpful approach to solve the skutterudite cracking issue.

Figure 4.17 shows the stress distribution for the module having thicker outer titanium ring. Tensile stresses were not considerably high and the P-type Skutterudite was mostly under compression. The difference between this model and the second approach is the hot pressing process. In this model, the pressure applied was taken off from the module after it reached the room temperature.

Figure 4.18 shows the differences between Mises, radial, circumferential, and axial stresses within the TE couple with thicker P-type Skutterudite with the same length. Radial stresses in P-type ranged between -12 MPa to 29 MPa. Circumferential stresses change from -35 MPa to 41 MPa in some regions. Axial stresses were higher than other stresses which covered the range of -27 MPa to 53 MPa.

According to the **Figure 4.19**, thermoelectric couple which thicker P-type Skutterudite and outer titanium ring, the radial stresses in P-type were mostly tensile. The range of radial stresses was between -57 MPa to -8 MPa. P-type experienced a little bit of tension in terms of circumferential stresses, which were between -54 MPa to 40 MPa, in the corner of the P-type, Macor® and titanium ring. **Figure 4.20** shows the existence of the cracks after all of the mentioned consideration.

Figure 4.20. Thermal cracks in the P-leg

4.1.3 Finite Element Analysis of the Second Generation Couple Design

Finite element analysis of the thermoelectric device was performed by Abaqus 6.12-3 to calculate the temperature distribution and state of stresses within the second generation thermoelectric couple and investigate the materials and parts interactions that occur during performance tests and operating conditions.

The components of the couple used in the finite element modeling are shown in **Figure 4.21.**

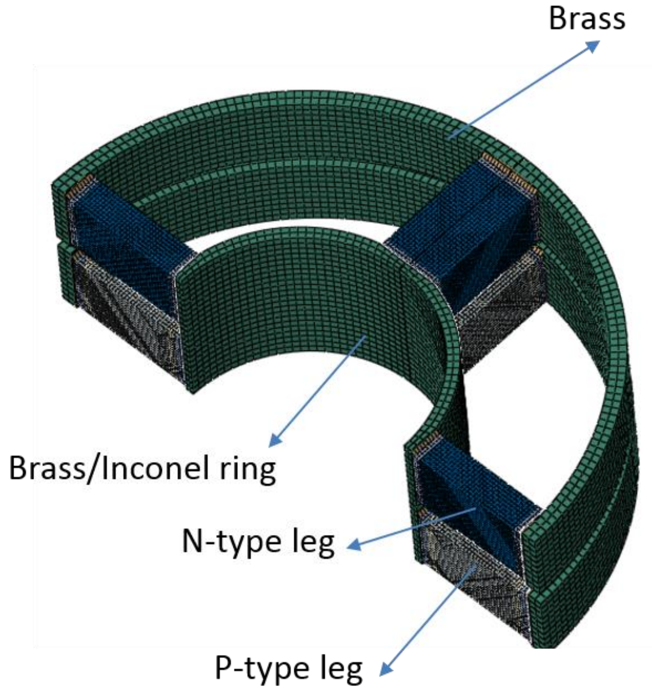

Figure 4.21. Section view of the meshed second generation couple

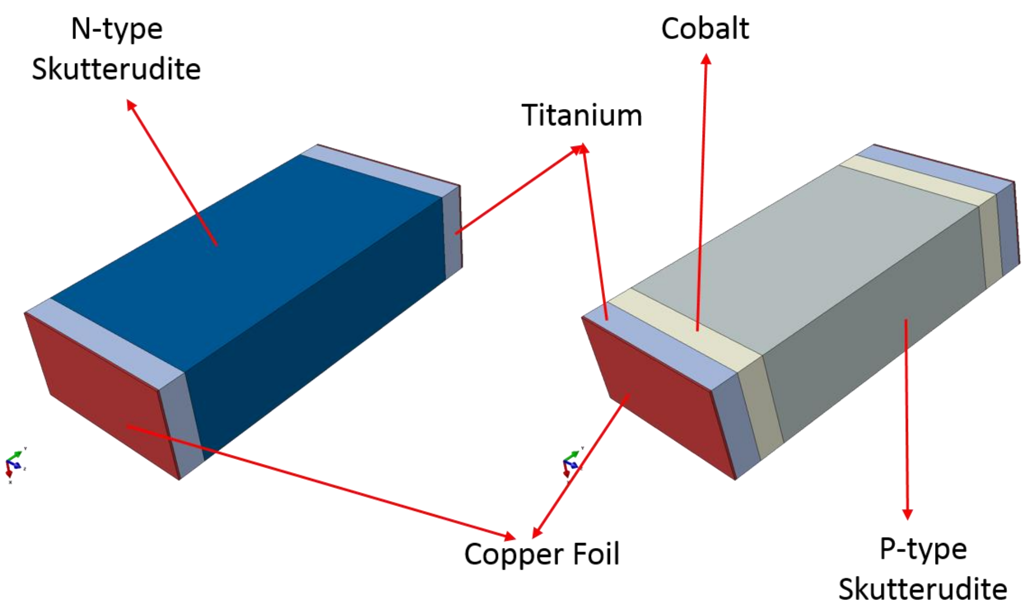

Figure 4.22. Components of N and P-type skutterudites

The model consists of inner brass/Inconel ring and outer brass rings with N and P-type skutterudite legs. The Inconel and brass ring have 0.03” thickness. The P-type skutterudite leg has a dimension of 0.21×0.14×0.14 inches while the N-type is 0.25×0.14×0.14. The thicknesses of cobalt layer, titanium layer, and copper foil are 0.02, 0.02, and 0.0015 inches respectively.

The purpose of using a layer of cobalt on P-type skutterudite is to grow a layer of $CoSb_3$ nanoparticles on the surface of skutterudite bulk matrix grain. This process showed to be a viable method which can be used in conjunction with other techniques such as doping and filling the voids to improve the ZT [66].

The couple was modeled as a 3-D deformable solid including different part as it is shown in **Figure 4.21** and **Figure 4.22**. The material properties including mechanical and thermal properties are summarized in the **Table 4.2**. Stress-strain data of the skutterudite and the steel are not included in the table below but all the essential information were considered to get a reliable simulation. In the finite element simulation, mechanical and thermal properties of the steel change when the temperature changes.

Table 4.2. Material properties of the thermoelectric couple components

	E(MPa)	υ	Density ρ (kg/m^3)	Thermal Expansion α (1/C)	Thermal Conductivity κ (W/m-C)	Specific Heat C_p (J/kg-K)
N-SKU	1.27e+5 (500˚C) 1.41e+5 (-60˚C)	0.231	7570	1.20e-5 (500˚C) 8.50e-6 (-60˚C)	4.5	140
P-SKU	1.13e+5 (500˚C) 1.31e+5 (-60˚C)	0.242	7570	1.50e-5 (500˚C) 1.28e-5 (-60˚C)	2.7	140
Titanium	1.20e+5	0.34	4500	8.90e-6	17	528
Copper	1.14e+5	0.31	8920	1.17e-5	387	385
Mica	1.72e+3	0.40	2900	3.00e-5	0.54	500
Brass	1.03e+5	0.28	8440	2.12e-5	116	377
Cobalt	2.11e+5	0.31	8900	1.2e-5	69	410
Inconel 600	2.06e+5	0.29	8470	1.33e-5	14.9	444
Solder	5.20e+4	0.35	7370	2.18e-5	61.1	220
Graphite	1.03e+5	0.30	1780	5.60e-6	70	760
Steel	2e+5 (25˚C) 1e+5 (100˚C)	0.3	7870	1.15e-5 (25˚C) 1.47e-5(1000˚C)	52	472

In the analysis part, transient module instead of steady-state was done. Boundary conditions were defined in the way to mimic the real physics of the problem. Fully couple thermos-mechanical equations were used as the governing equations of the problem. In the mesh menu, all the meshes were defined as quadratic 8-node thermally coupled brick, trilinear displacement and temperature (C3D8T) free mesh after choosing the base size as 0.0004 m.

4.1.3.1 Thermoelectric Couple Made by 2 Brass Rings

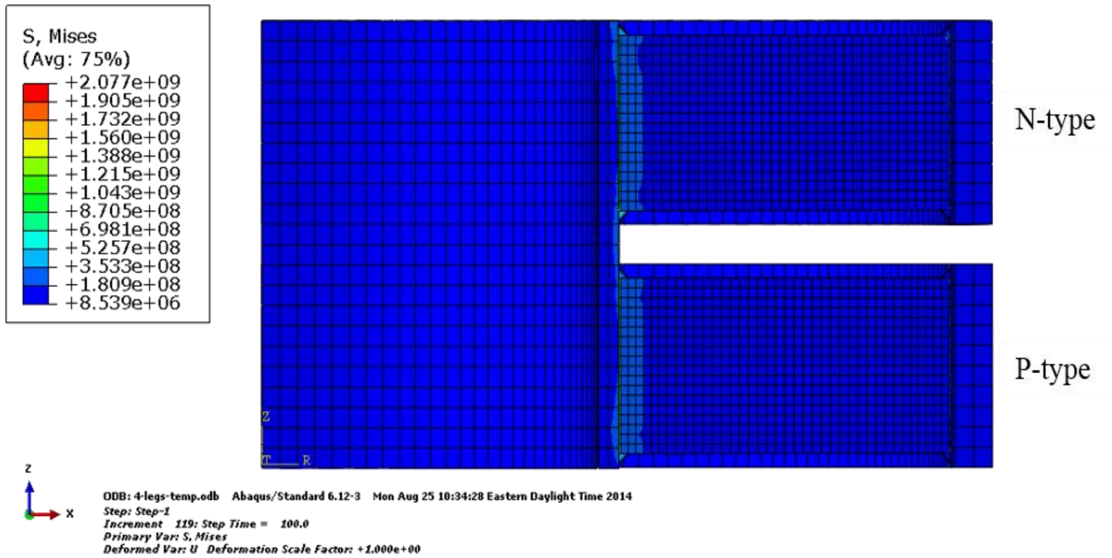

Figure 4.23. Mises stresses in N and P-type skutterudite

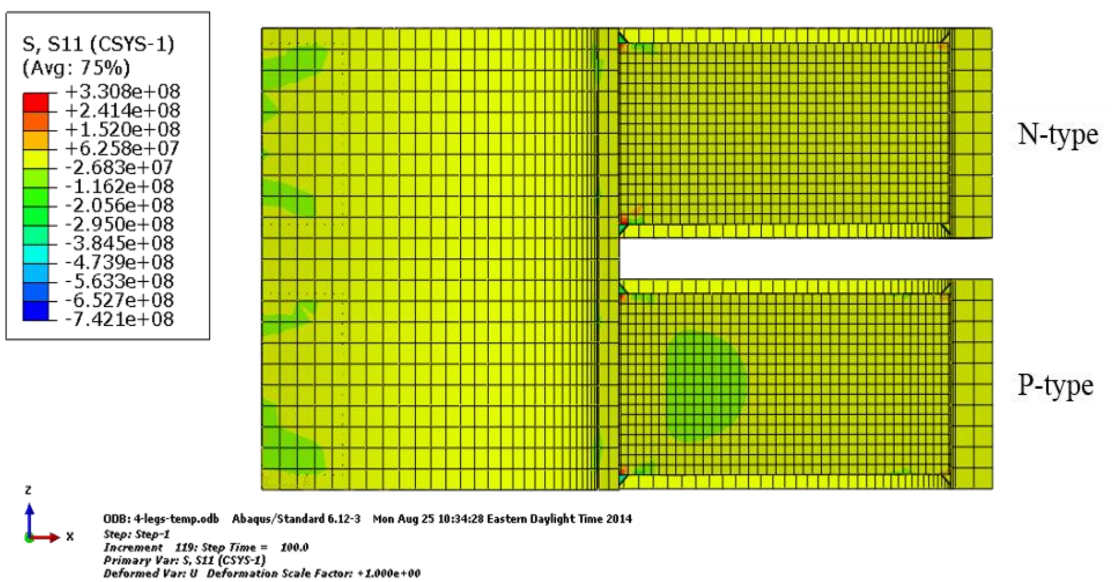

Figure 4.24. Radial stresses in N and P-type skutterudite

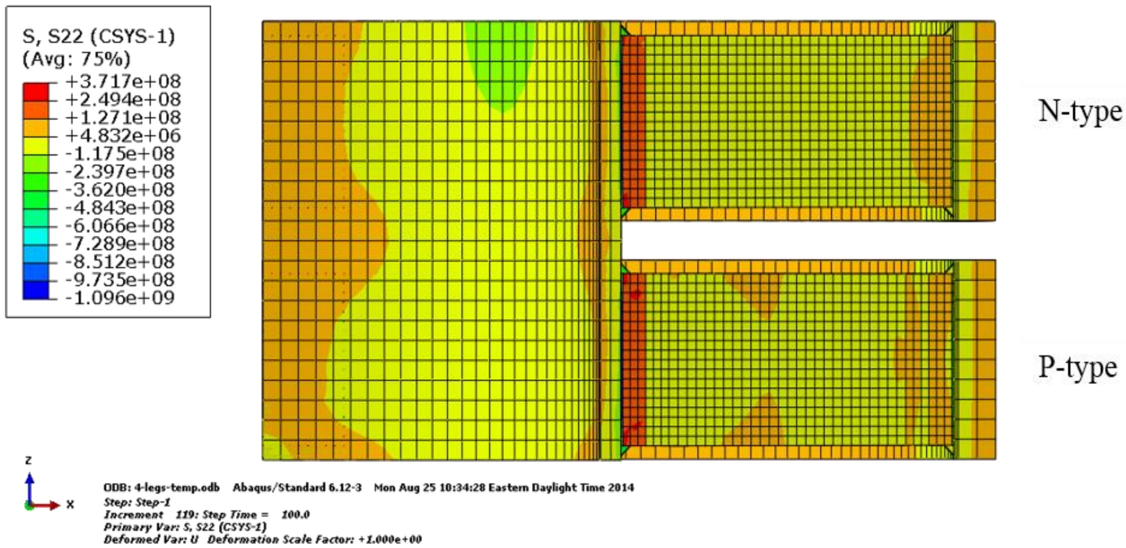

Figure 4.25. Circumferential stresses in N and P-type skutterudite

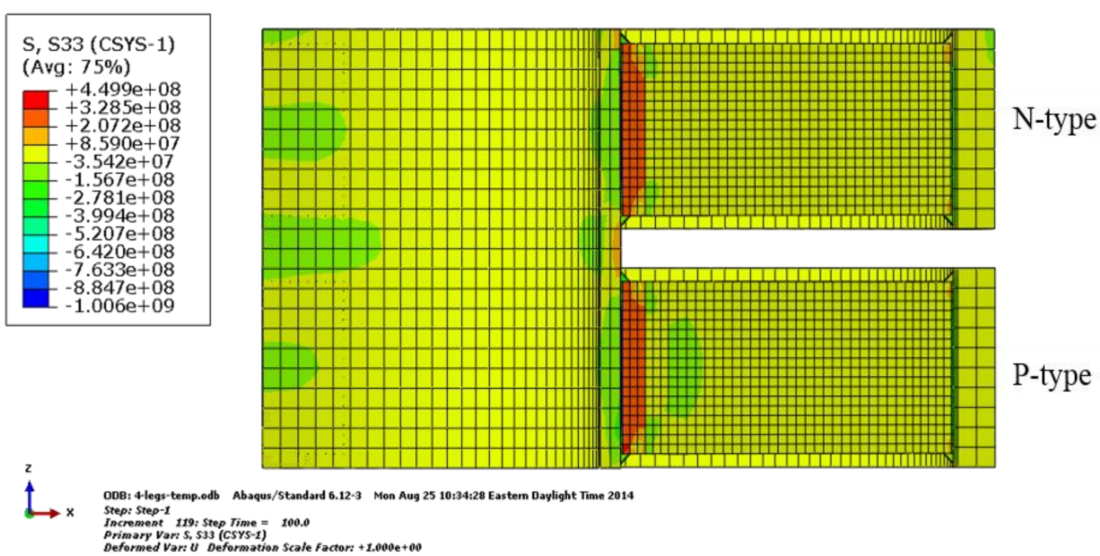

Figure 4.26. Axial stresses in N and P-type skutterudite

4.1.3.2 Thermoelectric Couple Made by 2 Brass Rings Assisted by a Steel Ring

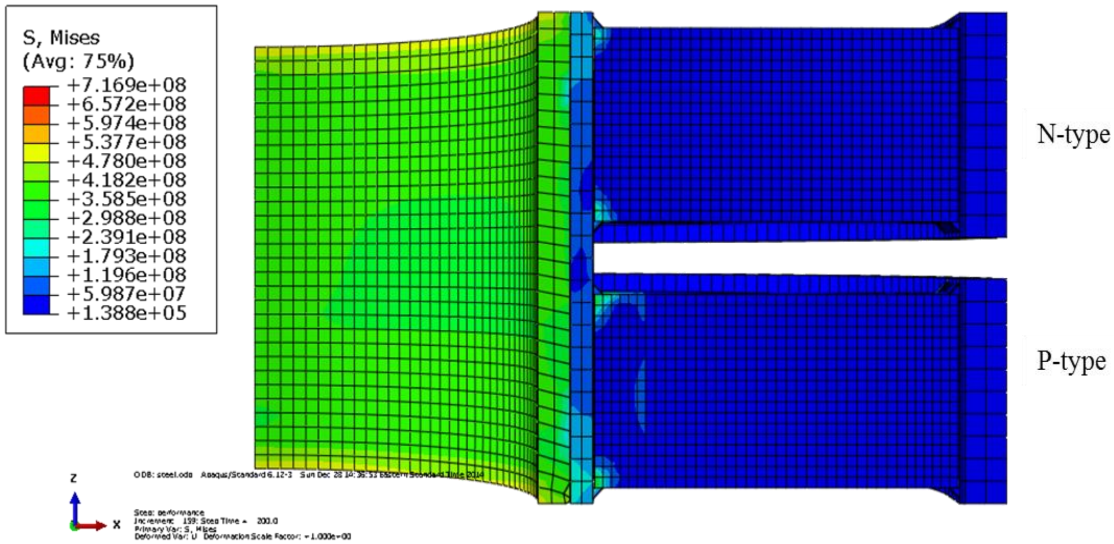

Figure 4.27. Mises stresses in the steel ring inserted couple

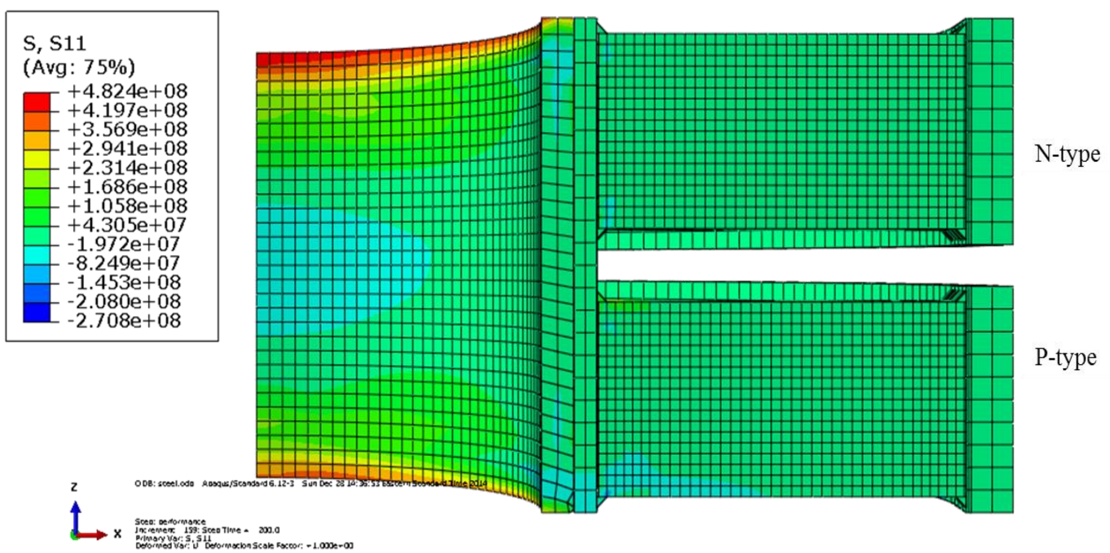

Figure 4.28. Radial stresses in the steel ring inserted couple

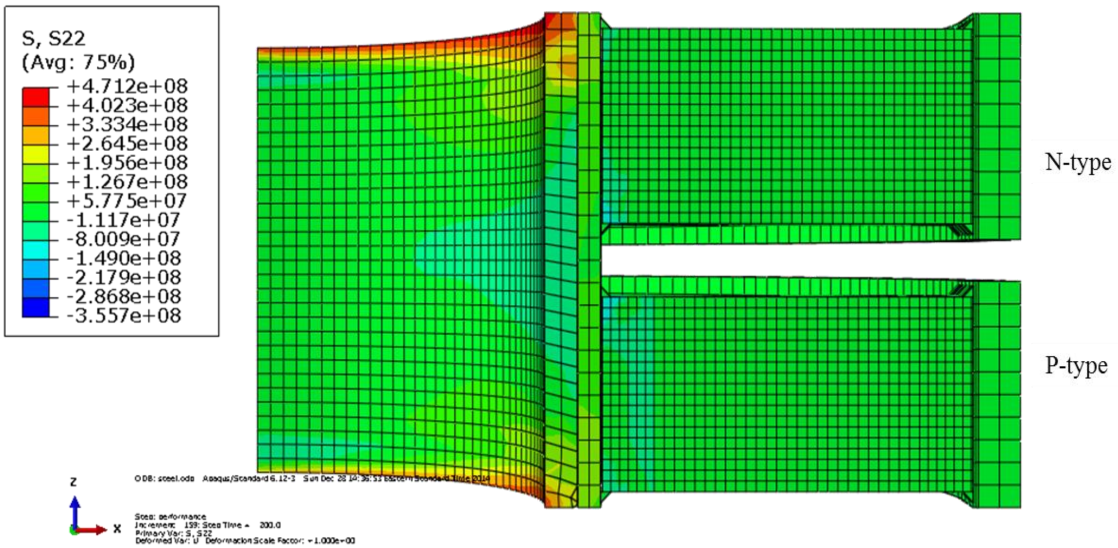

Figure 4.29. Circumferential stresses in the steel ring inserted couple

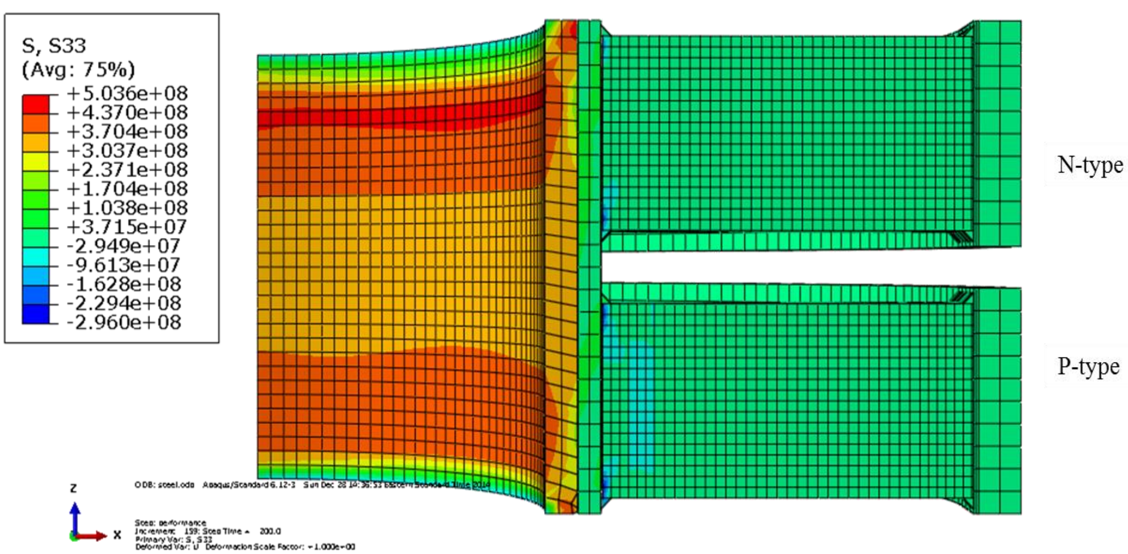

Figure 4.30. Axial stresses in the steel ring inserted couple

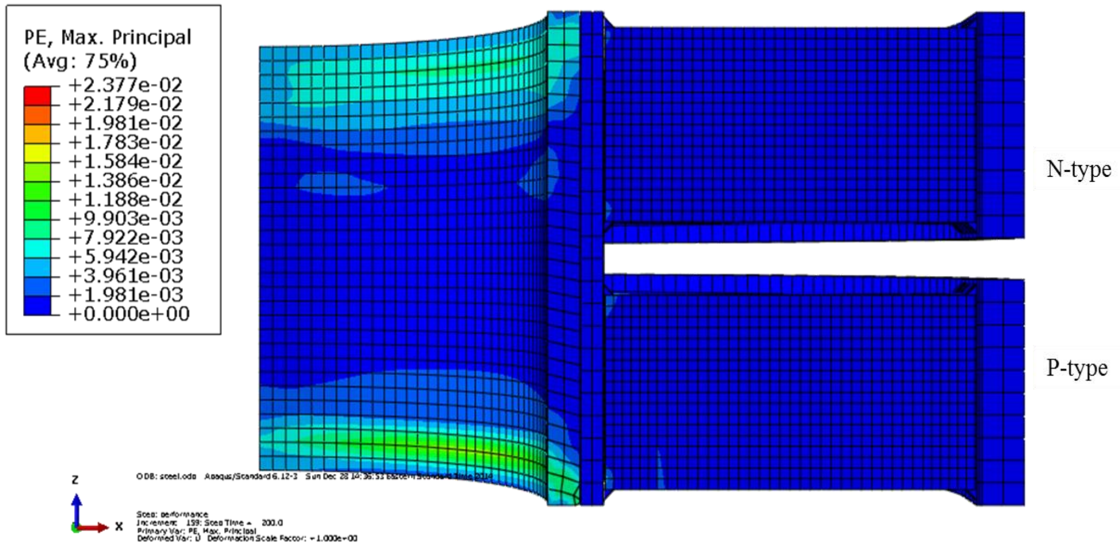

Figure 4.31. Maximum principal plastic strains in the steel ring inserted couple

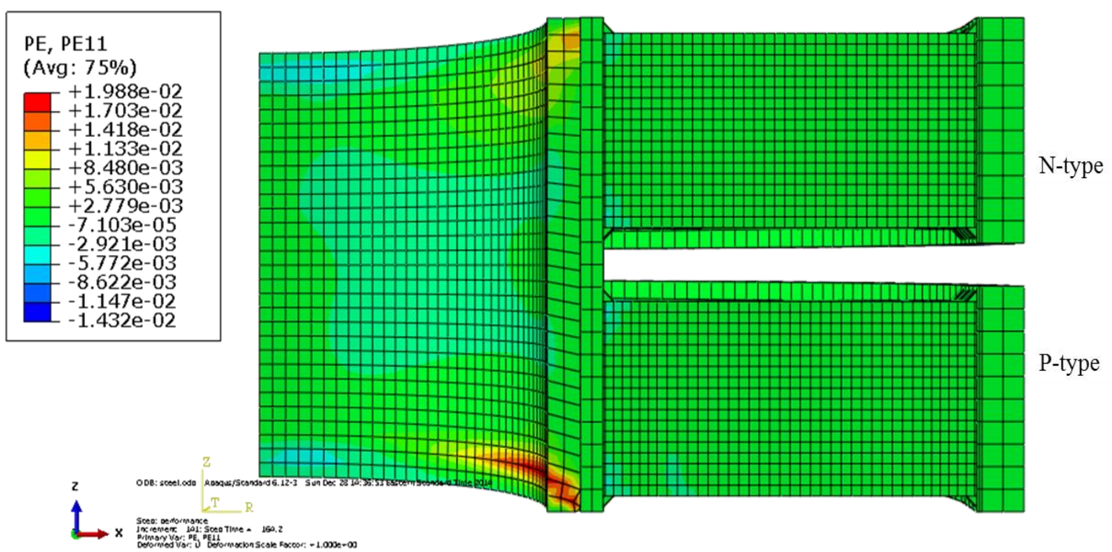

Figure 4.32. Plastic strains in x direction in the steel ring inserted couple

4.1.3.3 Thermoelectric Couple Made by 2 Brass Rings Assisted by a Graphite Ring

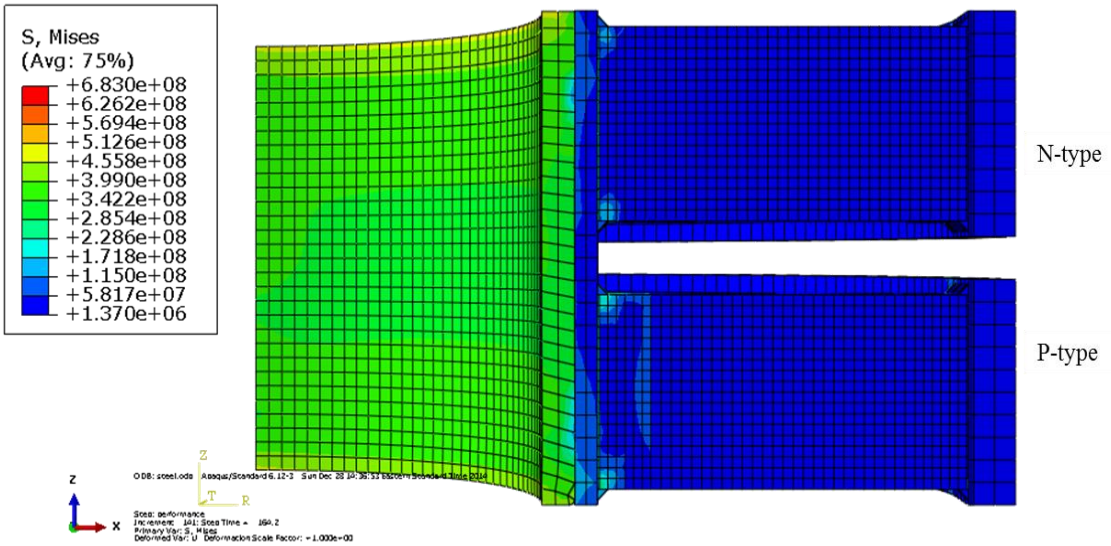

Figure 4.33. Mises stresses in the graphite ring inserted couple

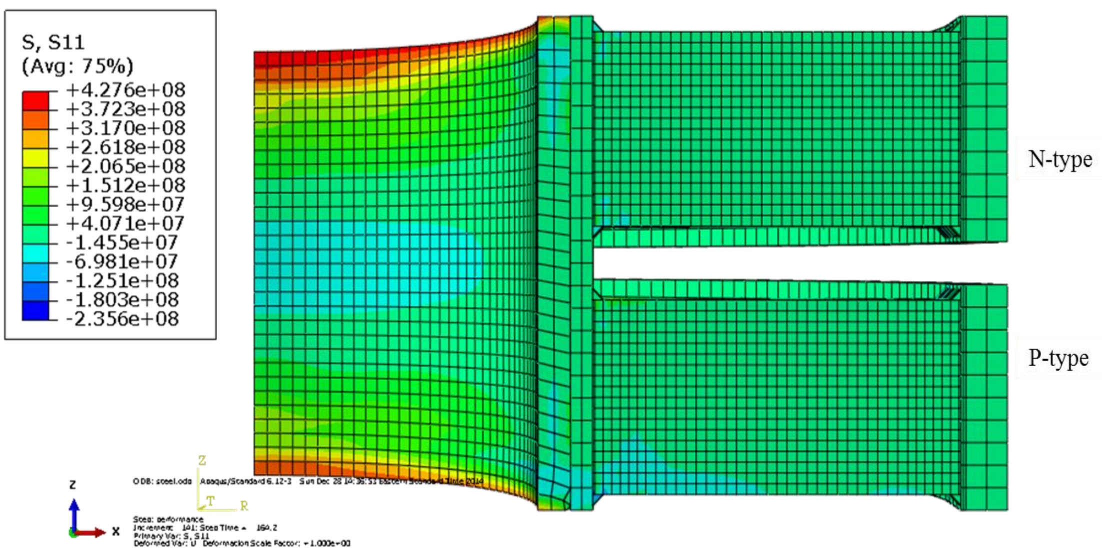

Figure 4.34. Radial stresses in the graphite ring inserted couple

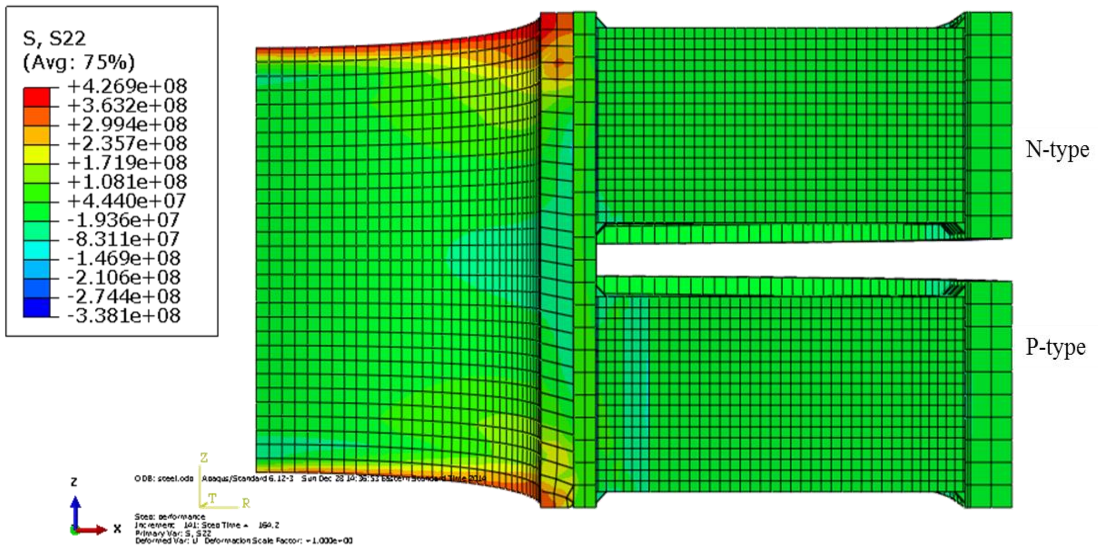

Figure 4.35. Circumferential stresses in the graphite ring inserted couple

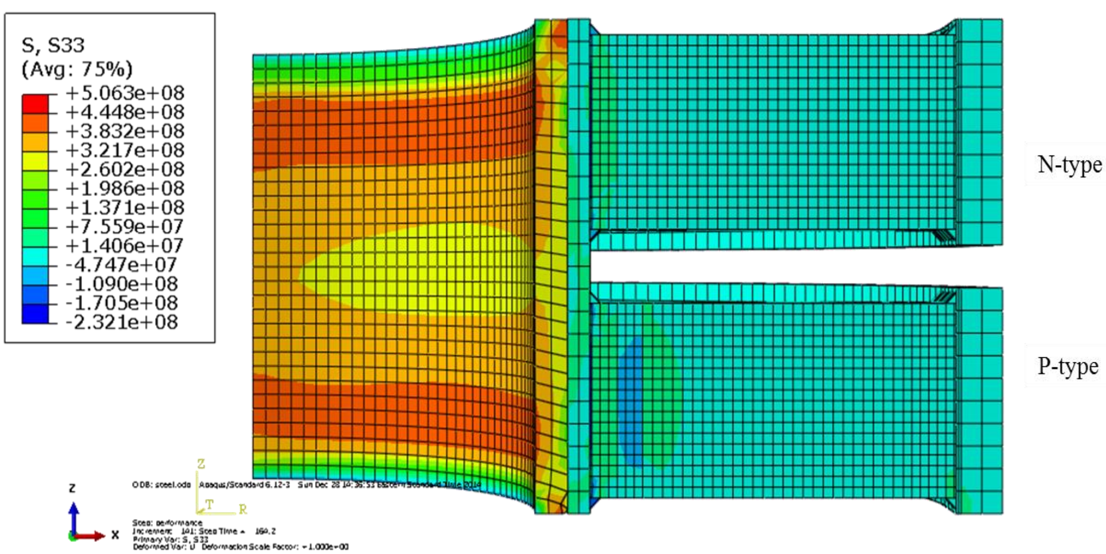

Figure 4.36. Axial stresses in the graphite ring inserted couple

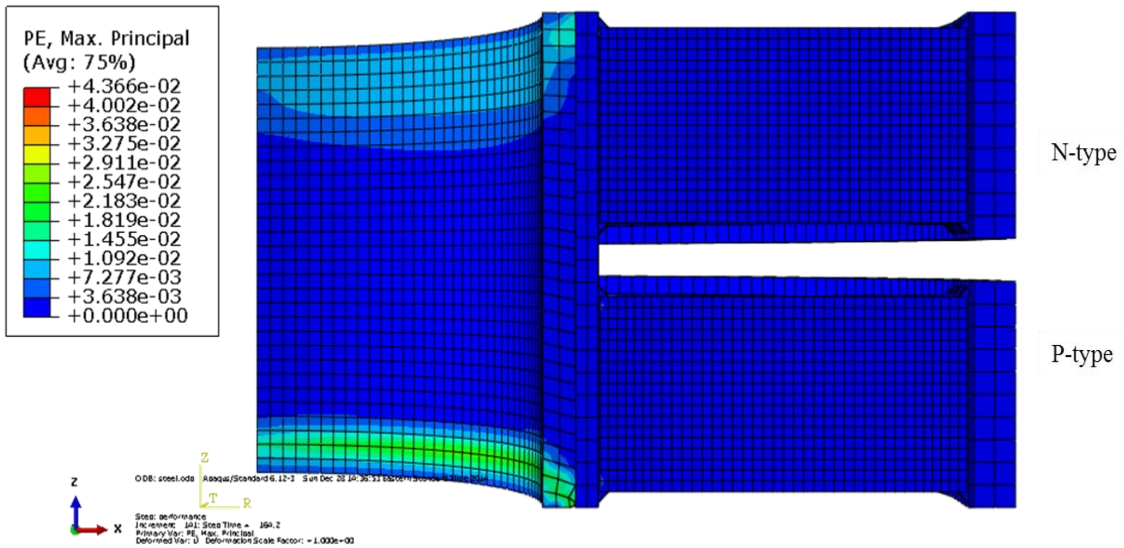

Figure 4.37. Maximum principal plastic strains in the graphite ring inserted couple

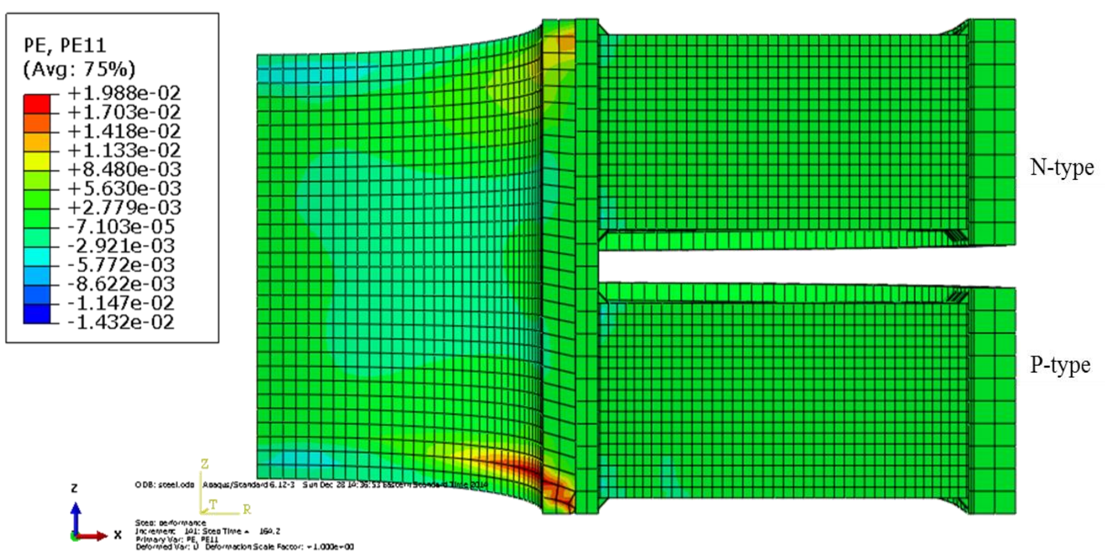

Figure 4.38. Plastic strains in x direction in the graphite ring inserted couple

4.1.3.4 Thermoelectric Couple Made by Outer Brass Ring and Inner Inconel Ring

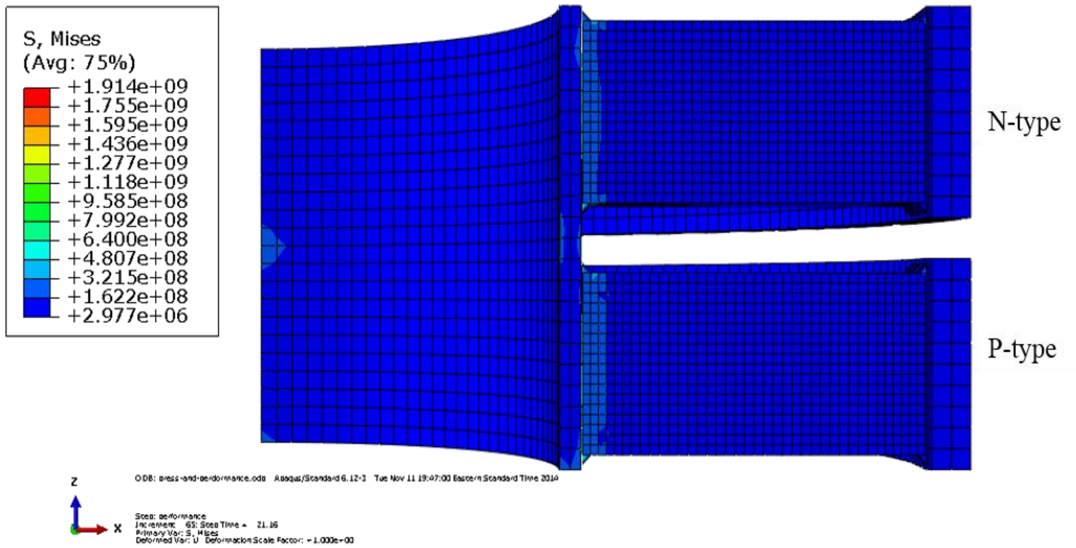

Figure 4.39. Mises stresses in N and P-type skutterudite

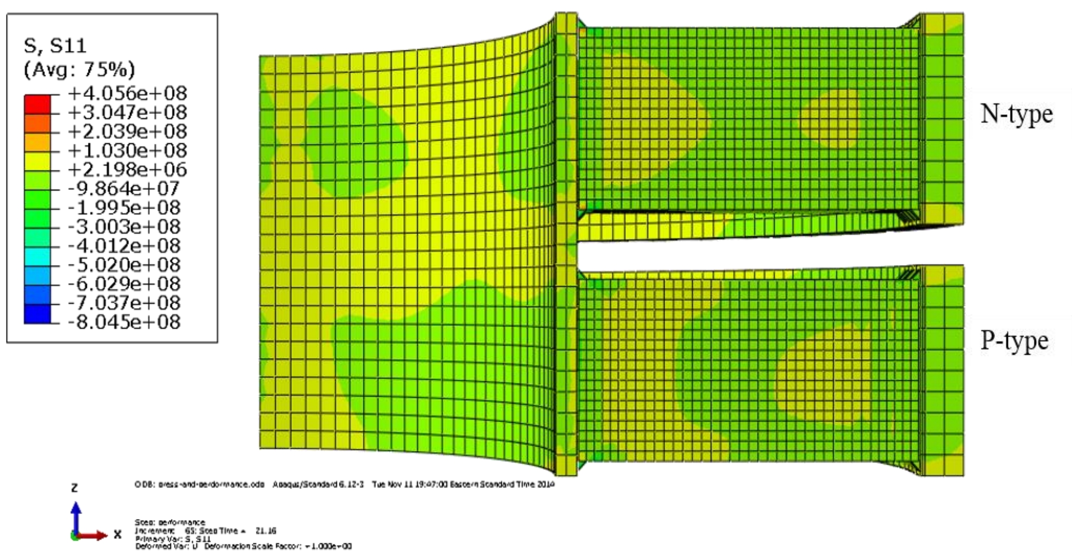

Figure 4.40. Radial stresses in N and P-type skutterudite

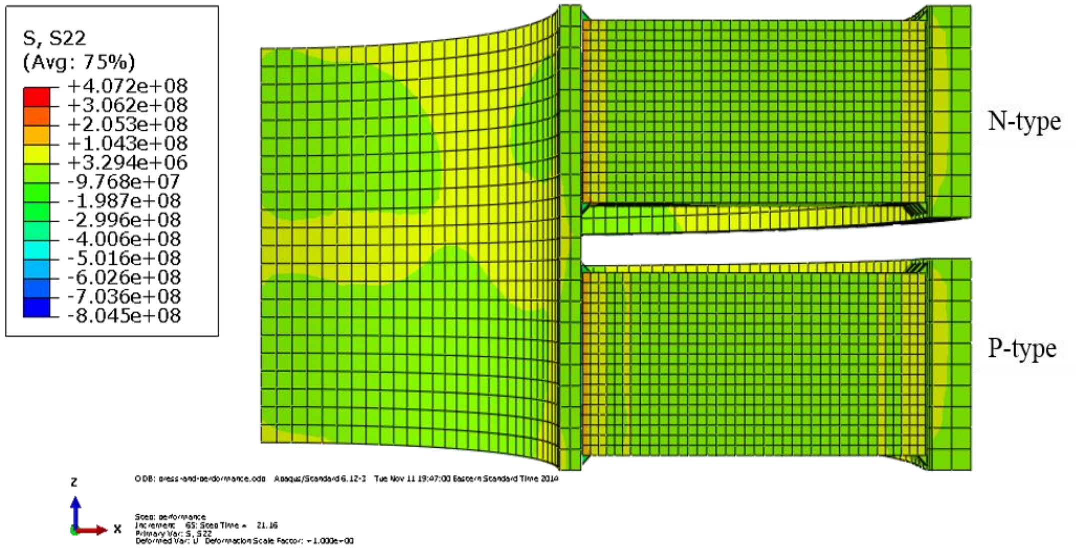

Figure 4.41. Circumferential stresses in N and P-type skutterudite

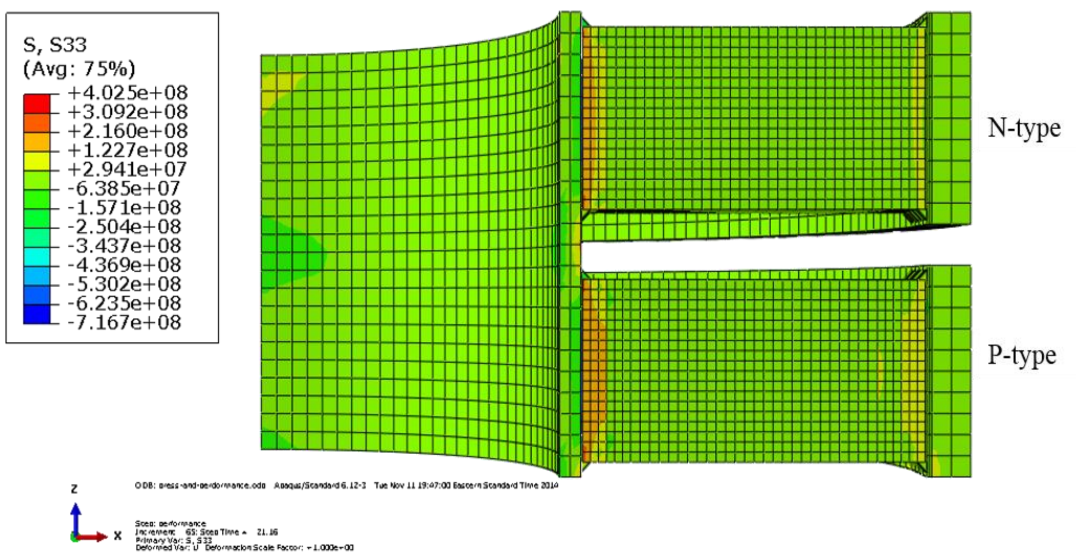

Figure 4.42. Axial stresses in N and P-type skutterudite

4.1.4 Finite Element Analysis Results of the Second Generation Thermoelectric Couple

Mises stresses distribution, as it is shown in **Figure 4.39,** are below the yield limit of different materials used in the assembled TEG which proves the fact that the TEG keeps its original shape after heating and cooling cycles. First generation thermocouples had a problem with thermal cracks due to residual tensile stresses after the hot pressing step. In the 2nd generation, there are no residual stresses in the assembly and the circular design keeps the couple in the compression all the time during its performance. **Figure 4.40** illustrates compression radial stresses in both N and P legs in the couple although there is a small amount of tensile circumferential and axial stresses in both legs which are considerably small to the yield strength of the Skutterudite. In addition, **Figure 4.41** and **Figure 4.42** show the circumferential and axial stresses in the section view of the couple.

2nd generation thermoelectric couple consists of two brass rings showed a drop in power output in the performance test every single time that it was tested. Excessive compressive stresses in the contact region of the inner brass ring and skutterudite legs can be seen in **Figure 4.24**. Applied heat and compressive stresses deform the brass ring permanently which reduces the contact area between the brass ring and skutterudite legs followed by increased in the resistance of the couple. The main reason of the power drop in the couple made by brass rings is the brass ring collapse. This problem existed when the brass ring assisted by graphite and steel rings. **Figure 4.32** and **Figure 4.38** show the plastic strain in x direction in the couple assisted by steel and graphite rings.

Collapse of the brass ring under thermal and compressive loads, due to the low Young's modulus, ended up by replacing the inner ring with Inconel 600 which has the elasticity modulus twice as the brass. The FE modeling showed all the stresses in the thermoelectric couple made by Inconel 600 are lower than the yield limit of the materials used in the TE couple.

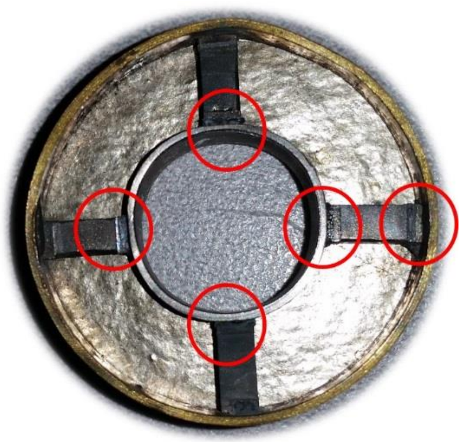

Figure 4.43. Collapsed brass ring after a performance test

4.2 1-D Engine Simulation (GT-Power)

Early in the proposal phase of this project, it was determined that an engine simulation code would be essential to the success of the project as a whole. Through the use of the simulation code, gas and wall temperature as well as heat flux can be predicted. This data is useful to the TE materials group in developing and selecting materials which perform optimally at engine operating conditions.

GT-Power is an industry standard 1-D engine simulation program from Gamma Technology which simulates pressure, temperature, and mass flow rate in different part of the engine and after-treatment system. GT-Power can be used for steady-state and transient simulations suitable for engine and powertrain control analysis for all types of IC engines. GT-Power uses 1-D gas dynamics to represent the flow and heat transfer in the engine model. The main role is to predict quantities such as power, torque, airflow, volumetric efficiency, fuel consumption, turbocharger performance and matching, pumping losses, and etc. Beyond basic performance predictions, GT-Power includes physical models for extending the predictions to include cylinder and tailpipe-out emissions, intake and exhaust system acoustic characteristics, in-cylinder and pipe/manifold structure temperature, measured cylinder pressure analysis, and control system modeling. These models may also be included in a full system level simulation within GT-Suite to provide accurate and physically based engine boundary conditions to the rest of the vehicle.

In GT-Power, the engine models can be very close to reality. To make the model works as a real engine, all the components down to the smallest pipe need to be imitated. To have a robust engine model in GT-Power, there are objects like cylinders, crankcases, pipes, turbochargers, catalyst convertors, and etc. are used which are easy to modify.

In GT-Power, the flow model involves the solution of the Navier-Stokes equations, namely continuity, the conservation of momentum and energy. These equations are solved in one-dimension, which all quantities are averages across the flow direction. There are two choices of time integration methods, which affect the solution variables and limits on time steps. The time integration methods include an explicit and an implicit integrator.

The primary solution variables in the explicit method are mass flow, density, and internal energy. The values of mass flow, density, and internal energy at the new time are calculated based on the conservation equations. In this method, the right hand side of the equations below is calculated using values from the previous time step. This yields the derivative of the primary variables and allows the value at the new time to be calculated by integration of that derivative over the time step. Note that the explicit solver uses only the values of the sub-volume in question and its neighboring sub-volumes. To ensure numerical stability, the time step must be restricted to satisfy the Courant condition. The small time steps required by this method make the explicit method undesirable for simulations that are relatively long (on the order of minutes in real time). However, it is well suited for highly unsteady flow where a high degree of resolution is already required to capture the extremes of the flow behavior. This method will produce more accurate predictions of pressure pulsations that occur in engine air flows and fuel injection systems and is required when prediction of pressure wave dynamics is important. The explicit method is recommended for the large majority of GT-Power simulations and lubrication, injection, or hydraulic system simulations over small time scales (normally less than 1 second). The exception in GT-Power is the simulation of the thermal response of an exhaust system from a cold start, without the engine. However, consideration of pressure pulsations is generally not necessary for cooling systems. Therefore, cooling system simulations generally use the implicit flow solver.

At each time step, the pressure and temperature are calculated in the following way:

1) Continuity and energy equations yield the mass and energy in the volume.

2) With the volume and mass known, the density is calculated yielding density and energy.
3) The equations of state for each species define density and energy as a function of pressure and temperature. The solver will iterate on pressure and temperature until they satisfy the density and energy already calculated for this time step. It is also possible for species change. The transfer of mass between species is also accounted for during iteration.

The primary solution variables in the implicit method are mass flow, pressure, and total enthalpy. This method solves the values of all sub-volumes at the new time simultaneously by iteratively solving a non-linear system of algebraic equations. This approach is useful for fluid system where high frequency pressure functions are not interest and typical simulation durations are higher. In the implicit method larger time steps may be taken. For this type of system the implicit solution is more efficient. While it has a significant advantage in terms of speed, the implicit solver should be used only in simulations that satisfy both of the following criteria:

1) There are minimal wave dynamics in the system, or accurate prediction of wave dynamics is not important.
2) The maximum Mach number in the system is less than 0.3

Because the implicit solution is iterative, it is important to verify that the solution for each step has numerically converged.

The whole system is discretized into many volumes, where each flow-split is represented by a single volume, and every pipe is divided into one or more volumes. These volumes are connected by boundaries. The scalar variables (pressure, temperature, density, internal energy, enthalpy, species concentrations, etc.) are assumed to be uniform over each volume. The vector variables (mass flux, velocity, etc.) are calculated for each boundary. This type of discretization is referred to as a staggered grid.

The conservation equations solved by GT-Suite are shown below. The left hand side represents the derivatives of the primary variables.

Continuity:
$$\frac{dm}{dt} = \sum_{boundaries} \dot{m} \tag{21}$$

Momentum:
$$\frac{d\dot{m}}{dt} = \frac{dpA + \sum_{boundaries}(\dot{m}u) - 4C_f \frac{\rho u|u|}{2}\frac{dxA}{D} - C_p\left(\frac{1}{2}\rho u|u|\right)A}{dx} \tag{22}$$

Energy:

(Explicit)
$$\frac{d(me)}{dt} = -p\frac{dV}{dt} + \sum_{boundaries}(\dot{m}H) - hA_s\left(T_{fluid} - T_{wall}\right) \tag{23}$$

Enthalpy:

(Implicit)
$$\frac{d(\rho HV)}{dt} = \sum_{boundaries}(\dot{m}H) + V\frac{dp}{dt} - hA_s\left(T_{fluid} - T_{wall}\right) \tag{24}$$

Where:

$\dot{m}$	Boundary mass flux into volume,
m	Mass of the volume
V	Volume
p	Pressure
ρ	Density
A	Cross-sectional flow area

A_s	Heat transfer surface area
e	Total internal energy per unit mass
H	Total enthalpy, $H = e + p/\rho$
h	Heat transfer coefficient
T_{fluid}	Fluid temperature
T_{wall}	Wall temperature
u	Velocity at the boundary
C_f	Skin friction coefficient
C_p	Pressure loss coefficient
D	Equivalent diameter
dx	Length of mass element in the flow direction (discretization length)
dp	Pressure differential acting across dx

Table 4.3. V6 Engine Specifications

Displacement	4.7 L
Bore	100 mm
Stroke	100 mm
Compression Ratio	10.5:1
Number of Valves	12

GT-Power was employed to create a model of the 6-cylinder V-configuration, naturally aspirated, direct-injected engine to determine exhaust gas properties as well as heat transfer to the duct walls of thermoelectric generator. The engine simulated has a displacement of 4.7L, and the bore and stroke are 100 mm. A schematic of the engine and after-treatment GT-Power models are shown in **Figure 4.44**. In the next step, the generated data is then used to provide the Star-CCM+ model and experiment as boundary and initial conditions. Mass flow rate and temperature of the exhaust gas after one the two last catalysts. Star-CCM+ was used to investigate the physical design of the TEG heat transfer configuration.

Table 4.4. Exhaust gas properties after catalyst

		Mass flow rate (gr/sec)	Inlet air temperature (˚C)	Engine load (bar)
Engine Speed	1000 RPM	10.40	464	3
	2000 RPM	29.50	553	3

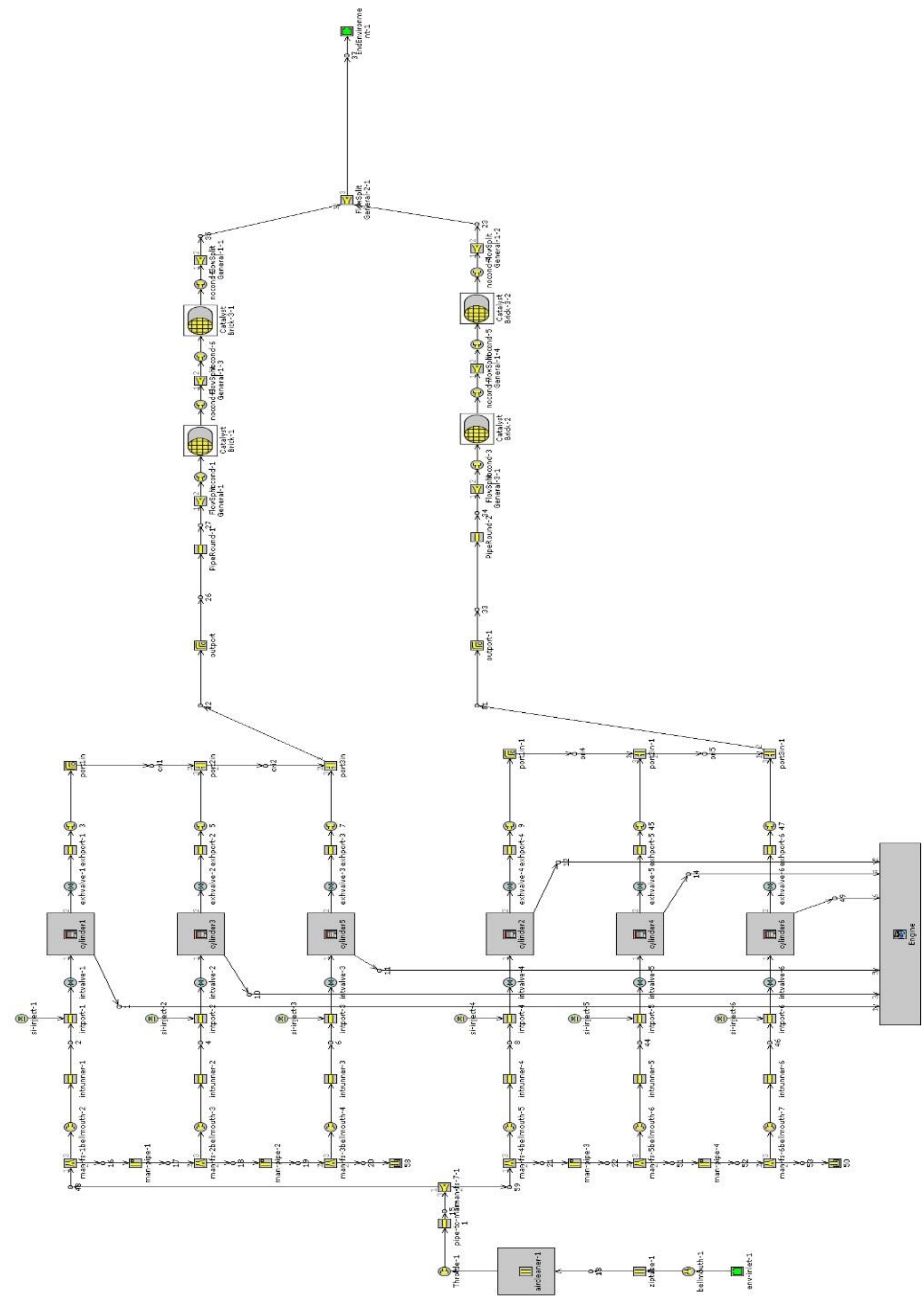

Figure 4.44. GT-Power model of the engine and after treatment system

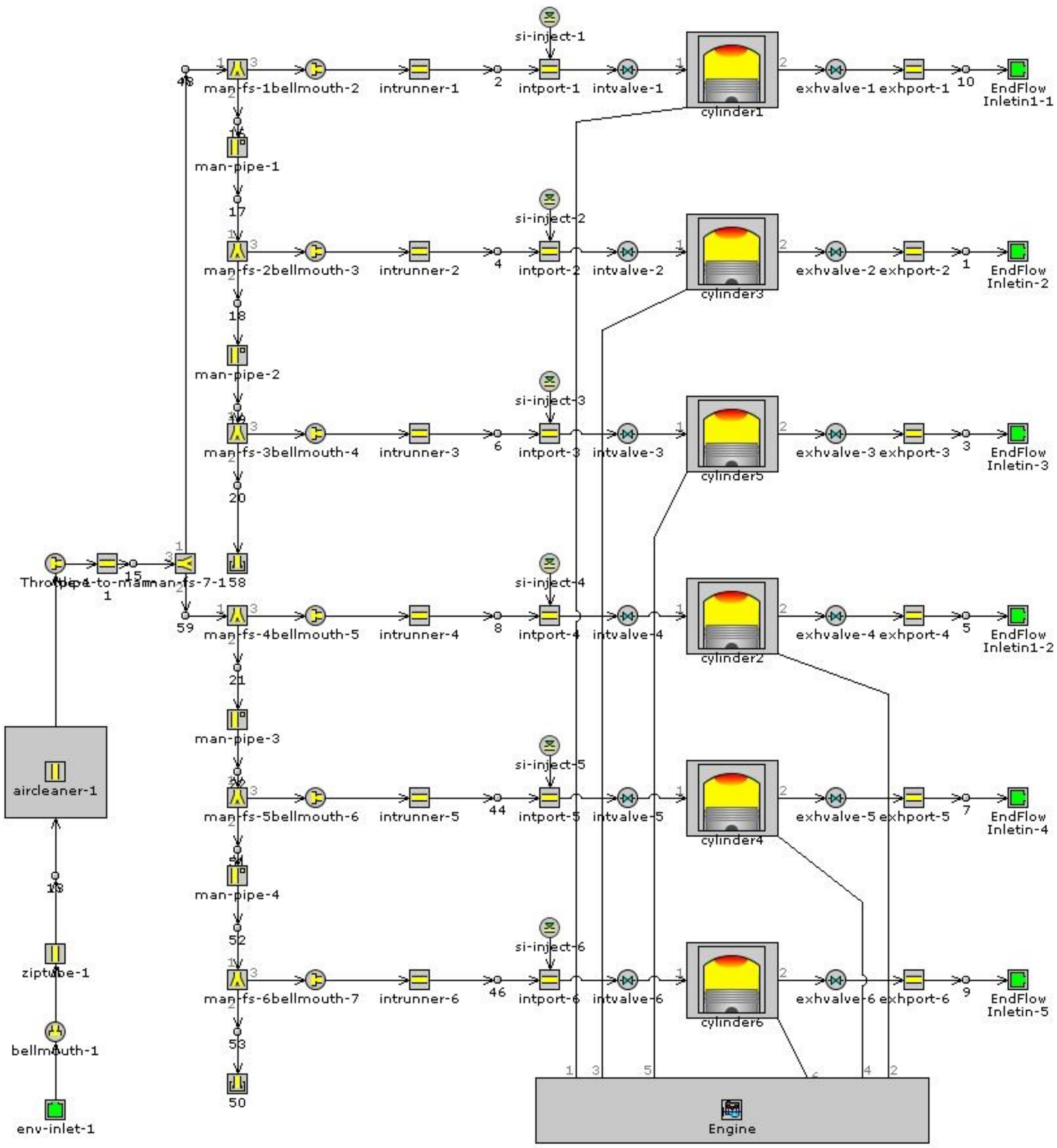

Figure 4.45. GT-Power model of the 4.7L V6 engine

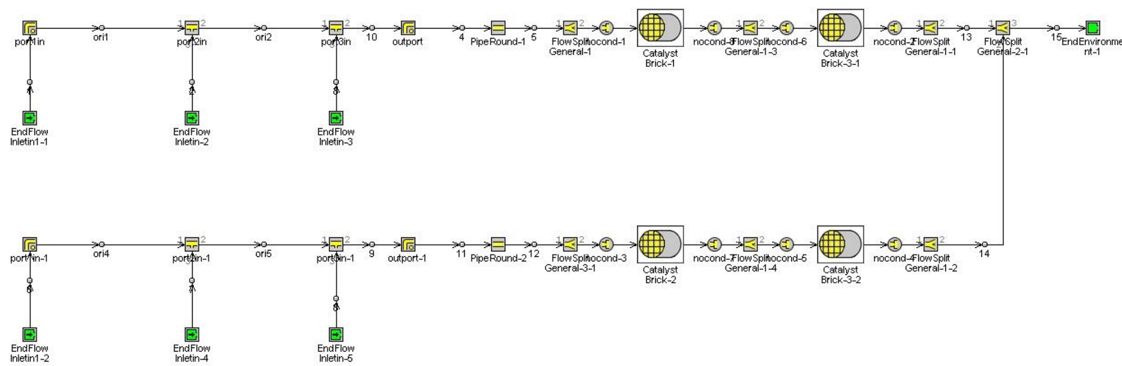

Figure 4.46. GT-Power model of the after-treatment system

4.3 Computational Fluid Dynamics (CFD) Simulations

Jet impingements are widely used in applications where high heat transfer rate is desired [67]. To improve the design of these systems, knowledge of the parameters affecting the heat transfer rate is required. The heat transfer rate from a jet impingement onto a surface is a complex function of many parameters such as: Nusselt number, Reynolds number, Prandtl number, nozzle geometry, flow confinement, turbulence, and dissipation of jet temperature [68].

The total computing domain includes fluid and solid parts. The temperature and flow fields of interest were obtained by solving Navier-Stokes equations (continuity, momentum, and energy) with respect to computational fluid and solid domains. Within the fluid domain, equations of mass, momentum and energy conversion are solved to model the fluid flow, heat and mass transfer. In the solid region, only heat transfer equation is needed.

Continuity: $$\frac{\partial \rho}{\partial t} + \nabla.(\rho u) = 0 \tag{25}$$

Momentum: $$\rho\left(\frac{\partial u}{\partial t} + u.\nabla u\right) = -\nabla\bar{p} + \mu\nabla^2 u + \frac{1}{3}\mu\nabla(\nabla.u) + \rho g \tag{26}$$

Energy: $$\rho\left(\frac{\partial E}{\partial t} + u.\nabla E\right) = \nabla u.\tau + \nabla.(k\nabla T) \tag{27}$$

CFD simulations were done to develop and design a jet impingement which is capable of delivering the same amount of heat to each of the thermoelectric couples. CFD simulation of the fluid region in the TEG has been performed by Star-CCM+ 9.06 to calculate the temperature, velocity, and pressure of the air inside the TEG. The purpose of using a jet impingement is achieving a uniform temperature and momentum flux delivery to each of the couples. Simulation of the prototype TEG CAD model using CFD software is a useful tool in developing the jet impingement component of the assembly.

This problem involves an incompressible gas. Fluid flow can be laminar or turbulent depending upon the Reynolds number and conditions of the flow that enter. When the flow in laminar, the used governing equations are continuity, Navier-Stokes, and energy equation for an ideal gas. On the other hand, when the flow is turbulent, the governing equations used are the ensemble-average continuity, Navier-Stokes, and energy equations for an ideal gas. The effects of turbulence were modeled by the two equation of k-ε model [69].

The transport equations for the standard k-ε model used by Star-CCM+ are:

$$\frac{d}{dt}\int_V \rho k dV + \int_A \rho k(v - v_g).da$$

$$= \int_A \left(\mu + \frac{\mu_t}{\sigma_k}\right)\nabla k.da \tag{28}$$

$$+ \int_V \left[G_k + G_{nl} + G_b - \rho\big((\varepsilon - \varepsilon_0) + \gamma_M\big) + S_k\right]dV$$

$$\frac{d}{dt}\int_V \rho\varepsilon dV + \int_A \rho\varepsilon\,(v - v_g).da$$

$$= \int_A \left(\mu + \frac{\mu_t}{\sigma_\varepsilon}\right)\nabla\varepsilon.da \tag{29}$$

$$+ \int_V \frac{1}{T}\left[C_{\varepsilon 1}(G_k + G_{nl} + G_{\varepsilon 3}G_b) - C_{\varepsilon 2}\rho(\varepsilon - \varepsilon_0) + \rho\gamma_y + S_\varepsilon\right]dV$$

S_k and S_ε are the user-specified source terms, and ε_0 is the ambient turbulence value in the source terms that counteracts turbulence decay [69].

k-ε model coefficients are:

$C_{\varepsilon l}$=1.44, $C_{\varepsilon l}$=1.92, C_μ=0.09 σ_k=1, σ_ε=1.3

The production G_k is evaluated as:

$$G_k = \mu_t S^2 - \frac{2}{3}\rho k\nabla.v - \frac{2}{3}\mu_t(\nabla.v)^2 \tag{30}$$

$$S = \frac{1}{2}(\Delta v + \Delta v^T) \tag{31}$$

If a non-linear model constitutive relation is used, the production due to the non-linear parts of the stress must be included. This production term is non-linear production G_{nl}. The production due to buoyancy G_b is evaluated as:

$$G_b = \alpha \frac{\mu_t}{\sigma_t}(\Delta T . g) \tag{32}$$

where α is thermal expansion coefficient, g is the gravitational vector, ΔT is temperature gradient vector, and σ_t is turbulent Prandtl number. $C_{\varepsilon 3}$ can be taken as constant everywhere or specified as below [70]:

$$C_{\varepsilon 3} = \{ \begin{matrix} 1 & for\ G_b \geq 0 \\ 0 & for\ G_b \leq 0 \end{matrix} \tag{33}$$

The dilatation dissipation γ_M is modeled according to Sarker as:

$$\gamma_M = \frac{C_M k \varepsilon}{c^2} \tag{34}$$

Where c is the speed of sound and C_M =2.

The Yap correction γ_y requires the computation of the wall distance. Therefore, it is only available when the standard k-ε model is used together with the two-later model.

$$\gamma_y = C_w \frac{\varepsilon^2}{k} \max\left[\left(\frac{l}{l_\varepsilon} - 1\right)\left(\frac{l}{l_\varepsilon}\right)^2, 0\right] \tag{35}$$

And the length scales are defined as:

$$l = \frac{k^{\frac{3}{2}}}{\varepsilon} \tag{36}$$

$$l_\varepsilon = C_l d \tag{37}$$

where d is the distance to the wall, C_w=0.83, and C_l=2.55.

Turbulent viscosity and turbulent time scale are:

$$\mu_t = \rho C_\mu k T \tag{38}$$

$$T = \begin{Bmatrix} \max(\frac{k}{\varepsilon}, C_t\sqrt{\frac{v}{\varepsilon}}) & \textit{without realizable scale option} \\ \min(\max(\frac{k}{\varepsilon}, C_t\sqrt{\frac{v}{\varepsilon}}, \frac{C_T}{\sqrt{3}C_\mu S}) & \textit{with realizable scale option} \end{Bmatrix} \quad (39)$$

Solutions to the governing equations were obtained by Star-CCM+ version 9.06. Steady-state solutions were pursued based on the fully coupled implicit algorithm to solve momentum, continuity, and energy simultaneously instead of in a segregated method. In the computation process, iterations were continued until all the residuals for all equations reach to a converged steady-state number. At convergence, the normalized residuals were always less than 10^{-5} for the three momentums (x, y, and z direction), 10^{-6} for the energy, 10^{-3} for the turbulent kinetic energy, 10^{-2} for dissipation rate of turbulent kinetic energy, and 10^{-3} for the continuity equation.

4.3.1 CFD Simulation of the Second Generation Thermoelectric 2-Couple Module

In the CFD modeling for the 2-couple module, the inlet gas temperature is set to 700 K and the velocity was 10 m/s. The outlet was assigned as a pressure outlet since it has the atmospheric pressure after that. The cooling was defined as a wall with a defined thermal resistance and the temperature of 300 K.

The components used for the CFD model for 2-couple module are shown in **Figure 4.47**. Holes for the jet impingement tube were places so they would be directly in line with the center axis of the individual N- and P-type legs. The meshed fluid region for the 2-couple assembly is presented in **Figure 4.48**. The CFD model is based on the k-ε turbulence-segregated fluid temperature for ideal gas. The polyhedral mesh base size was chosen as

0.0003 m. The advantage of using polyhedral elements is better approximation of the gradient compare to tetrahedral cells. Even along wall edges and at corners, a polyhedral mesh is likely to have a couple of neighbors which allow a reasonable predication of both gradients and local flow distribution [71].

Figure 4.49 shows the temperature distribution in the 2-couple assembly. In the last couple which is located at the outlet, the temperature goes up to almost 700 K which is 50 K higher than the inlet couple. In addition, there is a problem with the velocity which is higher in the last couple than the first couple. Jet impingement and two-couple assembly are shown in **Figure 4.50**. The combination of thermal stresses due to high temperature gradient and mechanical forces (momentum flux), the second couple fails all the time. Failure and collapse of the brass ring of the last couple cause drop in electric power output and rise of the resistance of the whole module.

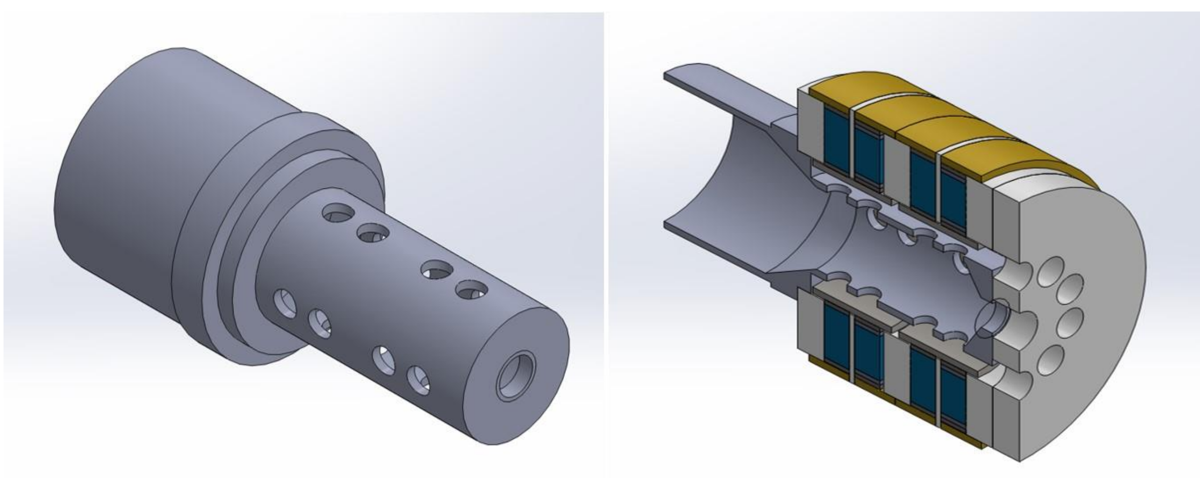

Figure 4.47. Jet impingement tube and two-couple assembly

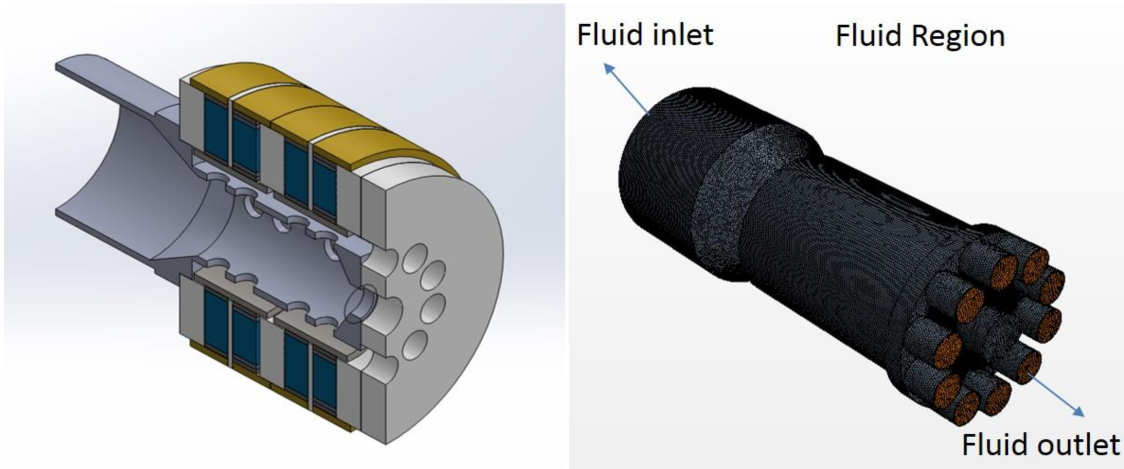

Figure 4.48. Fluid flow in meshed region for 2-couple module

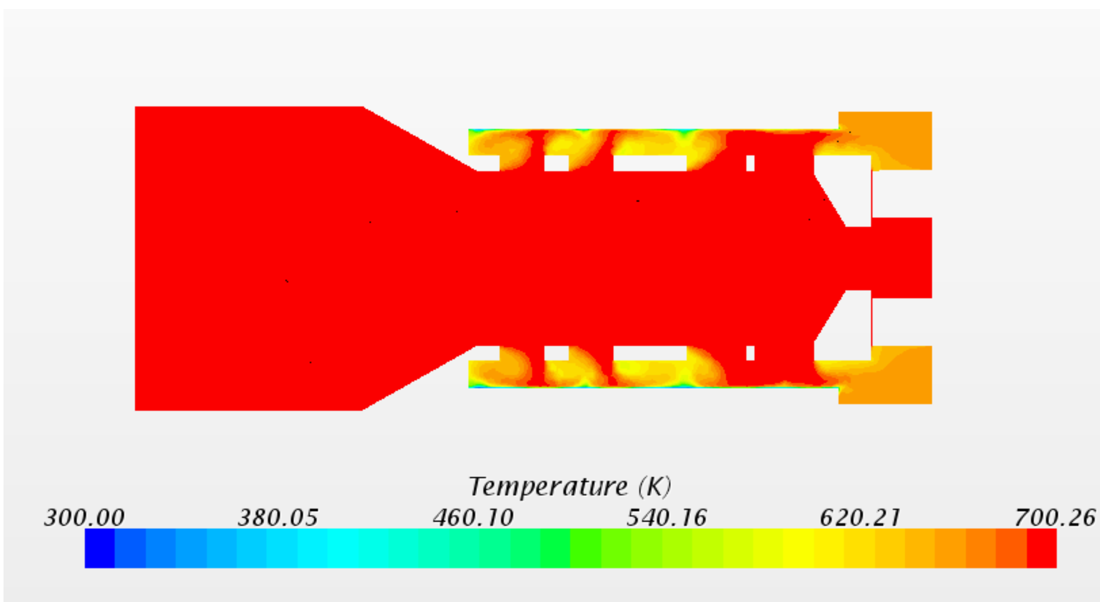

Figure 4.49. Temperature distribution for the 2-couple assembly

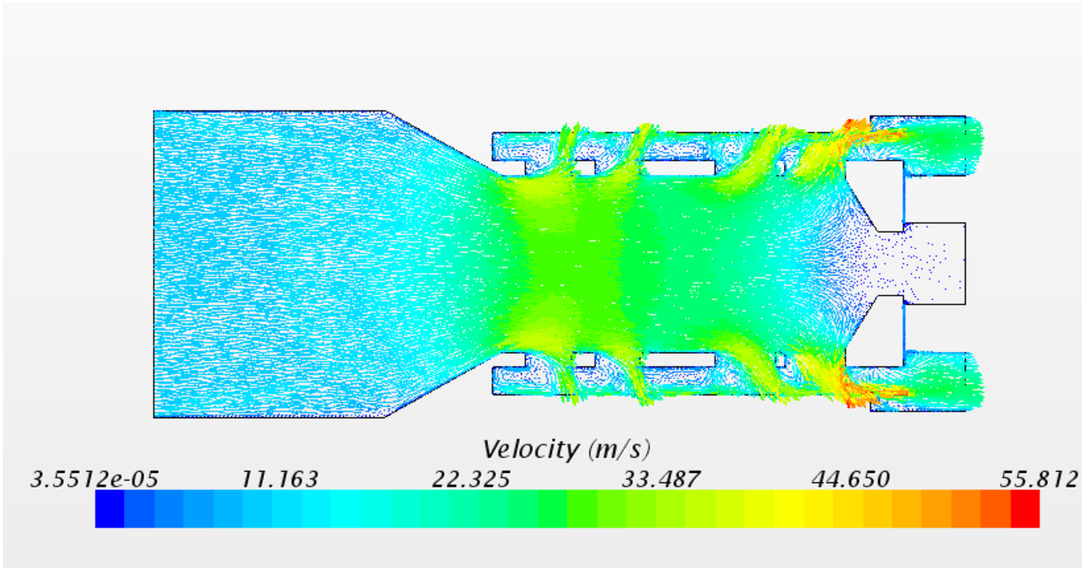

Figure 4.50. Velocity vectors for the 2-couple assembly

4.3.2 CFD Simulation of the Second Generation Thermoelectric 5-Couple Module

Designing a generator with only two couples per module is not realistic or efficient. As a matter of fact, for the real generator prototype there is a need of at least five couples per modules. In the previous sections, the specification of the 15W generator was explained. In this part, CFD simulation has been done for a 5-couple module and corresponded jet impingement to predict a uniform temperature distribution along the hot-side of the module.

The inlet gas temperature was set to 700 K and the inlet velocity was 10 m/s. The outlet was assigned as a pressure outlet, while the cooling jacket was defined as a wall with a temperature of 300 K.

The meshed fluid region for the 5-couple assembly is shown in **Figure 4.48**. Using the similar inlet temperature and air flow velocity, the CFD simulation shows a more uniform temperature distribution through all the jet compared to the 2-couple module (**Figure 4.51**). The velocity profile also appears to be more uniform compared to the 2-couple model (**Figure 4.48**). With more uniform temperature and air flow velocity, the probability of failure and collapse of any couples was expected to be decreased.

Figure 4.51. Meshed fluid region for 5-couple assembly used in the 15W prototype TEG

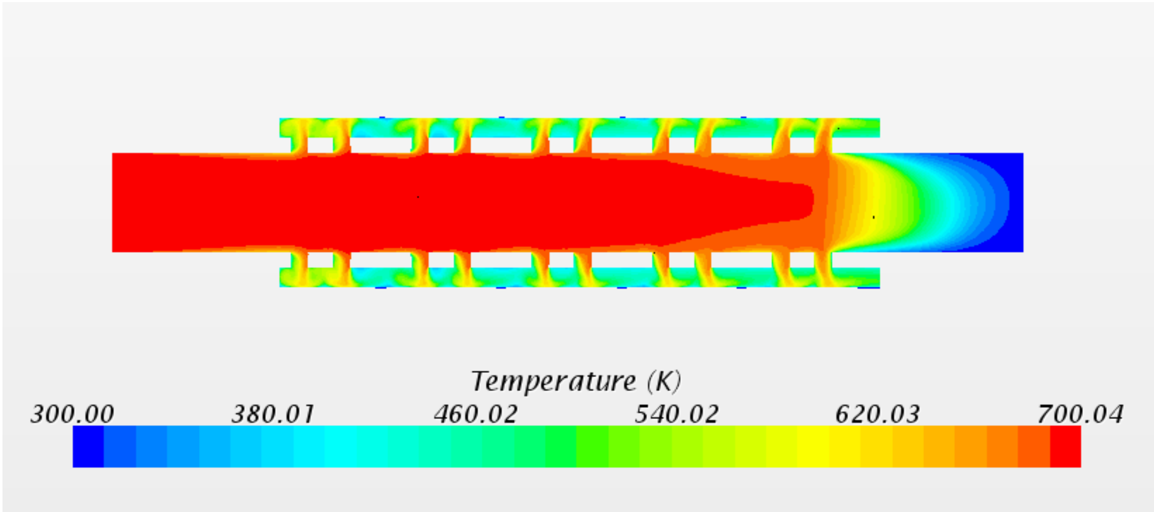

Figure 4.52. Temperature distribution in 5-couple assembly

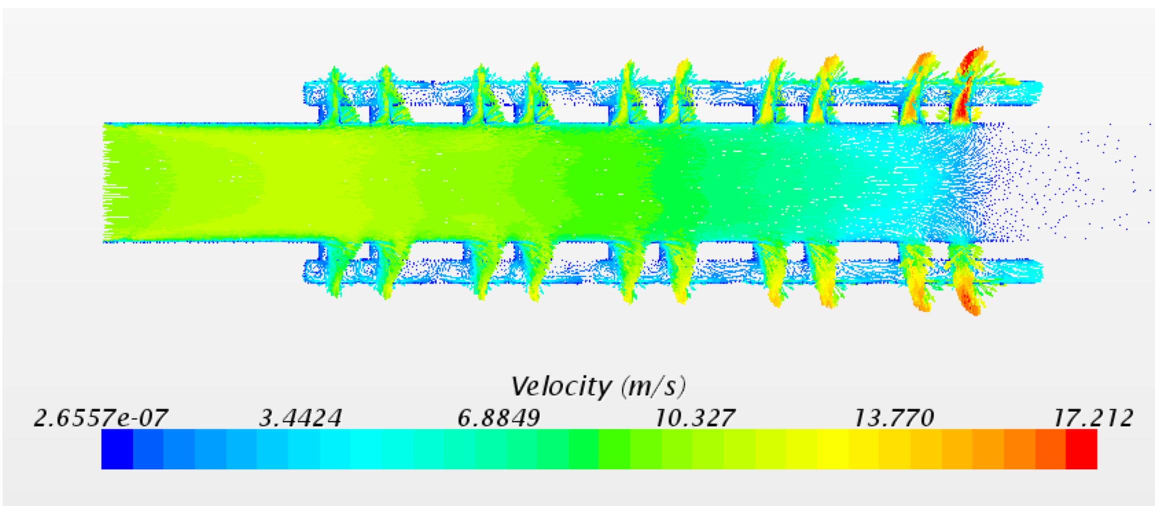

Figure 4.53. Velocity vectors in 5-couple assembly

4.3.3 CFD Simulation of the 15 Watts Thermoelectric Generator

Steady-state analysis of hot exhaust gas flow along the TEG was performed for the current study. Since the TEG is symmetric along two axes, only quarter of the domain is modeled and simulated in Star-CCM +.

The inlet gas temperature was set to 700 ˚C and the inlet mass flow rate was assigned as 8.5 gr/sec. The outlet was set as a pressure outlet, while the cooling jacket was defined as a wall with a temperature of 400 K. To check the accuracy of the model, the temperature of one point at the outlet was monitor and compared to the experimental results. Outlet temperature in the numerical model was reported as 567 ˚C while the actual temperature was 550 ˚C which shows 3.1% error between the actual and predicted model.

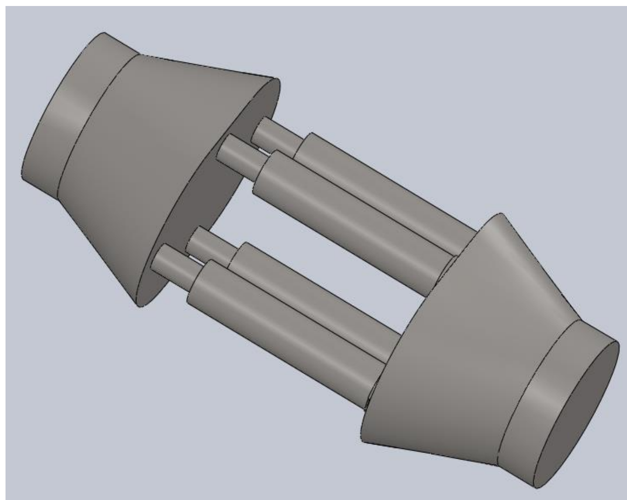

Figure 4.54. Fluid region in the generator

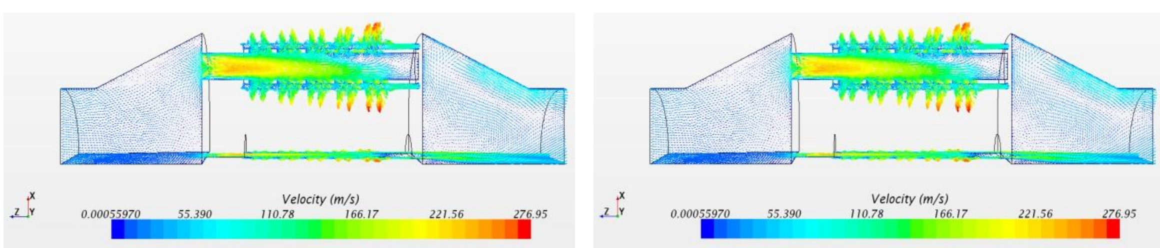

Figure 4.55. Velocity vectors in the TEG

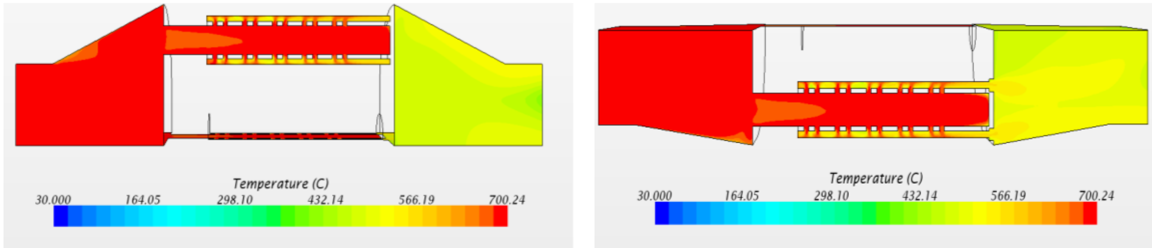

Figure 4.56. Temperature distribution in the TEG

4.4 Performance Testing

4.4.1 Performance of the First Generation Thermoelectric Circular Couple

The averaged results for first generation circular couples with brass rings pressed onto the couple in the big hot press are shown in **Figure 4.57** and **Figure 4.58**. The couples were cycled from hot to cold four times and then tested at a steady state for over an hour. The cyclic tests showed that the peak power output was initially 0.44 watts and dropped after subsequent cycle to 0.40 watts. A sample of one of the performance tests could be seen in **Figure 4.57**. Looking at the durability of the couples over a longer period of time, the couples were held at a steady state temperature and the power output data was recorded. The power output average remained steady at 0.33 Watts for 78 minutes as **Figure 4.58** shows.

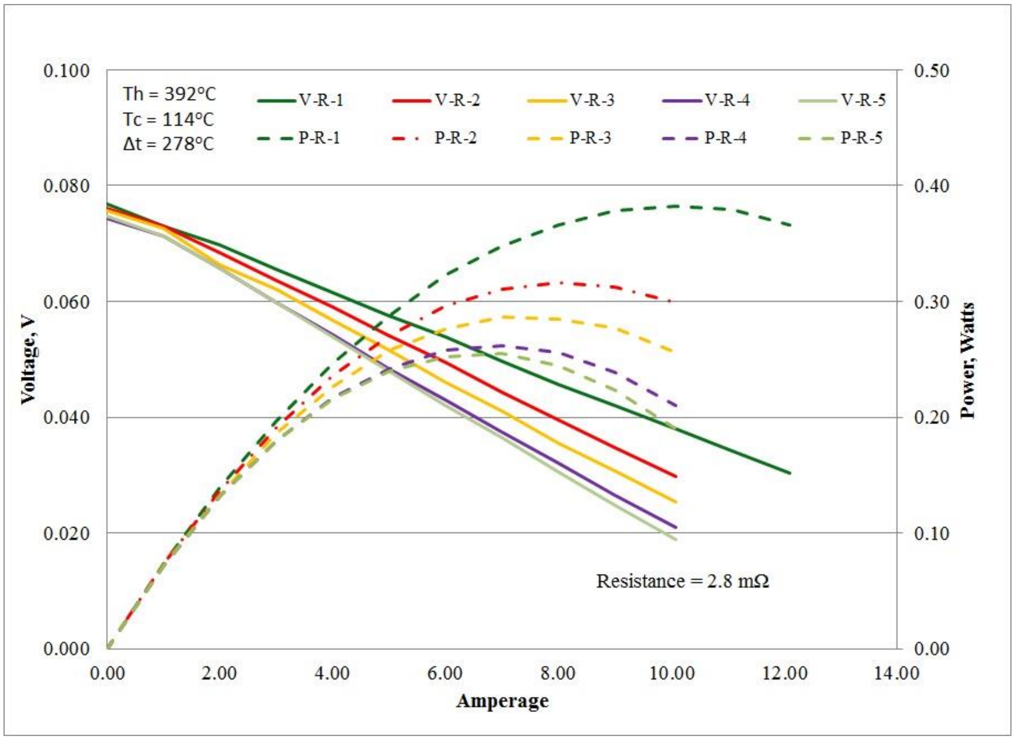

Figure 4.57. Averaged voltage and power output for circular couples in 4 cycles test

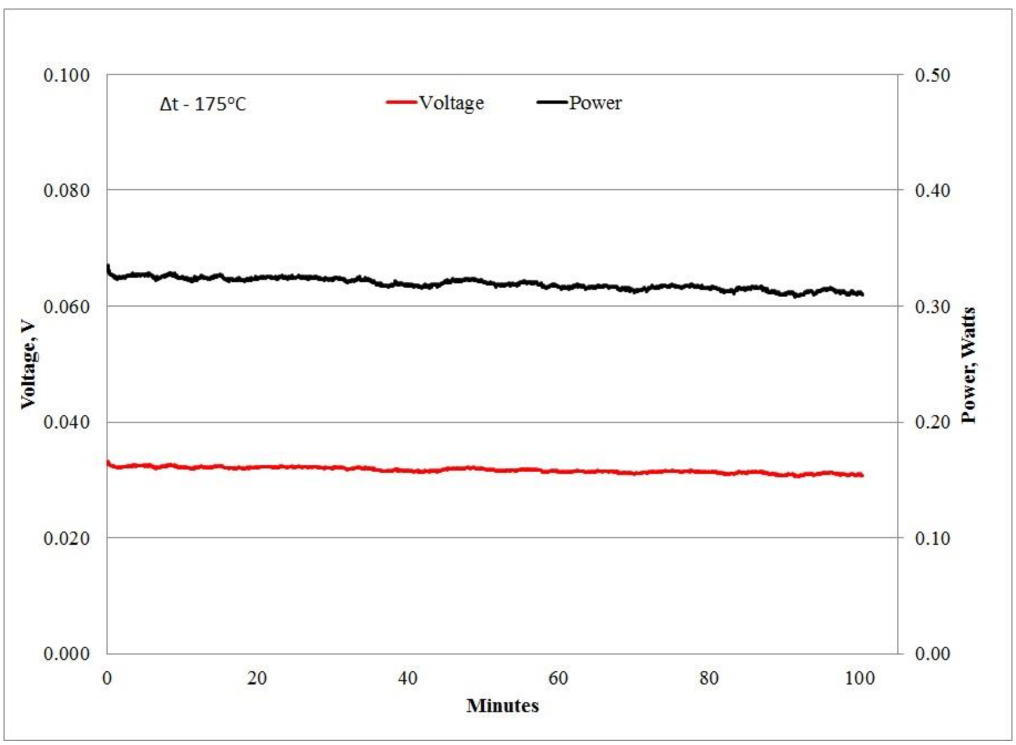

Figure 4.58. Averaged voltage and power output for circular couples

In addition to the approaches mentioned in the finite element analysis section, which contained different manufacturing approaches, other possibilities of cracking were studied. The main source as it was discuss dealt with the weakness of P-type skutterudite in tension. However, some other factors such as different thermal expansion coefficient between different materials used in the couple, state of bonding and cohesive zones between the assembled materials including titanium, Macor®, and skutterudite had been taken to the account. Conditions of the bonding between materials were clarified by placing the couple in the Scanning Electron Microscope (SEM). **Figure 4.59** and **Figure 4.60** show a reasonable bonding between skutterudite and titanium but a weak bonding between Macor® and skutterudite. Weak bonding causes the material slip on each other and cause cracking if the other side of one of the materials fixed. In addition, **Figure 4.61** shows skutterudite could easily be detached from Macor®.

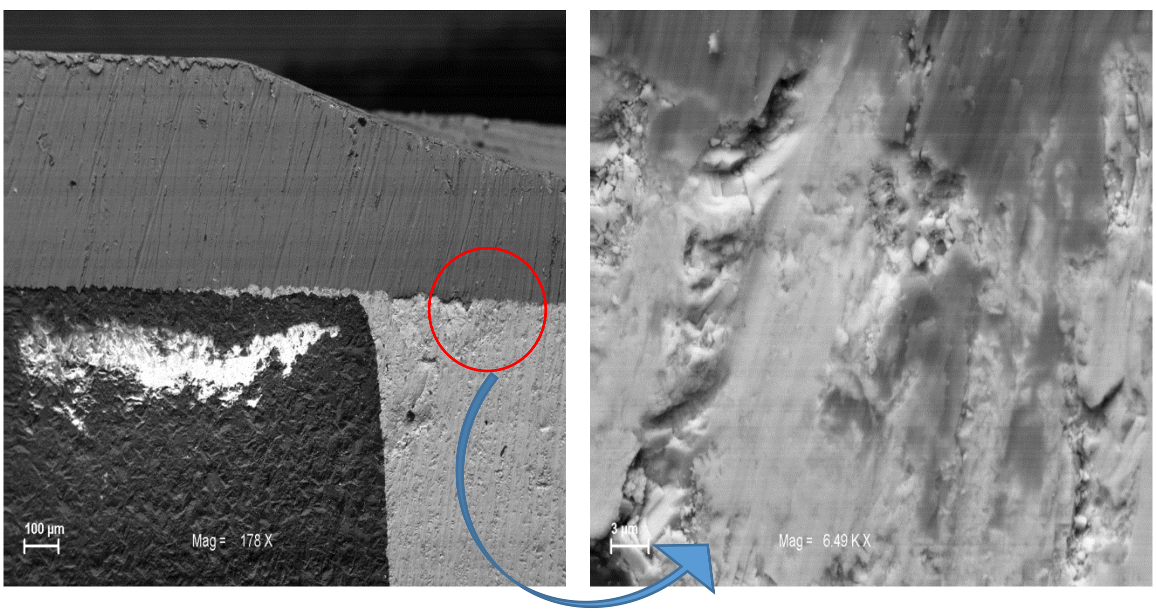

Figure 4.59. Titanium/skutterudite bonding

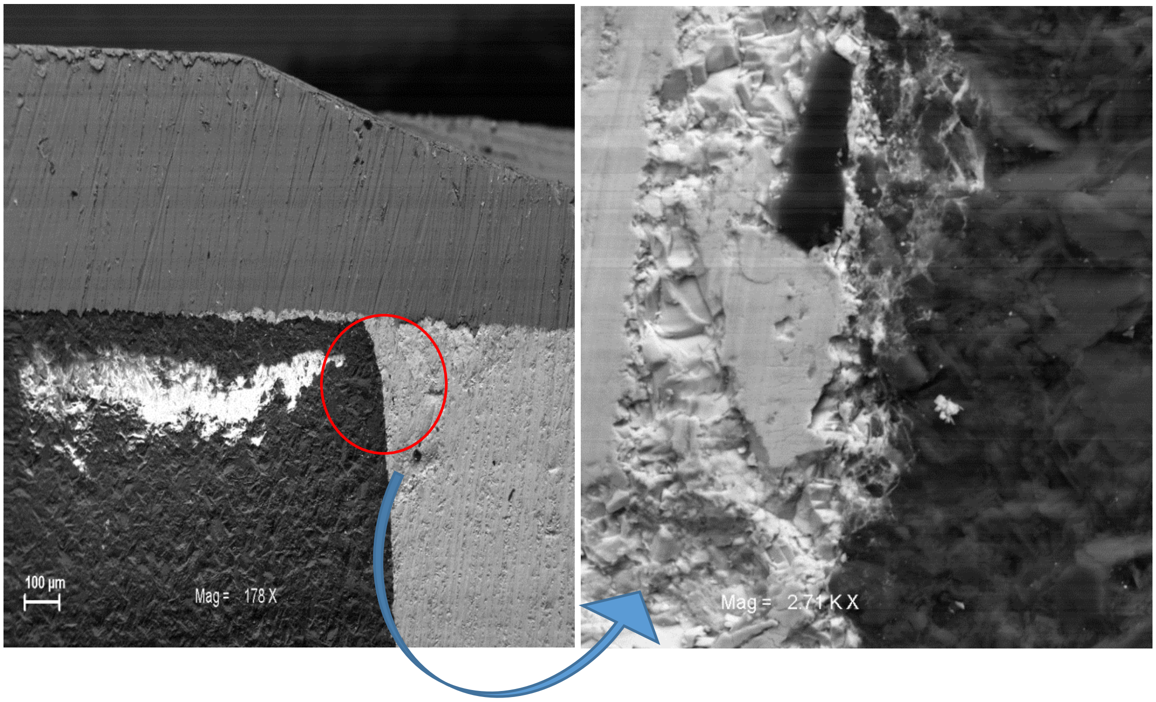

Figure 4.60. Macor®/skutterudite bonding

Figure 4.61. Weak Macor®/skutterudite bonding

In addition to bonding state between the materials, which it seems had issues, increasing tensile strength of the skutterudite could be a good option to have a crack-free thermoelectric couple. For this purpose, 0.5, 1, and 3% of xGnP, produced by the Composite Materials and Structures Center (CMSC) at Michigan State University, was used to increase the endurance limit of the skutterudite in tension. However, after adding the xGnP particles to the skutterudite, electrical resistance of the couple went up considerably. Looking at the samples in the SEM, it was observed the xGnP particles did not bond to the skutterudite. Those nanoparticles filled the voids between the skutterudite particles which are in the order of microns. The experiment showed adding xGnP to skutterudite does not solve the problem.

Figure 4.62. TE couple made with skutterudite reinforced with xGnP

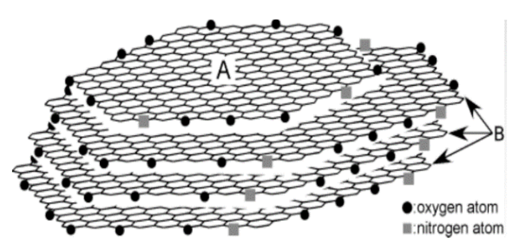

Figure 4.63. xGnP structure

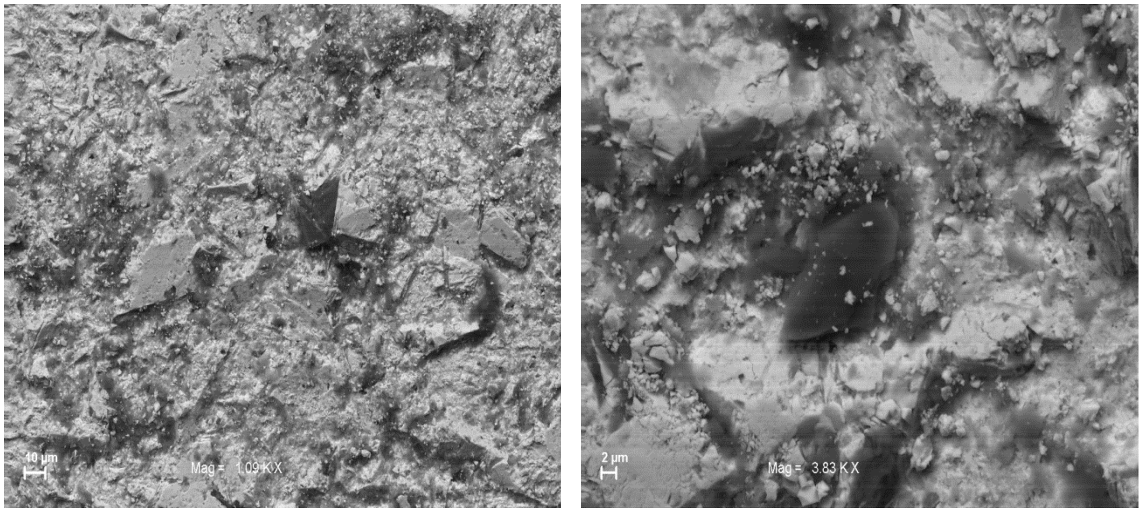

Figure 4.64. SEM image of the TE material ball-milled with 3% xGnP

Figure 4.64 is the SEM image of the TE material ball-milled with 3% xGnP. A scanning electron microscope is a type of electron microscope that produces images of a sample by scanning it with a focused beam of electrons. The electrons interact with atoms in the sample which creates a broad range of signals that can be detected. These signals contain information about the sample's surface topology and composition of the sample. SEM can achieve resolution better than 1 nanometer in high or low vacuum. With the help of the SEM, we recognized no bonding between the skutterudite and xGnP particles. Nano particles filled the voids and gaps between skutterudite particles which are in the order micrometer. **Figure 4.62** indicates there is no crack in the couple however, by looking at the sample in the SEM, we could able to see the low-strength bonding (no attachment) of the skutterudite and xGnP.

4.4.2 Performance of the Second Generation Thermoelectric Circular Couple

The averaged results for the second generation couples are shown in **Figure 4.65** to **Figure 4.74** for different test configurations. The assemblies were cycled 10 times. Cycles 5 to 10 were recorded. The results showed that the power curve and voltage remained constant.

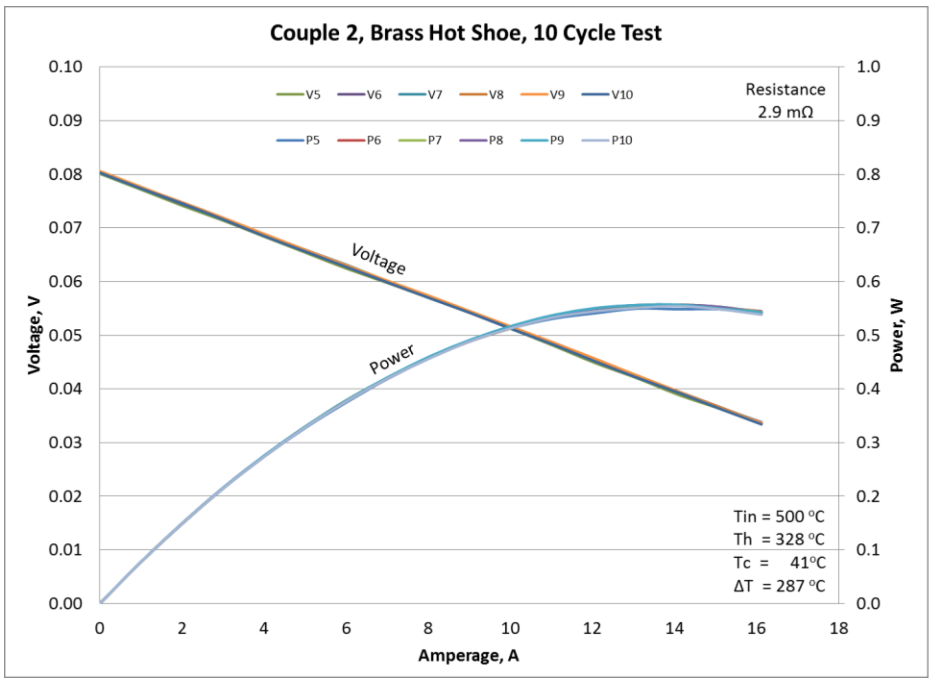

Figure 4.65. Voltage and power output for a brass hot shoe couple (5 cycles)

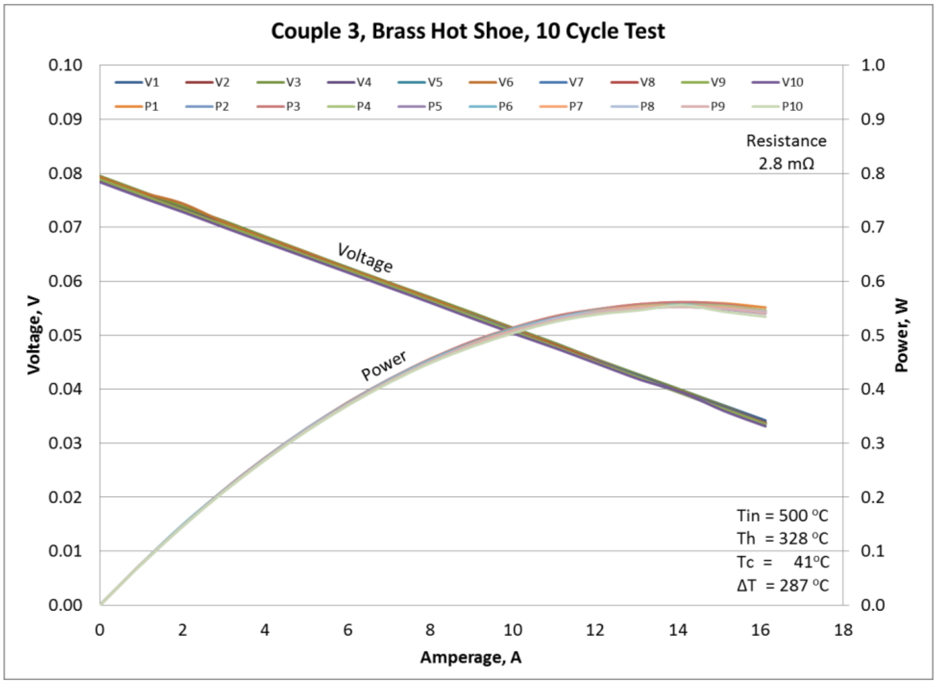

Figure 4.66. Voltage and power output for another brass hot shoe couple (10 cycles)

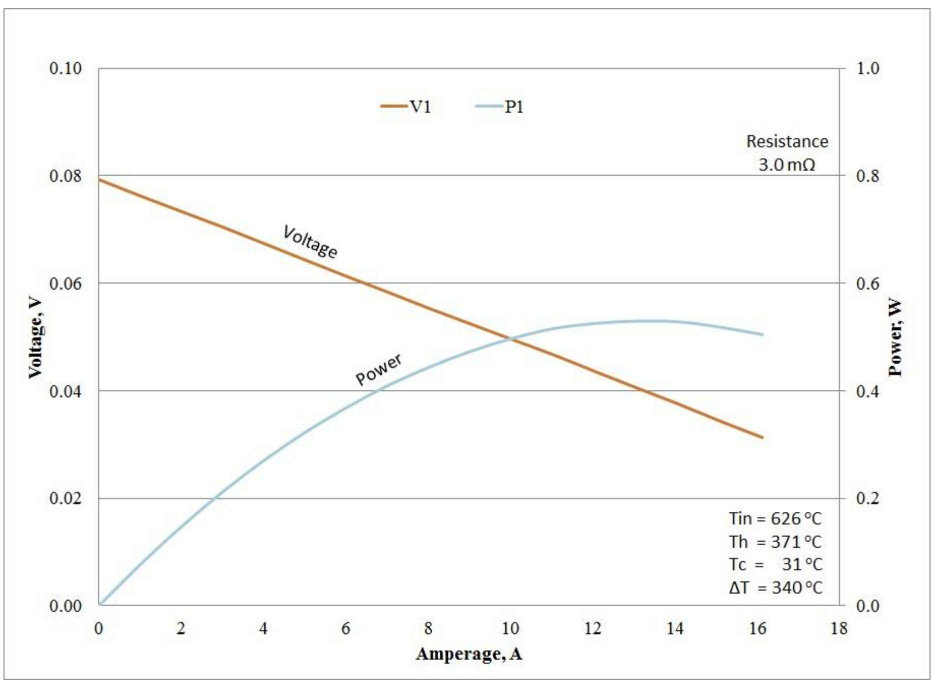

Figure 4.67. Voltage and power output, brass hot shoe/steel inserted

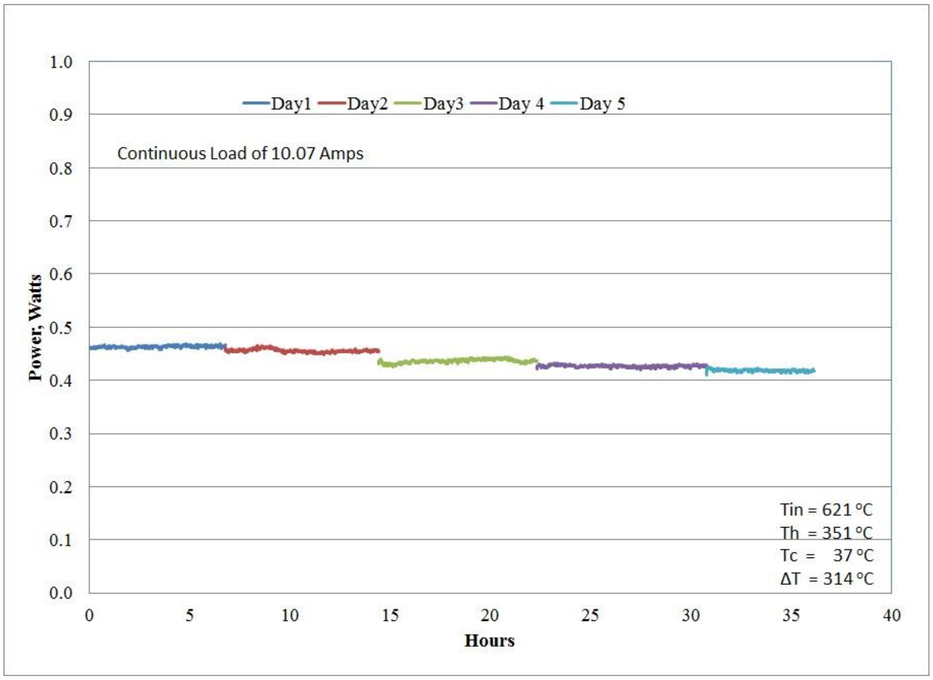

Figure 4.68. Power output durability, brass hot shoe/steel inserted

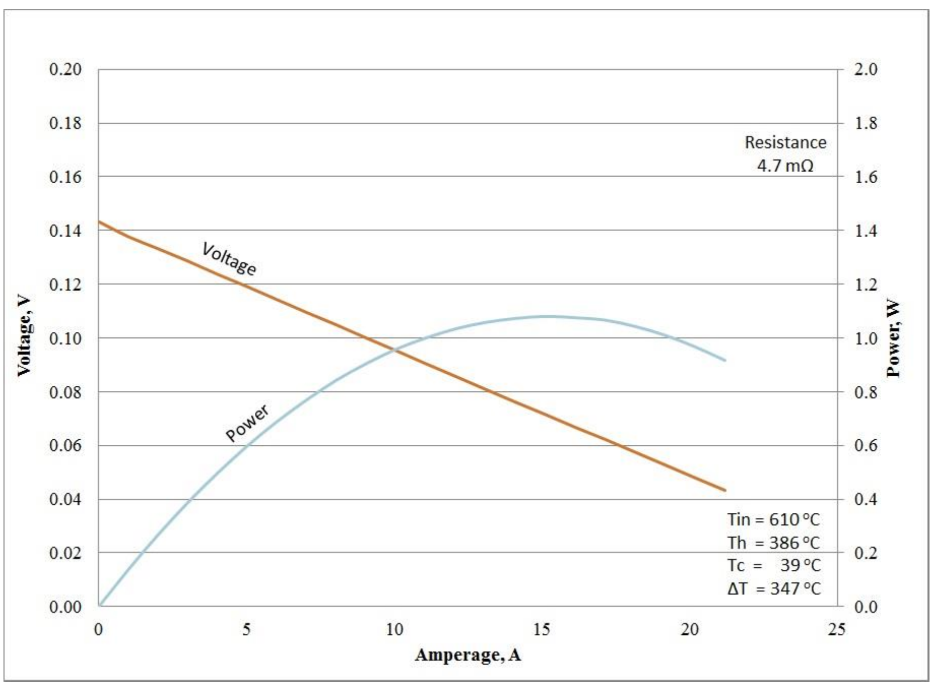

Figure 4.69. Voltage and power output, Copper hot shoe

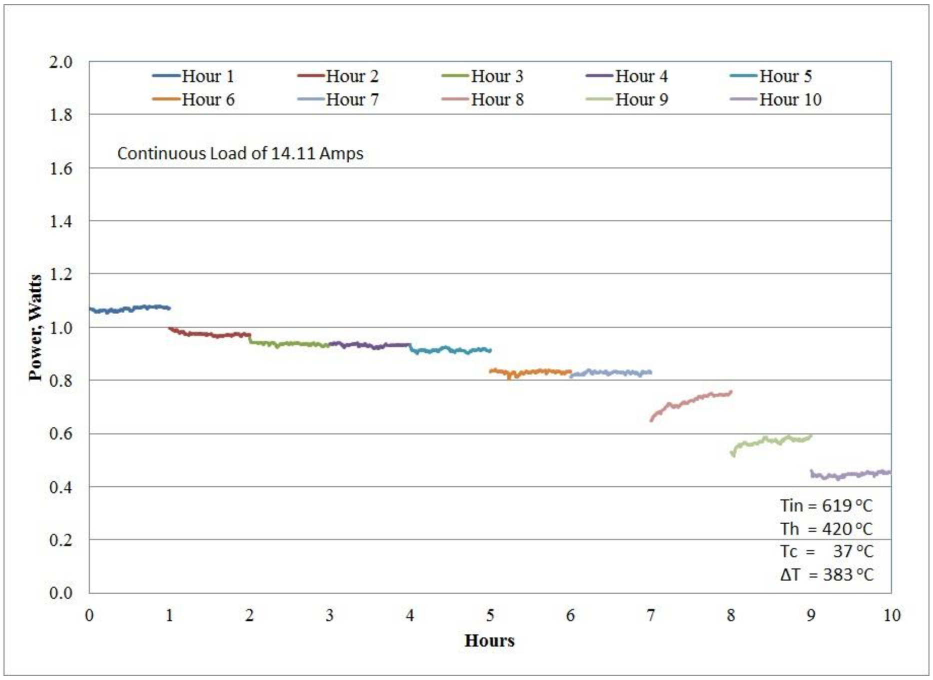

Figure 4.70. Power output durability, Copper hot shoe

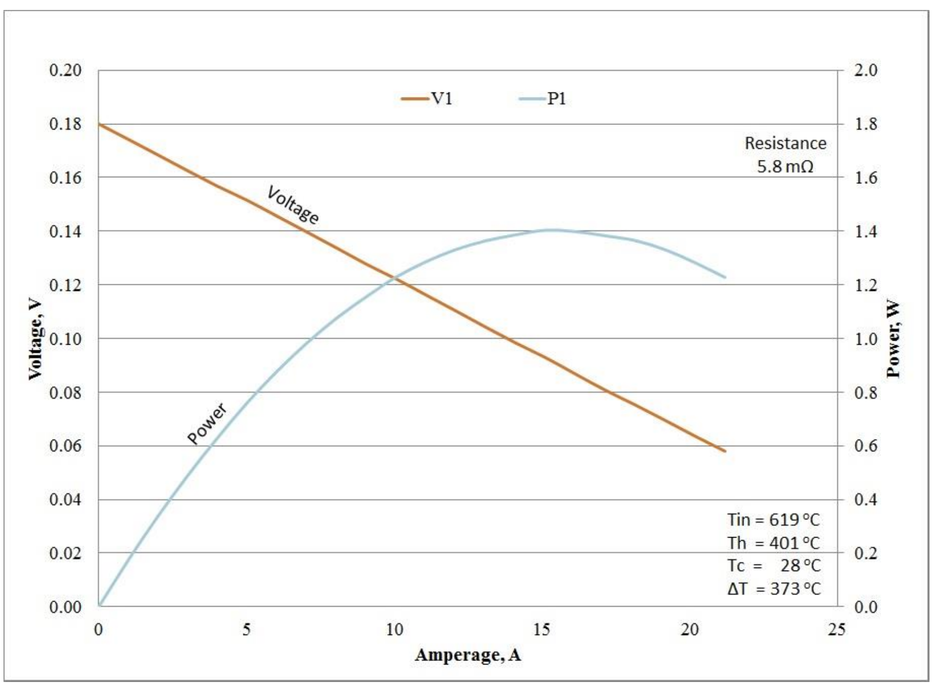

Figure 4.71. Voltage and power output, Brass hot shoe/Graphite inserted

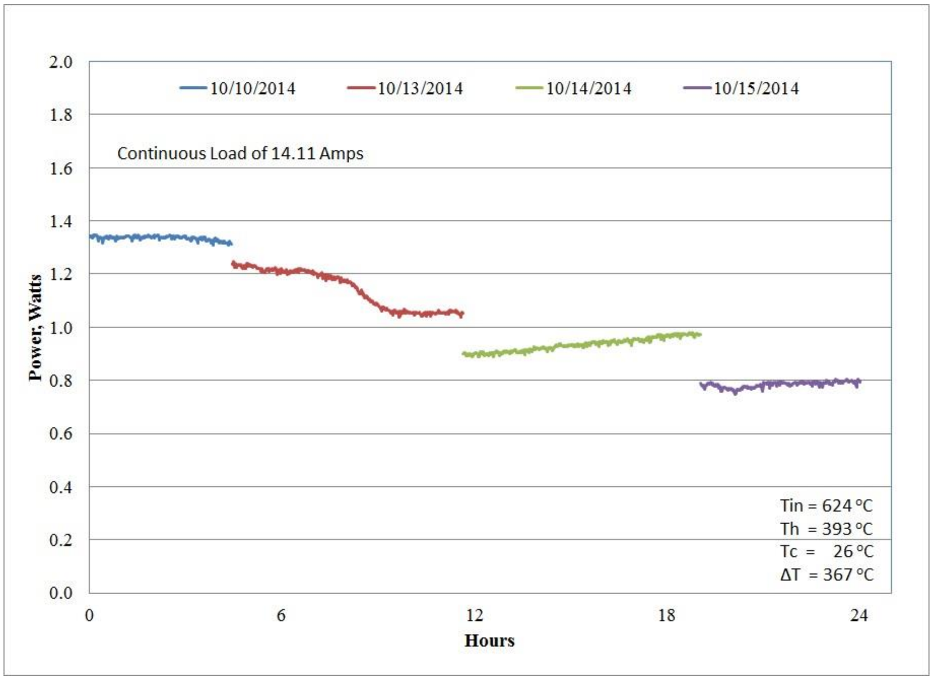

Figure 4.72. Power output durability, Brass hot shoe/Graphite inserted

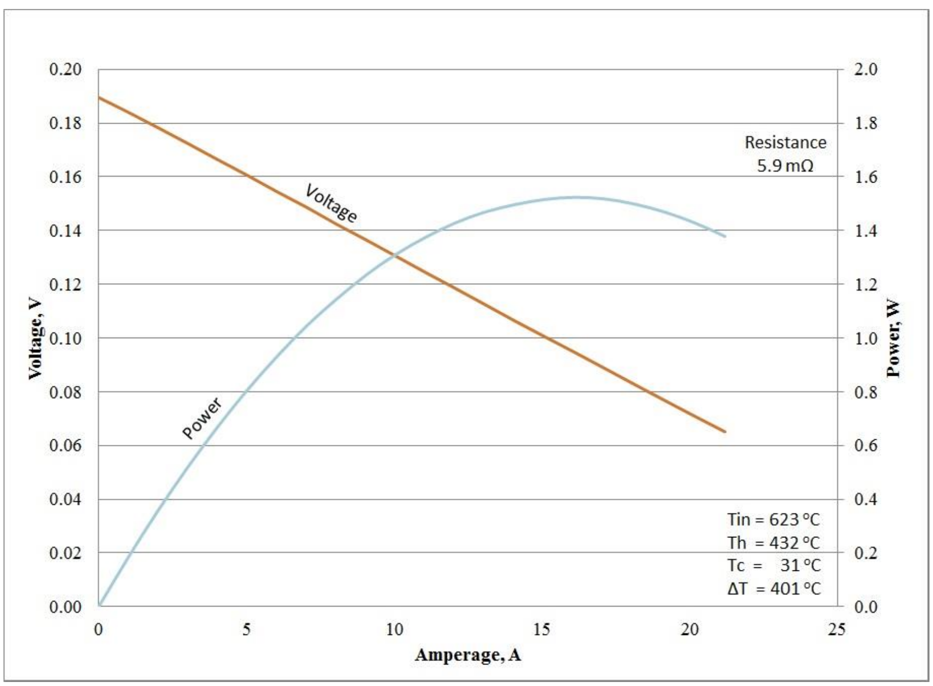

Figure 4.73. Voltage and power output, Inconel hot shoe

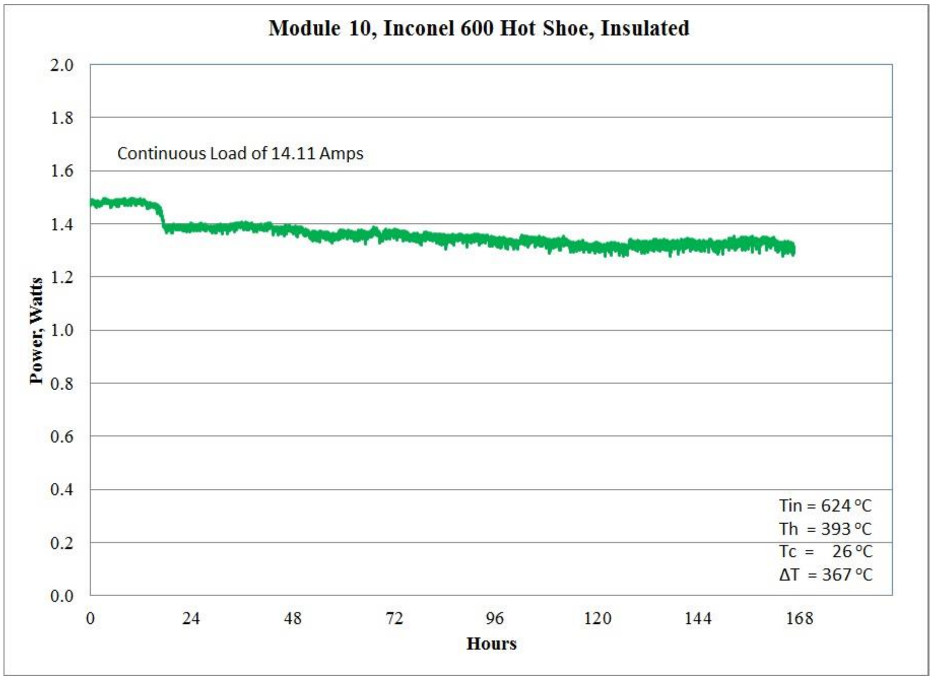

Figure 4.74. Power output durability, Inconel-600 hot shoe

Couples made by brass hot shoe were tested 10 times. Data for cycles 5 to 10 are reported here. Results in **Figure 4.65** show the power curve and voltage remain constant throughout the six recorded cycles. The peak power was 0.56 watts at 14.11 amps. Another couple assembled in the same way as the previous one was cycled. **Figure 4.66** shows the results of the power output and voltage. Power drop showed after the couple tested for a long cycle test.

To prevent the collapsing the inner brass ring in high temperature, two couples were assembled by inserting a steel or graphite ring into the inner brass ring. A single couple in the same configuration as inner brass ring was assembled with a steel ring pressed inside the brass hot shoe. The results for that couple are presented in **Figure 4.67** and **Figure 4.68.** A peak power of 0.53 watts was observed at 13.1 amps. The temperatures on the hot and cold shoes were 371 ˚C and 31 ˚C respectively. After the couple characterization, a 5-day cycling test was completed in a way the couple was tested for 8 hours at a steady state temperature and then allowed to cool down to room temperature prior to testing again. The couple was back loaded with a continuous load of 10.07 amps during each test. Results from the 5-day test showed the couple initially produced 0.46 watts of power and then dropped approximately 9% by day 5 to 0.42 watts. **Figure 4.76** and **Figure 4.77** show the detachment of the brass ring and copper layer in the leg. The gap caused by this failure, increased the resistance of the couple which has an invert relation with the power output.

Another approach, to prevent failure, was using a two couple module with a thicker wall copper hot shoe. The new module was cycled ten times for one hour period to complete the performance test. The results of performance characterization and cycling tests are presented in **Figure 4.69** and **Figure 4.70.** In the initial test, the module power output was recorded as 1.08 watts at 16.12 amps, but afterwards it decreased to 0.61 watts at 9.05 amps. The power loss during each cycle was caused by oxidation forming on the copper hot shoe. Oxidation increased the resistance of the copper hot shoe followed by the power drop of the module.

$$2Cu(s) + O_2(g) \xrightarrow{\Delta \approx 300℃} 2CuO(s) \tag{40}$$

Figure 4.75. Before (left) and after (right) testing photo of a module with copper hot shoe

Two couples in the same configuration as the previous couple with inserted steel ring were assembled. Prior to the assembly, a thin graphite tube was inserted inside each of the brass hot shoes. The graphite tube was used to prevent the brass hot shoe from deforming under high temperature loads. The module was tested for performance and then cycled during ten 1-hour test as previously described. The results for the initial power output of the model before and after cycling were 1.40 and 1.36 watts at 15.11 amps (**Figure 4.71**). There was a slight increase in overall resistance of the module from 5.8 to 6.1 mΩ. A continuous load of 14.1 amps was applied during each one-hour tests while the temperature on the hot side was held at a steady state of 393 ˚C. The initial power output for hour 1 was 1.37 watts and it decreased to 1.34 watts in test 10. This represents a 2% loss in total power. **Figure 4.78** and **Figure 4.79** are the SEM pictures of TE couples which the inner brass ring was assisted by a steel or graphite tube inserted into it. These set of TE couples still had the same problem which original couple had. Detachment of the inner brass ring and copper foil in the TE legs increased the electrical resistance and decreased the power output of the couple.

Finally, using the thermoelectric couple with inner Inconel ring and outer brass ring was finalized since Inconel was stiffer and it did not deform while exposed to the heat loads. Couples with inner brass rings or steel ring inserted started losing their power output because the brass and steel ring go to their plastic limit easier when they heated up. Collapsing the inner ring caused the disconnection of the skutterudite legs and inner ring followed by power output drop. Inconel 600 is a nickel-chromium alloy with good oxidation resistance at higher temperatures. It also has excellent mechanical properties and a combination of high strength and workability. A module using two couple with Inconel 600 hot shoes was assembled and tested for power performance (**Figure 4.73**). K-wool insulation was also added to the void space in the couples during the assembly of the module. The hot and cold side temperatures were recorded as 432 ˚C and 31 ˚C respectively. The total power output of module was 1.52 watts at 15.11 amps. Compared to all the previous modules, Inconel hot shoe module had the highest power output. A long-term test of the module was completed after the initial performance test. The hot air into the module was kept at steady state temperature of 408 ˚C for a total of 185 hours. The power output dropped about 7% but it stayed constant for the rest of the test (**Figure 4.74**). Proof of the durability of the new thermoelectric couples made by Inconel inner rings could be obtained by taking some SEM pictures to make sure all the layers and bonding in the couple stay firm and rigid. **Figure 4.80** shows the existence of no gaps in the TE couple which is the main and the most important factor to have a reliable couple under thermal cyclic loads.

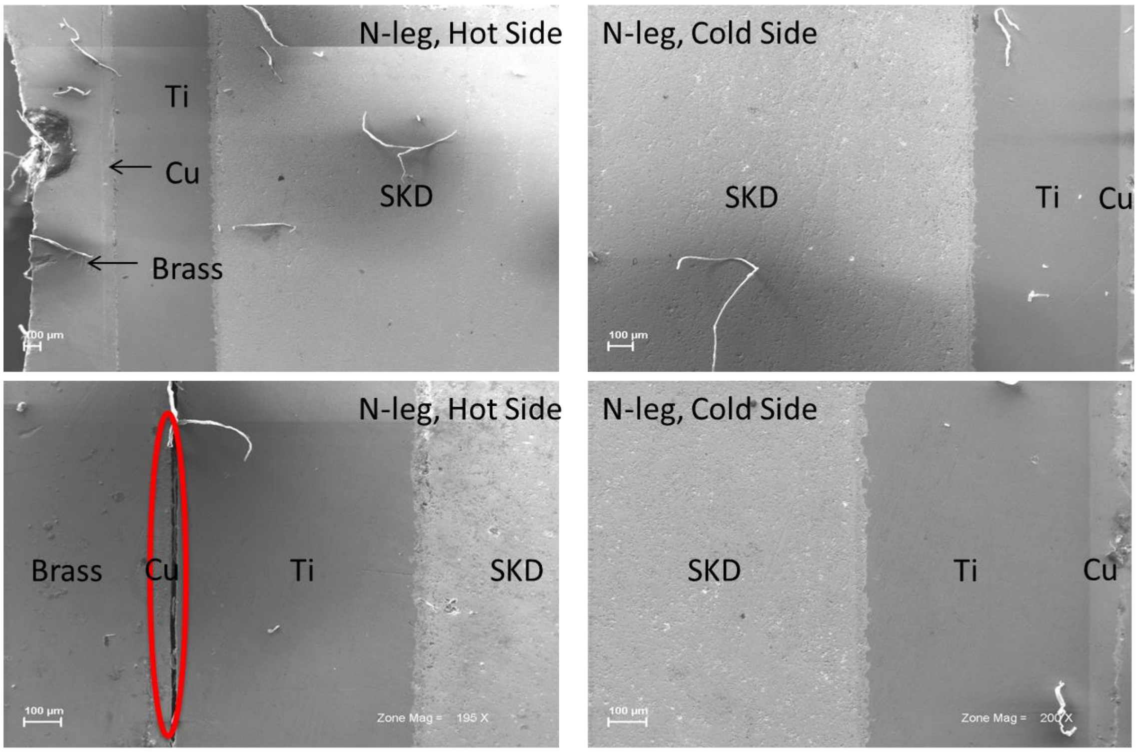

Figure 4.76. SEM image of the TE couple made of two brass rings (N-leg)

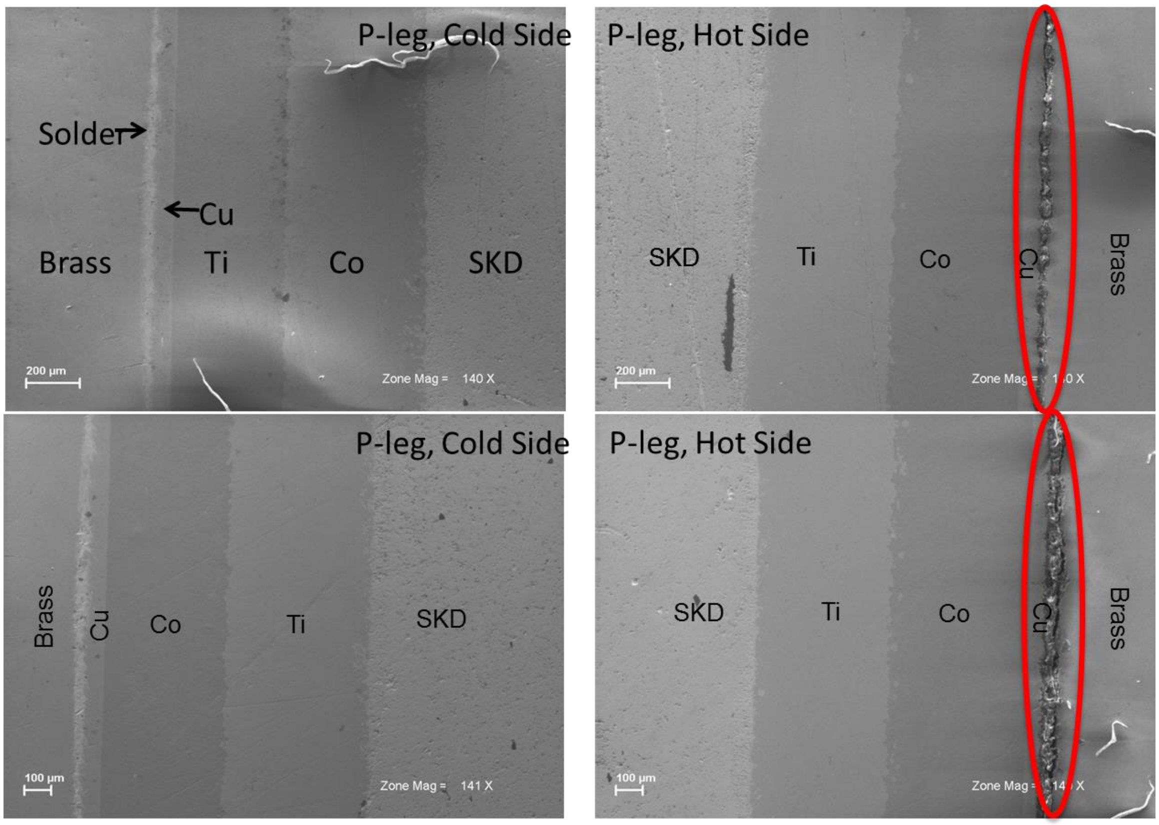

Figure 4.77. SEM image of the TE couple made of two brass rings (P-leg)

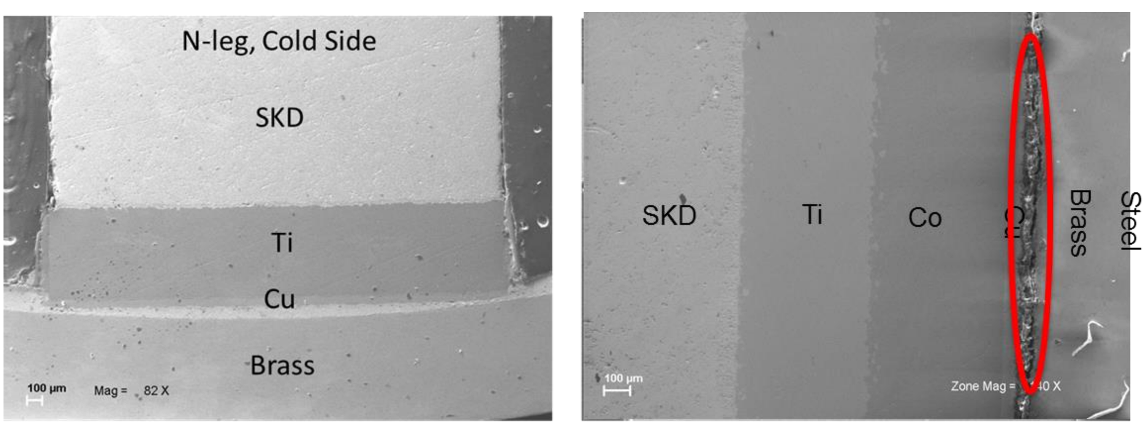

Figure 4.78. SEM image of the TE couple (steel ring inserted)

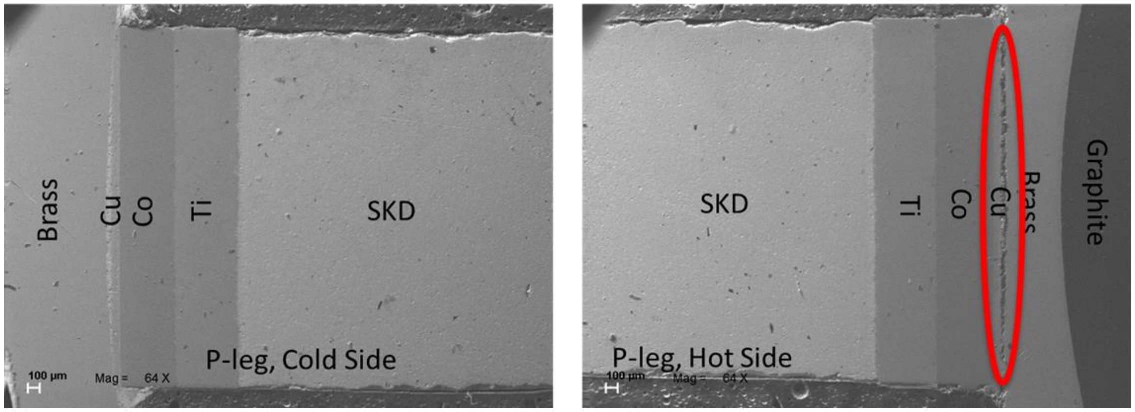

Figure 4.79. SEM image of the TE couple (graphite tube inserted)

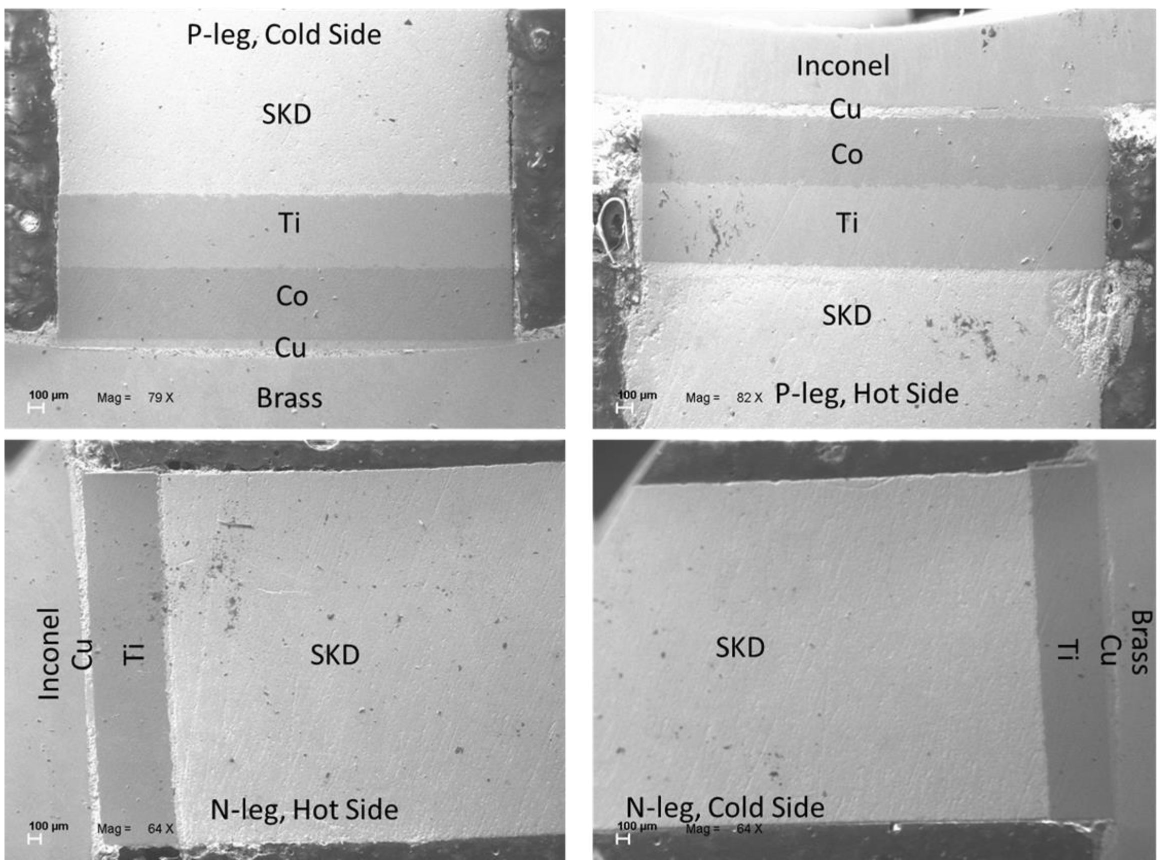

Figure 4.80. SEM image of the TE couple made of an Inconel ring

4.4.3 15 Watts TEG Testing

The prototype TEG was tested for performance through a range of temperatures by monitoring the cold and hot shoe. **Table 4.5** details the temperature, airflow and water flow rates recorded during each test.

Table 4.5. Temperatures and flow rates measured during the testing of the prototype TEG

	Test 1	Test 2	Test 3	Test 4
Exhaust Temp In (^oC)	495	574	690	690
Hot Shoe Temp (^oC)	405	476	544	545
Cold Shoe Temp (^oC)	105	128	134	145
Airflow (cfm)	15.0	15.0	15.0	15.4
Water flow (lpm)	10.8	10.8	10.8	10.4
ΔT Water (^oC)	1.0	1.0	1.1	1.2
ΔT Shoe (^oC)	300	348	410	400

For each test, the air-torch was allowed to reach a steady-state temperature. The 4 modules in the TEG were then independently back-loaded from 0 to 20.6 amps while recording the output voltage. A sample of the voltage and the calculated power output for module 4 is shown in **Figure 4.81**. The results show that as the ΔT increased between the hot and cold shoe, both the voltage power output and peak power increased. The maximum peak power increased from 2.14 watts at ΔT of 300 ˚C to 4.39 watts at ΔT of 400 ˚C. The corresponding voltages at the peak power output were 0.19 and 0.28 volts respectively. The difference between test 3 and 4 was that the airflow rate was increased slightly, which also increased the peak power output.

The individual power curves for each module are presented in **Figure 4.82-Figure** 4.85**.** The maximum power output at the highest temperature difference ranged from 3.13 to 4.39 watts. For each module, the power output increased with each increase in temperature difference. There was also an increase in power output when the airflow rate increased while maintaining the same temperature difference across the hot and cold shoes.

The overall power output of the prototype TEG is presented in **Figure 4.86**. At a ΔT of 300 ˚C the TEG produced 7.71 watts and increased 15.31 watts at a ΔT of 400 ˚C. The voltage output recorded at the peak power was 1.05 volts.

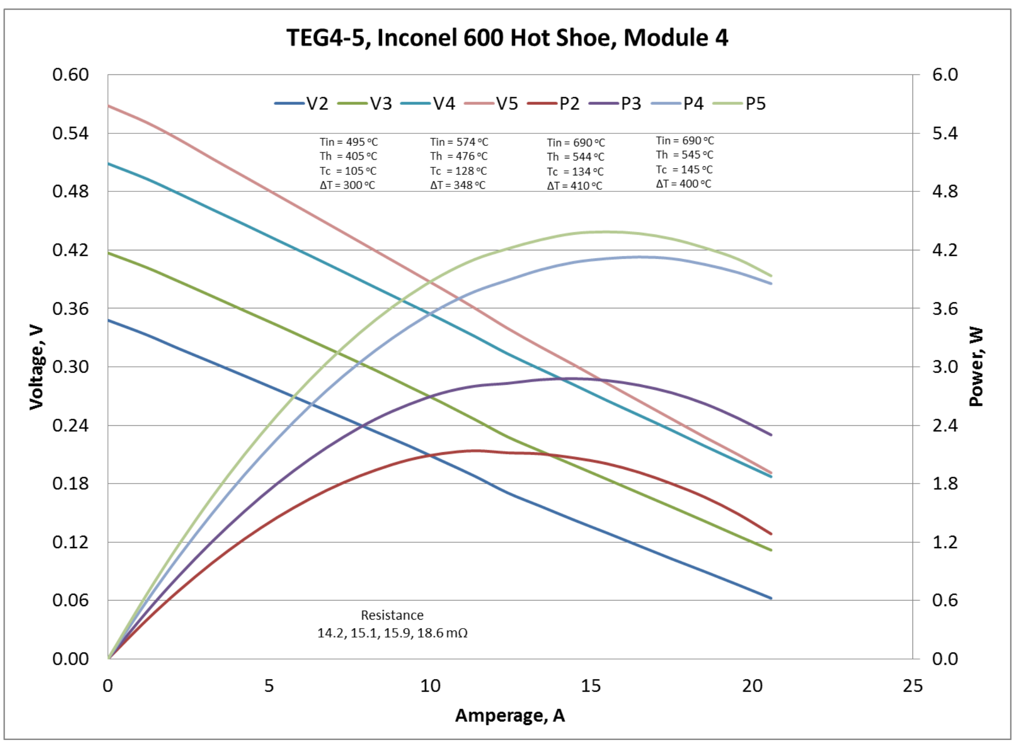

Figure 4.81. Voltage and power output for prototype TEG module 4

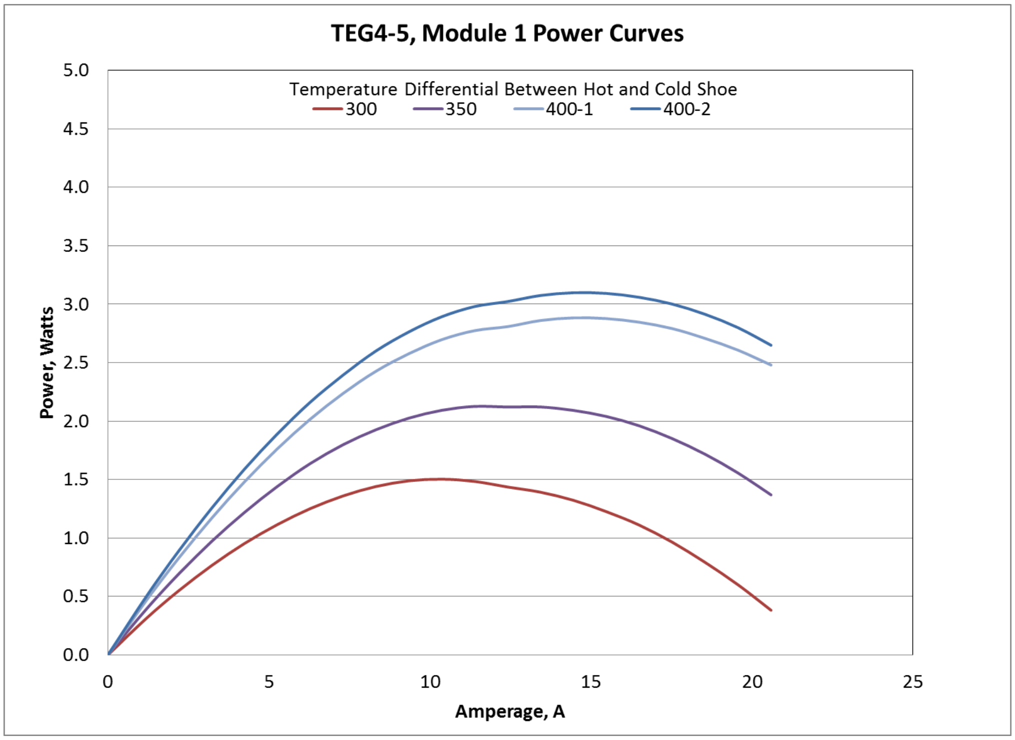

Figure 4.82. Power output for prototype TEG module 1

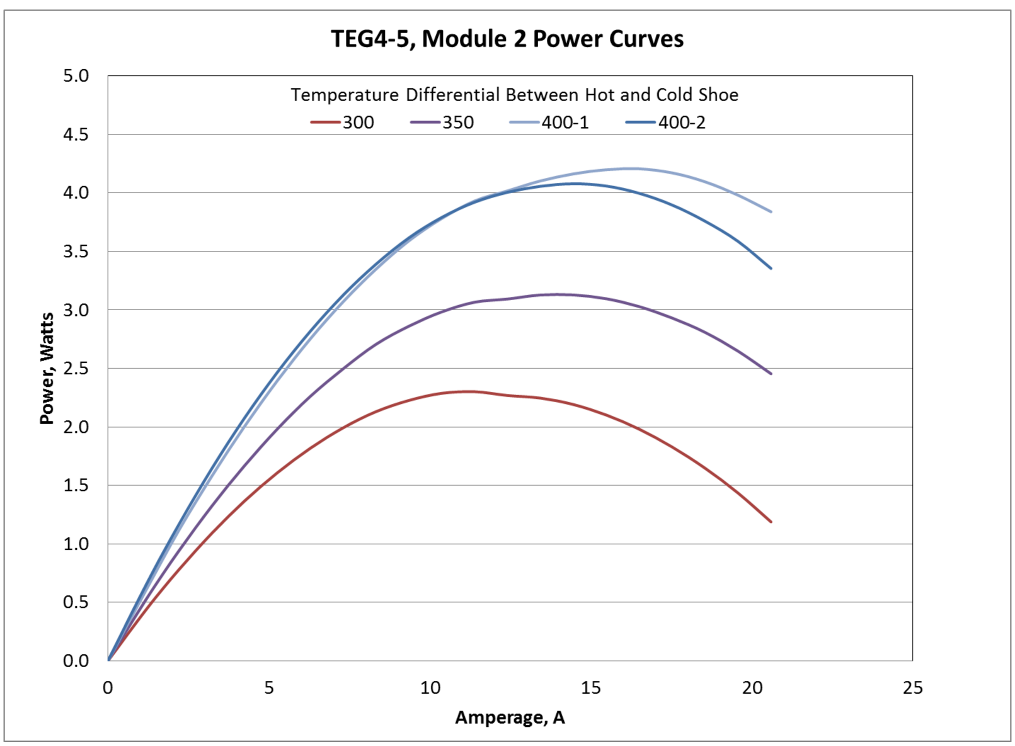

Figure 4.83. Power output for prototype TEG module 2

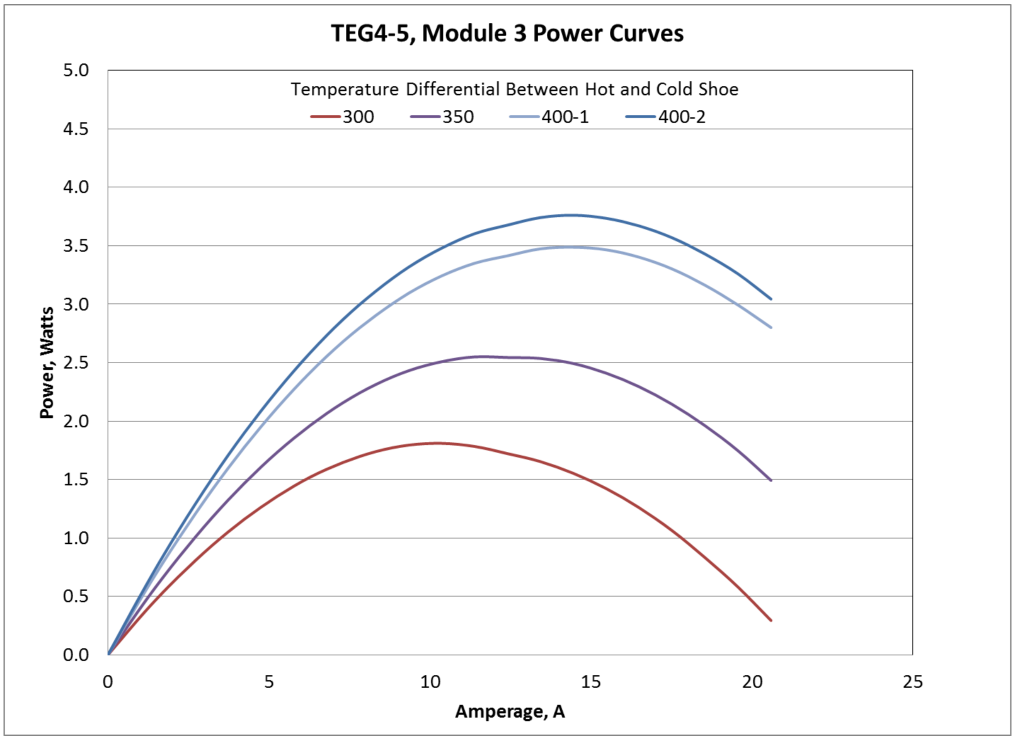

Figure 4.84. Power output for prototype TEG module 3

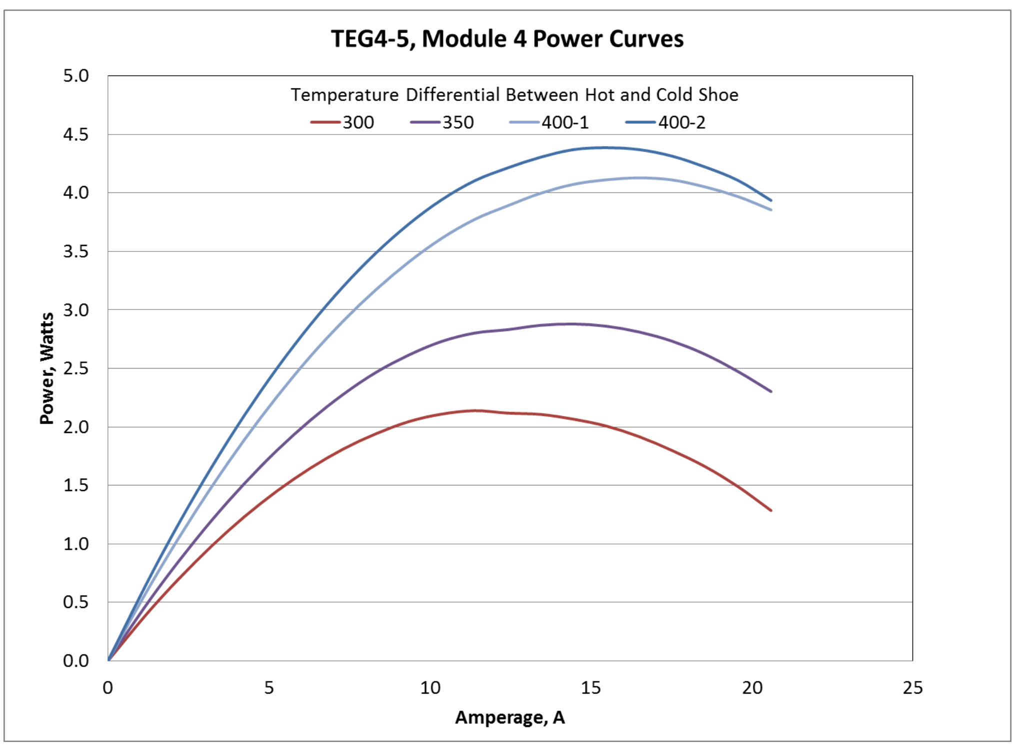

Figure 4.85. Power output for prototype TEG module 4

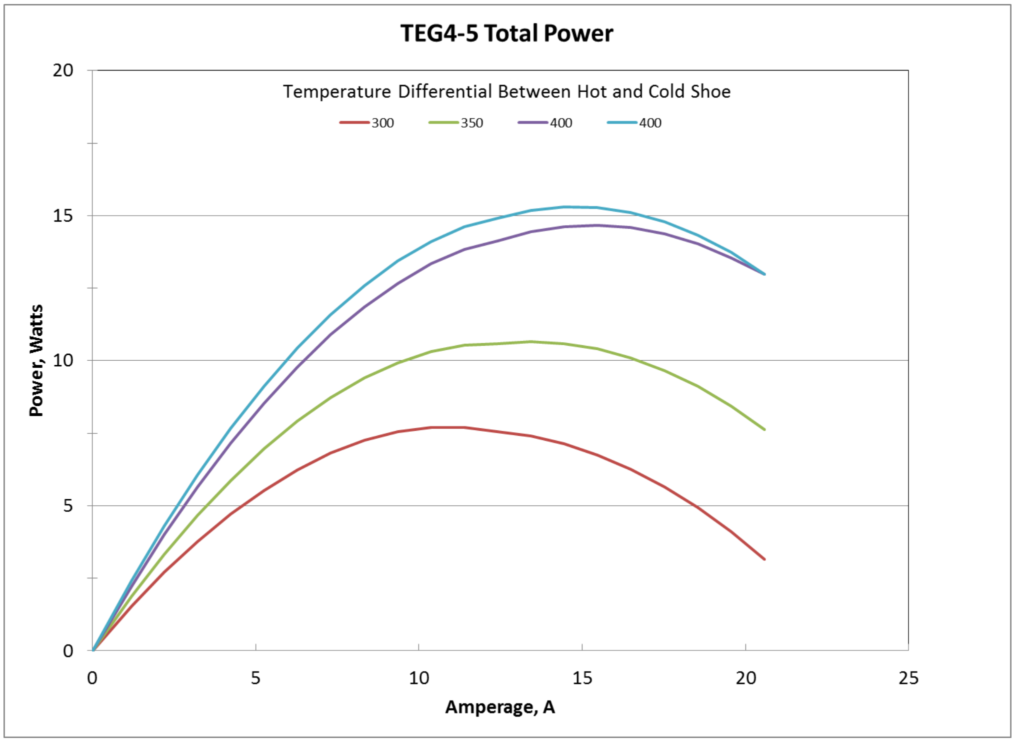

Figure 4.86. Total power output for prototype TEG

4.4.4 15-Watt TEG Performance Test Based on the Engine Simulation Data

The exhaust gas temperature and mass flow rate which the TEG receives is determined by the location of TEG within the exhaust section. As shown in **Figure 4.87**, for the test, the exhaust gas from the engine comes out from two exhaust headers, and then flow through the first left and right catalytic converters. After entering these converters, it goes through the flow pipes and enters the second left and right catalytic converters. To achieve high exhaust gas temperature and mass flow rate, the thermoelectric generator must be located after the last set of catalysts.

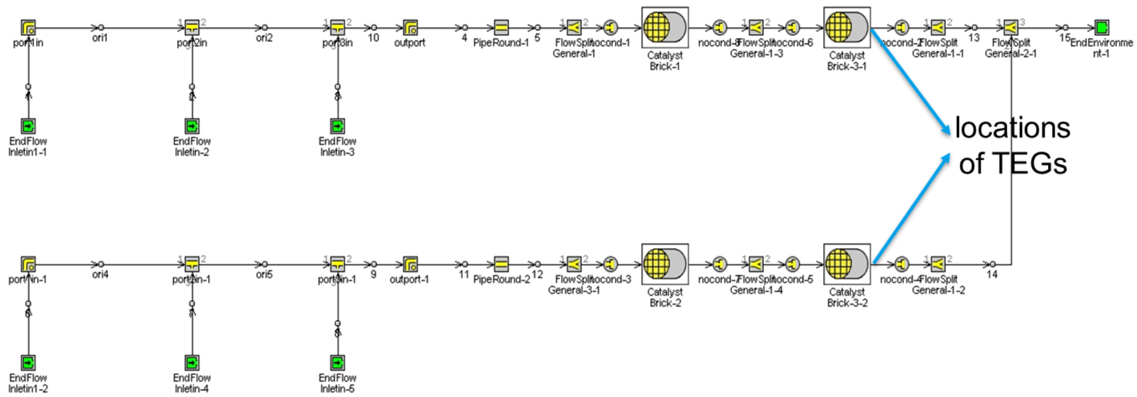

Figure 4.87. After-treatment system with the location of the TEGs

The initial goal of the project was design and manufacturing of a 120 watts TEG. The first prototype was predicted to generate 15 watts. Hence, if four of the TEGs would be installed in series after each of the last two catalysts, the total power output is predicted to be 120 watts. With the simulated engine data (exhaust gas mass flow rate and temperature) from GT-Power, electrical power production of TEG was predicted to be 17 watts at the operating point of 3 bar engine load at 2000 RPM. Based on the 17 watts generator experiments, the whole TEG system performance at 2000 RPM and 30% full engine load is estimated to be 136 watts.

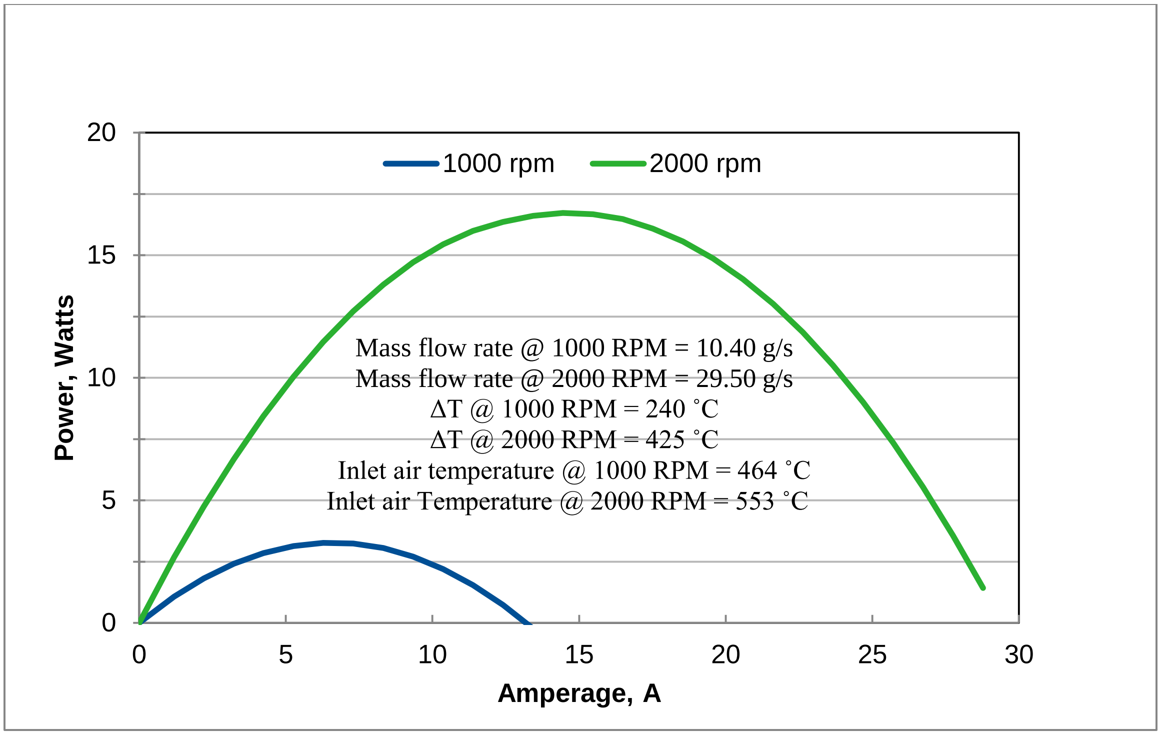

Figure 4.88. Total power output for prototype TEG based on experiments

Figure 4.88 shows electrical power output based on one of the eight TEGs at 2000 rpm and 3 bar engine load. Total power output is based on the performance of one TEG multiple by eight which was described earlier.

5. CONCLUSION

This study has been conducted to show with the appropriate support, successful demonstration and potential commercialization of TEG technology for waste heat recovery in a vehicle. As discussed, three factors that would significantly improve the energy harvesting capabilities of TEG are:

1) Performance improvements in thermoelectric materials
2) TE couple assembly having stresses below the yield limit of the each components
3) Overall system design including required electronics

Using liquid coolant (water), equivalent to that used in the engine cooling system with a temperature of about 50 ˚C to cool the outer wall of the TEG, results in average exhaust gas-side wall temperature in the range of approximately 300 ˚C to 400 ˚C.

In this work, combination of materials, research, experiment, and simulation were focused on modeling the real-life condition of the thermoelectric couple performance. Two significant roadblocks to feasibly manufacturing and implementing TEGs were identified. First, the risk of a broken or cracked couple was found to pose a significant threat to the overall power production of the entire generator. The couples and modules need to be wired or connected in series to maximize voltage generation. If a single broken couple disrupts the electric circuit, it negates the power generation of the whole generator. Secondly, the couple degradation and failures occurred during testing compromised generator longevity.

The initial work in the net shaped hot pressed couple led to many different variations in design and performance. The powder processing and hot pressing techniques for TE fabrication were developed. The thermal and mechanical properties of the TE materials, which were provided by NASA JPL, were used to get a robust simulation of the thermoelectric couple under heat and mechanical loads. While the performance of the first generation couple showed promise, the structural integrity of the p-type leg resulted in radial and circumferential cracking caused by excessive tensile stresses. Several different methods were studied in an effort to reduce the cracking; however none of the techniques solved the problem.

Using the square leg and compression couple technology led to design and develop the second generation thermoelectric couples. Early performance results indicate the second generation TE couple has promise but, additional design work will be needed to optimize the design parameters such as durability and performance of the couple components.

Commercialization of the thermoelectric generator depends on several challenges including heat exchanger, couple design and generator development. Measuring system performance with high figure-of-merit thermoelectric material is not completely satisfactory to determine generator performance. Overall performance of the system depends not only on the stability of the materials, but also on design and manufacturing of the generator follow by proper heat exchangers. An active research and development effort along with testing the new thermoelectric generator indicates a solution to the mentioned couple and generator challenges. Power output of 15 watts was predicted and demonstrated by testing the generator. Performance and long term durability tests showed the generator is mechanically stable preliminary and the TEG will not show a power drop in overall system energy conversion output.

Finally, the use of geometrical modelling tools, coupled with 1-D engine simulation, computational fluid dynamics, and finite element analysis, can be used to reasonably predict the heat transfer, temperature distribution, fluid flow profile and thermal stresses followed by durability of the thermoelectric generator under cyclic loads.

6. FUTURE WORK

Since a good research usually raises as many more questions as it answers, the results presented in this dissertation provide several opportunities for further studies. These include:

1) The effect of back-pressure in the engine after installing TEGs after the EGR cooler or in a combined package with catalytic converter.
2) GT-Power model can be coupled into an advanced 3D heat transfer and fluid flow model or simulation code (e.g. StarCCM+) to predict the efficiency of the thermoelectric generators.
3) Coupled model of 1D engine, 3D model of heat transfer and fluid flow, can be coupled to a finite element based code to predict the durability of the generator. In this way, solid stresses generated in the generator, based on the temperature and heat fluxes, can be calculated and studied.
4) Lessons learned from this set of simulations and experiments can be employed in TEG power generation simulation. With the help of simulation, power output can be predicted and generalized as a function of mass flow rate and temperature which will skip the time of labor to run actual experiments.

REFERENCES

REFERENCES

1. Taylor, C.F., *The Internal-combustion Engine in Theory and Practice: Combustion, fuels, materials, design*. Vol. 2. 1985: MIT press.

2. Crane, D.T. and L.E. Bell, *Design to Maximize Performance of a Thermoelectric Power Generator With a Dynamic Thermal Power Source.* Journal of Energy Resources Technology, 2009. **131**(1): p. 012401-012401.

3. Priest, M. and C. Taylor, *Automobile engine tribology—approaching the surface.* Wear, 2000. **241**(2): p. 193-203.

4. Small, K.A. and K. Van Dender, *Fuel efficiency and motor vehicle travel: the declining rebound effect.* The Energy Journal, 2007: p. 25-51.

5. Liu, B.-T., K.-H. Chien, and C.-C. Wang, *Effect of working fluids on organic Rankine cycle for waste heat recovery.* Energy, 2004. **29**(8): p. 1207-1217.

6. Chen, H., D.Y. Goswami, and E.K. Stefanakos, *A review of thermodynamic cycles and working fluids for the conversion of low-grade heat.* Renewable and Sustainable Energy Reviews, 2010. **14**(9): p. 3059-3067.

7. Rowe, D.M., *Thermoelectrics, an environmentally-friendly source of electrical power.* Renewable energy, 1999. **16**(1): p. 1251-1256.

8. Xi, H., L. Luo, and G. Fraisse, *Development and applications of solar-based thermoelectric technologies.* Renewable and Sustainable Energy Reviews, 2007. **11**(5): p. 923-936.

9. DiSalvo, F.J., *Thermoelectric Cooling and Power Generation.* Science, 1999. **285**(5428): p. 703-706.

10. Goldsmid, H. and R. Douglas, *The use of semiconductors in thermoelectric refrigeration.* British Journal of Applied Physics, 1954. **5**(11): p. 386.

11. Hicks, L. and M. Dresselhaus, *Effect of quantum-well structures on the thermoelectric figure of merit.* Physical Review B, 1993. **47**(19): p. 12727-12731.

12. Schmidt, R.D., et al., *The temperature dependence of thermal expansion for p-type Ce0.9Fe3.5Co0.5Sb12 and n-type Co0.95Pd0.05Te0.05Sb3 skutterudite thermoelectric materials.* Philosophical Magazine, 2012. **92**(10): p. 1261-1286.

13. Tritt, T.M. and M. Subramanian, *Thermoelectric materials, phenomena, and applications: a bird's eye view.* MRS bulletin, 2006. **31**(03): p. 188-198.

14. Goldsmid, H.J., *Recent Trends in Thermoelectric Materials, Semiconductors and Semimetals.* Aademic 2000. **69, Ch. 1**.

15. Schmidt, R.D., et al., *Temperature-dependent Young's modulus, shear modulus and Poisson's ratio of p-type Ce0.9Fe3.5Co0.5Sb12 and n-type Co0.95Pd0.05Te0.05Sb3 skutterudite thermoelectric materials.* Philosophical Magazine, 2011. **92**(6): p. 727-759.

16. Kenny, H., et al., *Heat Transfer Enhancement in Thermoelectric-Power Generation*, in *47th AIAA Aerospace Sciences Meeting including The New Horizons Forum and Aerospace Exposition*. 2009, American Institute of Aeronautics and Astronautics.

17. Case, E., *Thermal Fatigue and Waste Heat Recovery via Thermoelectrics.* Journal of Electronic Materials, 2012. **41**(6): p. 1811-1819.

18. Biswas, K., et al., *High-performance bulk thermoelectrics with all-scale hierarchical architectures.* Nature, 2012. **489**(7416): p. 414-418.

19. Bangert, K., *BMW Turbosteamer and Thermoelectric Generator Projects Aim to Harness Heat Energy*. 2013.

20. Bell, L.E., *Cooling, Heating, Generating Power, and Recovering Waste Heat with Thermoelectric Systems.* Science, 2008. **321**(5895): p. 1457-1461.

21. Tom, S., et al., *Heat Transfer and Electric Current Flow in a Thermoelectric Couple*, in *44th AIAA Aerospace Sciences Meeting and Exhibit*. 2006, American Institute of Aeronautics and Astronautics.

22. Hendricks, T.J., *Thermal system interactions in optimizing advanced thermoelectric energy recovery systems.* Journal of Energy Resources Technology, 2007. **129**(3): p. 223-231.

23. Schock, H., et al., *Prospects for Implementation of Thermoelectric Generators as Waste Heat Recovery Systems in Class 8 Truck Applications.* Journal of Energy Resources Technology, 2013. **135**(2): p. 022001.

24. Zheng, M., G.T. Reader, and J.G. Hawley, *Diesel engine exhaust gas recirculation—a review on advanced and novel concepts.* Energy conversion and management, 2004. **45**(6): p. 883-900.

25. Yang, J. and F.R. Stabler, *Automotive applications of thermoelectric materials.* Journal of Electronic Materials, 2009. **38**(7): p. 1245-1251.

26. Justi, E., *THERMOELEMENT*. 1954, Google Patents.

27. Seebeck, T., *Magnetic polarization of metals and minerals.* Abhandlungen der Deutschen Akademie der Wissenschaften zu Berlin, 1822. **265**: p. 1823.

28. Paulsson, M. and S. Datta, *Thermoelectric effect in molecular electronics.* Physical Review B, 2003. **67**(24): p. 241403.

29. Peltier, J. *Nouvelles experiences sur la caloricite des courans electrique*. in *Annales de Chimie et de Physique*. 1834.

30. Rowe, D.M., *CRC handbook of thermoelectrics*. 1995: CRC press.

31. Thomson, W., *On a mechanical theory of thermoelectric currents.* Proceedings of the Royal Society of Edinburgh, 1851. **91**: p. 1851.

32. Altenkirch, E., *Über den Nutzeffekt der Thermosäule.* Physikalische Zeitschrift, 1909. **10**: p. 560.

33. Telkes, M., *The Efficiency of Thermoelectric Generators. I.* Journal of Applied Physics, 1947. **18**(12): p. 1116-1127.

34. Vedernikov, M. and E. Iordanishvili. *AF Ioffe and origin of modern semiconductor thermoelectric energy conversion*. in *Thermoelectrics, 1998. Proceedings ICT 98. XVII International Conference on*. 1998. IEEE.

35. Rowe, D. and C. Bhandari, *Modern Thermoelectrics, 1983.* Holt, Rinehart and Winston, London: p. 7-13.

36. Chen, J. and C. Wu, *Analysis on the Performance of a Thermoelectric Generator.* Journal of Energy Resources Technology, 1999. **122**(2): p. 61-63.

37. Xia, Y., et al., *One‐dimensional nanostructures: synthesis, characterization, and applications.* Advanced materials, 2003. **15**(5): p. 353-389.

38. Matsuura, K., et al. *Design Optimisation for a Large Scale Low Temperature Thermoelectric Generator*. in *Proc. Xlth International Conference on Thermoelectrics*. 1992.

39. Rowe, M.D., et al. *Thermoelectric recovery of waste heat-case studies*. in *Energy Conversion Engineering Conference, 1997. IECEC-97., Proceedings of the 32nd Intersociety*. 1997. IEEE.

40. Goldsmid, H.J., *Applications of thermoelectricity.* 1960.

41. Chen, M., S.-S. Lu, and B. Liao, *On the Figure of Merit of Thermoelectric Generators.* Journal of Energy Resources Technology, 2005. **127**(1): p. 37-41.

42. Rowe, D. and C. Bhandari, *Effect of grain size on the thermoelectric conversion efficiency of semiconductor alloys at high temperature.* Applied Energy, 1980. **6**(5): p. 347-351.

43. Bhandari, C.M. and D.M. Rowe, *Thermal conduction in semiconductors*. 1988: Wiley New York.

44. Stordeur, M., et al., *Investigation of the Valence Band Structure of Thermoelectric (Bi1− xSbx) 2Te3 Single Crystals.* physica status solidi (b), 1988. **150**(1): p. 165-176.

45. Dashevskii, Z., et al., *Cryogenic thermoelectric coolers with passive high-Tc superconductor branches.* Superconductor Science and Technology, 1992. **5**(11): p. 690.

46. Hicks, L. and M. Dresselhaus, *Thermoelectric figure of merit of a one-dimensional conductor.* Physical review B, 1993. **47**(24): p. 16631.

47. Heikes, R.R. and R.W. Ure, *Thermoelectricity: science and engineering*. 1961: Interscience Publishers New York.

48. Singh, G., *Steady state and transient analysis of thermoelectric devices using finite element method.* 2003.

49. Gray, P.E. and R. Wolfe, *The dynamic behavior of thermoelectric devices.* Journal of The Electrochemical Society, 1960. **107**(10): p. 242C-242C.

50. Egli, P.H., *Thermoelectricity*. 1960: John Wiley & Sons.

51. Measurement, A.C.E.o.T., *Manual on the use of thermocouples in temperature measurement*. Vol. 28. 1993: ASTM International.

52. Harman, T.C. and J.M. Honig, *Thermoelectric and thermomagnetic effects and applications.* 1967, 377 P. MCGRAW-HILL INC., NEW YORK, N. Y.$ 17. 50, 1967.

53. Wong, A., J. Sparrow, and S. Dunn, *On the revised theory of the thermoelastic effect.* Journal of Physics and chemistry of solids, 1988. **49**(4): p. 395-400.

54. Measurement, A.C.E.-o.T. and A.C.E.-o.T.M.S.E.o. Thermocouples, *Manual on the use of thermocouples in temperature measurement*. Vol. 470. 1981: ASTM International.

55. Das, S.K., et al., *Temperature dependence of thermal conductivity enhancement for nanofluids.* Journal of Heat Transfer, 2003. **125**(4): p. 567-574.

56. Ashcroft, N., *ND Mermin Solid state physics.* Saunders College, Philadelphia, 1976.

57. Fleurial, J.-P., *Thermoelectric power generation materials: Technology and application opportunities.* JOM, 2009. **61**(4): p. 79-85.

58. Mansouri, N., et al., *Development of a Circular Thermoelectric Skutterudite Couple Using Compression Technology*. Journal of Energy Resources Technology, 2015.

59. Mansouri, N., et al., *Design Simulations, Experiments and Estimated On-Vehicle Performance for a Compression-Couple Based Thermoelectric Generator*. Journal of Energy Resources Technology, 2015.

60. Slayzak, S., R. Viskanta, and F. Incropera, *Effects of interactions between adjoining rows of circular, free-surface jets on local heat transfer from the impingement surface.* Journal of heat transfer, 1994. **116**(1): p. 88-95.

61. Pepper, D.W. and J.C. Heinrich, *Finite Element Methods: Basic Concepts And Applications: Basic Concepts and Applications*. 1992: CRC Press.

62. Reddy, J.N., *An introduction to the finite element method*. Vol. 2. 1993: McGraw-Hill New York.

63. Hastings, J., M. Juds, and J. Brauer. *Accuracy and economy of finite element magnetic analysis*. in *33rd Annual National Relay Conference*. 1985.

64. Long, P., W. Jinliang, and Z. Qiding, *Methods with high accuracy for finite element probability computing.* Journal of computational and applied mathematics, 1995. **59**(2): p. 181-189.

65. Jimenez-Puente, I., *Offshore Field Development in Cold Climate: with Emphasis on Terminals.* 2013.

66. Alboni, P.N., *Effect of cobalt antimonide nanoparticles on the thermoelectric properties of filled and unfilled cobalt antimonide skutterudites.* 2009.

67. Gau, C. and C. Chung, *Surface curvature effect on slot-air-jet impingement cooling flow and heat transfer process.* Journal of Heat Transfer, 1991. **113**(4): p. 858-864.

68. Yeh, L., *Review of heat transfer technologies in electronic equipment.* Journal of electronic packaging, 1995. **117**(4): p. 333-339.

69. Shih, T.-H., et al., *A new k-ϵ eddy viscosity model for high reynolds number turbulent flows.* Computers & Fluids, 1995. **24**(3): p. 227-238.

70. Henkes, R., F. Van Der Vlugt, and C. Hoogendoorn, *Natural-convection flow in a square cavity calculated with low-Reynolds-number turbulence models.* International Journal of Heat and Mass Transfer, 1991. **34**(2): p. 377-388.

71. MacDonald, S., *New corporate image for CD-adapco.*